Università degli Studi di Padova

Centro Ricerche Fusione (**CRF**)

Universidade de Lisboa

Instituto Superior Técnico (**IST**)

Università degli studi di Napoli Federico II

JOINT RESEARCH DOCTORATE IN FUSION SCIENCE AND ENGINEERING

Cycle XXX

Theoretical study and design of a CARM type millimeter wave source

Coordinator: Prof. Paolo Bettini

Supervisor: Prof. Fabio Villone

Co-Supervisors: Prof. Giuseppe Dattoli

Ph.D. student: Emanuele Di Palma

Padova, January 2018

UNIVERSITÀ DEGLI STUDI DI PADOVA

JOINT Doctorate and NETWORK in Fusion Science and Engineering

Network Partners:

- Instituto Superior Técnico (IST) Lisboa, Portugal
- Università degli studi di Padova, Italy
- Ludwig Maximilians University Munich, Germany

In collaboration with:

Consorzio RFX
IPP Garching, Germany

Acknowledgements

I would like to express my gratitude to Dr. Ivan Spassovsky (the scientific responsible of the ENEA CARM project) for having introduced me to this interesting and challenging research six years ago, transferring patiently his wide knowledge in this topic and believing in me even if I was coming from a total different background. At the same time I want to thank Prof. Giuseppe Dattoli introducing me to the Physics of free electron laser and for sharing with me his physical insights. His talent in the Mathematical/Physics and the long experience in the FEL devices allowed to facilitate the theoretical analysis reported in this thesis. During this period, his guidance as a mentor is an invaluable part of my education.

I have sincerely been lucky to work under their supervision which has led to the successful conclusion of the thesis work.

I'm also grateful to my supervisor Prof. Fabio Villone for the interest in the thesis topic and advice during the PhD courses.

In addition I would to thank all the Enea CARM Task Force from which I received a fruitful advices during the periodical meeting we held at Enea Frascati.

It is a great pleasure to thank Prof. Gregory Nusinovich, one of the greatest authorities in the field of CARM and gyrotron devices, for clarifying and helpful discussions. Professor Svilen Sebacevsky has always been available and helpful in either explaining dark points and very much patient in reviewing computation and draft papers.

I want to express my sincere appreciation to Profs. Naum Ginzburg, Mikhail Glyavin, Nikolay Peskov and Andrei Savilov for the kind hospitality and enlightening discussion we had both at ENEA Frascati and at the Institute of Applied Physics of the Russian Academy of Science (IAP/RAS) in Nizhny Novgorod.

Last but not least words to thank Dott. Silvia Licciardi for the collaboration during the preparation of the CDR and for kind help and encouragement.

Contents

Summary

In Nuclear Fusion external heating sources play a role of paramount relevance for the twofold role of plasma heating and instability suppression. The effectiveness of Electron Cyclotron (EC) waves in Tokamaks have been experimentally demonstrated since the early 80's of the last century (see e. g. the pioneering work by R.M. Gilgenbach et al., 1980). Nowadays EC systems plays a pivotal role in magnetic fusion devices and their need in future experimental reactors is out of doubt. The physical reasons underlying these choices stems from the fact that electron cyclotron radiation can be coupled effectively to the plasma, producing a localized and controlled energy deposition. Within this framework an important tool has been provided by the electron cyclotron masers (ECM) sources, namely gyrotron-like device, extensively used because able to provide sufficiently large power in the millimeter and sub-millimeter region.

The gyrotrons provide the most mature and reliable technology in the field of millimeter-wave tubes, their use is however hampered by the fact that they meet some difficulty of operation (in terms of delivered power and efficiency) in the spectral range above 200 GHz.

The possibility of exploiting different generators of powerful millimeter-wave coherent radiation has therefore been suggested. In this context a research and development program has been undertaken at ENEA Frascati Center, aimed at realizing a microwave tube based on a Cyclotron Auto-Resonance Maser (CARM) oscillator, characterized by a high value of the Doppler up-shift interaction allowing a consistent reduction of the static magnetic field in the interaction cavity and enhanced efficiency with a moderately relativistic beam due to the auto resonance mechanism. The price to be paid is the necessity of exploiting high quality electron beams, with velocity spread below 0.5%, in order to ensure appropriate mode selection, enough gain to oscillate and adequate beam-wave power transfer with the required efficiency.

The low beam quality has been the main element that has affecting the performances of the first CARM experiments on the eve of the last century. Most of the them used already existing high-voltage accelerators producing electron beams with currents of several kA. They were powered by modulators having non-appropriate waveform with respect to flat-top ripple. The beam was emitted from a cold cathode and then blasted toward the small aperture, used either to scratch out the largest part of the beam and as an emittance filter. This mechanism never succeeded to deliver a beam with appropriate characteristics. Even though the data relevant to the beam qualities are rather insufficient, serious doubts can be raised on the reliability of such drivers for CARM operation.

The research line associated with the present Ph.D. thesis, developed at ENEA with the CARM project team, has gone through different phases, the first of which has been the understanding of the physical mechanisms underlying the operation of the different devices (Gyrotron, FEL, CARM, Gyro-Backward...).

A significant part of the thesis has been devoted to the design of the various components of the CARM device, including the cathode, the principal magnet and the radiation confining cavity. Most of the design effort has been devoted to the production of a beam with suited characteristic for the CARM operation. Successively, particular care has been devoted in putting in evidence the relative pro's and con's and noticeable efforts has been devoted to the understanding of the factors which have limited the CARM efficiency in the past experiments.

In chapter 1 we review the relevant issues to the thermonuclear fusion as a clean solution for the world energy demand putting in evidence the requirements for a commercial power fusion plant. In particular the studies, undertaken under auspices of the European Fusion Development Agreement (EFDA) for a different configuration of a DEMOnstration fusion reactor, get out the importance of the efficiency for the Heating and Current Drive (H&CD) systems.

We report a short description of the physical mechanism governing the fusion reaction. We discussed the role played by the plasma instabilities in a Tokamak plant and the necessity of their suppression or control. We put therefore in evidence the necessity of additional H&CD devices in Tokamak plants and analyze the required characteristics in terms of frequency and power.

In chapter 2 we describe the design of the ENEA CARM facility. We start with

the analysis of a thermionic gun and perform accurate simulation determine the conditions for the generation of a high quality beam, in terms of the longitudinal velocity spread. The simulation are benchmarked with an analytical modeling of the beam transport by means of the generalization of the Courant-Snyder formalism which simplifies the beam transport design for this device, demanding for an accurate control of the beam transverse dimension.

The forthcoming chapter 3 contains a thorough analysis of CARM interaction, carried out using previous theoretical formulation providing the coupled beam-wave evolution equations. The theory is then confronted with that of U-FEL systems. The results of this efforts is that of providing a set of semi-analytical formulae useful for a quick design of the device. The relevant reliability has been benchmarked using the home-made code GRAAL and tested for a variety of study cases. Furthermore, a "universal" scaling formula describing the CARM performance embedding inhomogeneous broadening effects and the beam current, as it happens in the case of U-FEL, has been derived for monitoring the accuracy and for diagnosing the calculations during the numerical experiments.

The concluding chapter 4 deals with the CARM oscillator configuration. It contains the description of the system, the evaluation of the gain and saturation mechanism and the design of the radiation confining cavity with particular reference to the relevant optimization of the suppression of the spurious modes.

Sommario

Nella fusione nucleare le sorgenti di riscaldamento addizionale svolgono un ruolo di fondamentale importanza per un duplice motivo: raggiungimento della temperatura della reazione di fusione e soppressione delle instabilità di plasma. L'efficacia dei sistemi di riscaldamento tramite l'utilizzo di onde alla frequenza ciclotronica elettronica (EC) nei Tokamaks è stata sperimentalmente dimostrata fin dai primi anni '80 del secolo scorso (si veda ad esempio il lavoro pionieristico di R.M. Gilgenbach et al., 1980). Oggi i sistemi EC giocano un ruolo chiave nei dispositivi a fusione magnetica e la loro necessità nei futuri reattori sperimentali è fuori dubbio. Le ragioni fisiche alla base di queste scelte derivano dal fatto che la radiazione alla frequenza ciclotronica elettronica può essere accoppiata efficacemente al plasma, apportando una deposizione di energia localizzata e controllata. Le sorgenti di tipo MASER hanno, in questo contesto, svolto un ruolo di primaria importanza. Il girotrone, infatti, è ampiamente utilizzato perché in grado di fornire in maniera efficiente una grande quantità di energia a lunghezza d'onda millimetrica e sub-millimetrica

I girotroni rappresentano, ad oggi, la tecnologia più matura e affidabile nel campo dei tubi a onde millimetriche, il loro utilizzo è tuttavia limitato alla regione spettrale al di sotto dei 200 GHz, in quanto al di sopra di questa frequenza si hanno difficoltà di operazione ad alta potenza ed alta efficienza.

La soluzione proposta per superare tale problema è l'utilizzo di una variante del gyrotron nota come CARM (Cyclotron Auto-Resonance Maser), caratterizzato da un alto valore dello spostamento in avanti della frequenza di interazione fascio-onda per effetto Doppler. In questo contesto è stato avviato un programma di ricerca e sviluppo presso il Centro ENEA di Frascati, finalizzato alla realizzazione di una sorgente di questo tipo che, grazie al già citato effetto Doppler, utilizza un campo magnetico statico significativamente ridotto rispetto a quello di un gyrotron operante alla stessa frequenza. Inolre, il meccanismo di auto-risonanza consente di

raggiungere una maggiore efficienza del sistema e quindi di operare con un fascio di elettroni moderatamente relativistico e di non alta potenza. Al fine di garantire l'operazione CARM in condizione di alta efficienza è necessario disporre di fasci di elettroni di elevata qualità, ovvero con una dispersione della distribuzione delle velocità delle particelle inferiore a 0.5%

La scarsa qualità del fascio di elettroni è stato l'elemento principale che ha influenzato le prestazioni dei primi esperimenti CARM durante la seconda metà del secolo scorso. La maggior parte di essi utilizzavano acceleratori ad alta tensione preesistenti, ovvero non progettati per produrre radiazione CARM, in grado di offrire fasci di ellettroni di diversi kA ma con una pessima dispersione in energia. Le ragioni che determinavano tale inappropriatezza sono ascritte sia ai modulatori sia ai metodi di estrazione del fascio dal catodo. I problemi nascevano infatti dalla mancanza di stabilità dei modulatori e dal metodo di filtraggio utilizzato per diminuire lo spread angolare.

Il progetto ENEA, nel cui ambito questa tesi è stata sviluppata, ha considerato con particolare attenzione le problematche relative alla preparazione di un fascio sufficientemente adeguato cosa resa possibile a 40 anni di distanza dai primi esperimenti CARM grazie allo sviluppo di tecniche di calcolo di progetto estremamente evolute insieme a nuove concezione di sviluppo nella tecnologia dei modulatori. La tesi ha attraversato diversi fasi, la prima delle quali è stata la comprensione dei meccanismi fisici alla base del funzionamento dei diversi dispositivi (Gyrotron, FEL, CARM, Gyro-Backward ...).

Una parte significativa della tesi è stata dedicata alla progettazione dei vari componenti del dispositivo CARM, tra cui il catodo, il magnete principale e la cavità di confinamento della radiazione. Gran parte dello sforzo progettuale è stato dedicato alla produzione di un fascio con caratteristiche adatte per l'operazione CARM. Successivamente, è stata prestata particolare attenzione nel mettere in evidenza i pro ed i contro e un grande sforzo è stato dedicato alla comprensione dei fattori che hanno limitato l'efficienza CARM negli esperimenti passati.

La struttura della tesi è gli argomenti trattati sono qui di seguito riportati.

Nel capitolo 1 analizziamo le questioni rilevanti per la fusione termonucleare come una soluzione pulita per la domanda mondiale di energia mettendo in evidenza i requisiti per un impianto di fusione di potenza commerciale. In particolare gli studi,

intrapresi sotto l'egida dell'Accordo europeo sullo sviluppo della fusione (EFDA) per diverse configurazioni di un reattore a fusione Dimostrativo, rivelano l'importanza dell'efficienza per i sistemi di riscaldamento e "current drive" (H&CD).

Riportiamo una breve descrizione del meccanismo fisico che governa la reazione di fusione. Discutiamo sul ruolo svolto dalle instabilità del plasma in un impianto Tokamak e la necessità della loro soppressione o controllo. Mettiamo quindi in evidenza la necessità di dispositivi H&CD negli impianti Tokamak e analizziamo le caratteristiche richieste in termini di frequenza e potenza.

Nel capitolo 2 descriviamo il disegno della macchina CARM in corso in ENEA. Iniziamo con l'analisi di un cannone termoionico ed eseguiamo una simulazione accurata determinando le condizioni per la generazione di un fascio di alta qualità, in termini della dispersione della velocità longitudinale delle particelle. La simulazione viene comparata con un modello analitico del trasporto del fascio mediante la generalizzazione del formalismo Courant-Snyder che semplifica la progettazione del trasporto del fascio per questo dispositivo, essendo richiesto un controllo accurato della dimensione trasversale del fascio.

Il capitolo successivo 3 contiene un'analisi approfondita dell'interazione fascio-onda di tipo CARM, effettuata usando la formulazione teorica già presente in letteratura che fornisce le equazioni di evoluzione dell'interazione fascio-onda. La teoria viene quindi confrontata con quella dei sistemi U-FEL. Il risultato di questo lavoro di confronto è quello di fornire un insieme di formule semi-analitiche utili per una rapida progettazione del dispositivo. L'affidabilità di queste formule è stata valutata utilizzando il codice GRAAL sviluppato nell'ambito di questa tesi e testato su diversi casi studio. Inoltre, è stata dedotta una legge di scala "universale" che descrive le prestazioni del CARM in funzione degli effetti di allargamento inomogenei e della corrente del fascio, come nel caso dell'U-FEL, per monitorare l'accuratezza e per diagnosticare i calcoli durante gli esperimenti numerici.

Il capitolo conclusivo 4 tratta della configurazione dell'oscillatore CARM. Contiene la descrizione del sistema, la valutazione del meccanismo di guadagno e saturazione e la progettazione della cavità di confinamento della radiazione con particolare riferimento alla relativa ottimizzazione della soppressione dei modi spuri.

Resumo

Na Fusão Nuclear as fontes de calor externo desempenham um papel de relevância primordial para a dupla função de aquecimento no plasma e de supressão de instabilidade. A eficácia das ondas Ciclotrônicas dos Elétrons (CE) em Tokamaks foi demonstrada experimentalmente desde o início dos anos 80 do século passado (ver, por exemplo, o trabalho pioneiro de R.M. Gilgenbach et al., 1980). Atualmente, os sistemas da CE desempenham um papel fundamental nos dispositivos de fusão magnética e suas aplicações em futuros reatores experimentais estão fora de questão. As razões físicas por traz dessa escolha decorrem do fato de que a radiação de ciclotrônica de elétrons pode ser acoplada efetivamente ao plasma, produzindo uma deposição de energia localizada e controlada. Dentro deste esquema, uma ferramenta importante foi fornecida pelas masers ciclotrônicos de elétrons (MCE), a saber, dispositivo de tipo girotron, amplamente utilizado, pois é capaz de fornecer energia suficientemente grande na região milimétrica e sub-milimétrica.

Os girotrons fornecem a tecnologia mais madura e confiável no campo de tubos de onda milimétrica, porém a suas aplicações são prejudicados pelo fato de que eles enfrentam alguma dificuldade de operação (em termos de potência e eficiência entregues) na faixa espectral acima de 200 GHz.

A possibilidade de explorar diferentes geradores de poderosa radiação coerente de ondas milimétricas tem sido sugerida. Neste contexto, um programa de pesquisa e desenvolvimento está sendo implantado Centro ENEA em Frascati, visando o desenvolvimento de um tubo de micro-ondas com base em um Maser Ciclotrônico de Auto-Ressonância (MCAR), que é caracterizado por um alto valor da interação Doppler com deslocamento para cima, permitindo assim uma consistente redução do campo magnético estático na cavidade de interação e eficiência aumentada com um feixe moderadamente relativista devido ao mecanismo de auto-ressonância. O preço a pagar é a necessidade de empregar feixes de elétrons de alta qualidade, com

espalhamento da velocidade de propagação abaixo de 0,5%, para garantir a seleção adequada do modo, ganho suficiente para oscilar e transferir energia de feixe para onda adequada com a eficiência necessária.

A baixa qualidade do feixe tem sido o principal elemento que afetou os desempenhos dos primeiros experimentos MCAR na final do século passado. A maioria deles usava aceleradores de alta tensão já existentes, produzindo feixes de elétrons com correntes de vários kA. Eles foram alimentados por moduladores com forma de onda não apropriada em relação à ondulação quadrada. O feixe foi emitido a partir de um cátodo frio e depois dirigido em direção à pequena abertura, usada para cortar a maior parte do feixe e também como um filtro de emitância. Este mecanismo nunca conseguiu produzir um feixe com características apropriadas. Embora os dados relevantes para as qualidades do feixe sejam bastante insuficientes, podem ser levantadas sérias dúvidas sobre a confiabilidade desses dispositivos para a operação do MCAR.

A linha de pesquisa associada ao presente tese de doutorado, desenvolvida na ENEA com a equipe do projeto MCAR, passou por diferentes fases, sendo a primeira a compreender os mecanismos físicos responsáveis para o funcionamento dos diferentes dispositivos (Girotron, LEL, MCAR, Giro-Onda-reversa ...).

Uma parte significativa da tese foi dedicada ao design dos vários componentes do dispositivo MCAR, incluindo o cátodo, o ímã principal e a cavidade de confinamento de radiação. A maior parte do esforço de design foi dedicada à produção de um feixe com características adequadas para a operação MCAR. Sucessivamente, um cuidado especial foi tomado a colocar em consideração todas as evidências pro e contra e esforços notáveis foram dedicados à compreensão dos fatores que limitaram a eficiência do MCAR nas experiências passadas.

No capítulo 1, analisamos as questões relevantes para a fusão termonuclear como uma solução limpa para a demanda mundial de energia, colocando em evidência os requisitos para uma usina comercial de fusão. Em particular, os estudos realizados sob os auspícios do Acordo Europeu de Desenvolvimento de Fusão (EFDA) para uma configuração diferente de um reator de fusão para demonstração destacou a importância da eficiência dos sistemas de aquecimento e Current Drive (sistemas H & CD).

Relatamos uma breve descrição do mecanismo físico que governa a reação de fusão. Discutimos o papel desempenhado pelas instabilidades do plasma em uma

maquina Tokamak e a necessidade de sua supressão ou controle. Entretanto nós colocamos em evidência a necessidade de dispositivos adicionais H & CD em Tokamaks e analisamos as características necessárias em termos de frequência e potência.

No capítulo 2, descrevemos o design do experimento em ENEA MCAR. Começamos com a análise de um emissor termiônico e realizamos uma simulação precisa para determinar as condições para a geração de um feixe de alta qualidade, em termos de espalhamento da velocidade longitudinal. A simulação é comparada com um modelo analítico para o transporte do feixe baseado a uma generalização do formalismo Courant-Snyder, que simplifica o desenho do sistema de transporte do feixe para este dispositivo, exigindo um controle preciso da dimensão transversal do feixe.

O próximo capítulo 3 contém uma análise minuciosa da interação MCAR, realizada com o formalismo teórico anterior, que fornece as equações de evolução acoplada da onda e do feixe. A teoria é então confrontada com desta de sistemas U-LEL. O resultado desses esforços foi a obtenção um conjunto de fórmulas semi-analíticas úteis para um design rápido do dispositivo. A confiabilidade relevante foi comparada com um código próprio (GRAAL) e testada para uma variedade de casos de estudo. Além disso, uma fórmula de escala "universal" que descreve o desempenho do MCAR incorporando efeitos do alargamento não homogêneos e da corrente do feixe, como acontece no caso de U-LEL, foi derivada para monitorar a precisão e para o diagnóstico dos cálculos durante as experiências numéricas.

O capítulo de conclusão 4 trata da configuração do oscilador MCAR. Ele contém a descrição do sistema, a avaliação do mecanismo de ganho e saturação e o desenho da cavidade de confinamento de radiação, com referência específica à otimização relevante da supressão dos modos espúrios.

Chapter 1

Fusion Power Plants

1.1 The energy world demand and the Power Fusion Plant

Energy demand is expected to more than double by 2050 as the combined effect of the increases of population and energy consumption per capita in developing countries.

In past two centuries, since the Industrial Revolution in the 1700s that was initiated by the invention of the steam turbine, the world has undergone a dramatic change due to the steeply increased contribution of fossil fuels (coal, oil, and natural gas) to modern societies' energy supply. Though the Chinese society already used coal for energy supply in approximately 1000 BC and the Romans prior to AD 400, the first written references indicating its use are from about the thirteenth century and beyond.

These hydrocarbon fuels so far have been considered essential, as they are comparatively cheap and convenient energy carriers used for heating, cooking, lighting and mechanical as well as electric power production and have been widely used as transportation fuels and feedstock for the manufacture of bulk and fine chemicals as well as other materials with a wide range of applications. Rapid global population growth, expansion of economies, and higher standards have caused an enormous increase in worldwide energy consumption, which was partly made possible by the supply of cheap fossil fuels that presently these satisfy 80% of the primary energy demand but their impact on the environment through greenhouse gas emission is

not tolerable.

In the past 30 years, carbon emissions have been steadily rising due to the increased use of all three fossil fuels: coal, oil and gas and these now stand at 32 Gigatonnes (Gt). The only periods in history when emissions dipped were during the economic crisis in former Soviet Union countries at the beginning of the 1990s and after the global economic crisis in 2008 as reported in Fig.1.1.

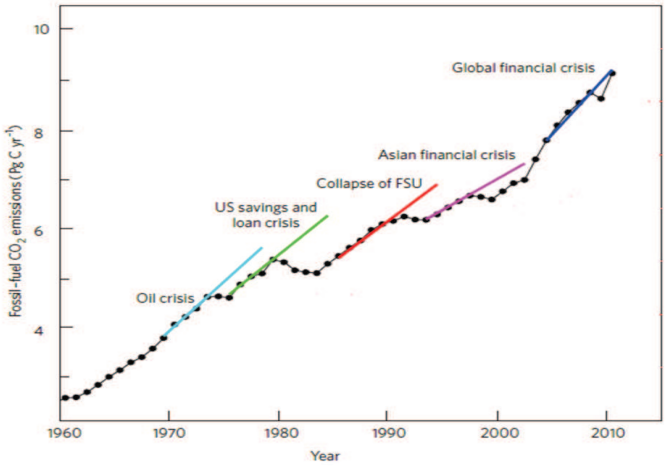

Figure 1.1: Emissions of CO_2 from fossil-fuel combustion and cement production for the world.The most important recent financial crises are highlighted with a linear trend fitted to the five years before the beginning of each crisis.[2]

Three different motivations drive today's energy discussions.

First, any resource and technology as well has a finite life-time, this is true for fossil fuel too. The use of a technology/resource follows a logistic behavior. It is characterized by different phases, which can be summarized as the innovation period, the maturity and saturation[1]. The resource consumption after the mature stage, when it is governed by resource price, slows down because of two other factors:

- there are no more new applications that make use of this resource,
- the price of the resource increases significantly because of profit-taking and because of the realization that the resource may be depleted and may become more valuable in the future.

The Hubbert curve allows the forecast of when a resource, after its maturity, is no more economically convenient, an example is reported in Fig.1.2 for the natural

gas production in USA. This pushes to seek alternative energy sources. The fossil fuel, useful for manufacture of plastics and all sorts of other creative stuff, must be preserved for better uses than simply to fire them.

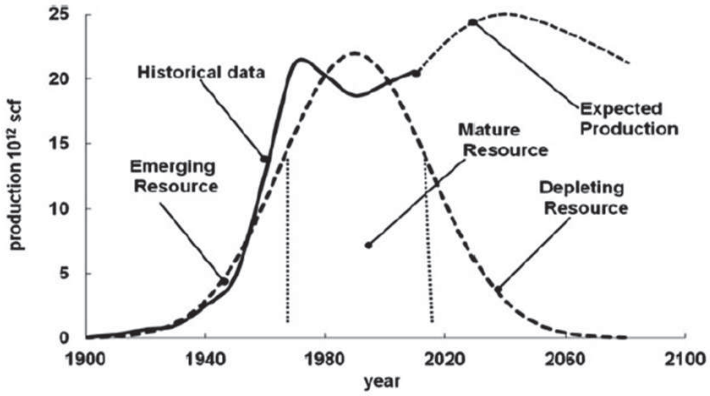

Figure 1.2: Standard cubic foot (scf) gas production vs years with the Hubbert curve life cycle[3]

Second, the security on energy supply must be guaranteed. The States can not be dependent by a fossil fuels coming outboard as it makes the states economy vulnerable to the foreigners.

Third, it's likely that using fossil fuels changes the climate. Climate change is blamed on several human activities, but the biggest contributor to climate change is the increase in greenhouse effect produced in major part by carbon dioxide (CO_2). It must be noted that the term greenhouse effect is neither new nor a product of the twentieth century environmentalists. The effect was first predicted analytically by Jean-Batiste Jaques Fourier, in 1824 and was verified experimentally in the laboratory by the British physicist John Tyndall in the 1850s after quantitatively validated for the atmospheric temperature in the 1890s by S. Arrhenius.

Nowadays, the accurate climate models to study quantitatively the greenhouse effect and its consequences on the planet Earth converge in predicting a significant average global temperature rise (at different values) accompanied by significant regional changes of the temperature and severe weather changes that have the potential to disrupt the human economic activities.

The increases of the Earth temperature could be described using a simplified

model (Fig.1.3) of the energy balance of the Earth coupled with the closure equations

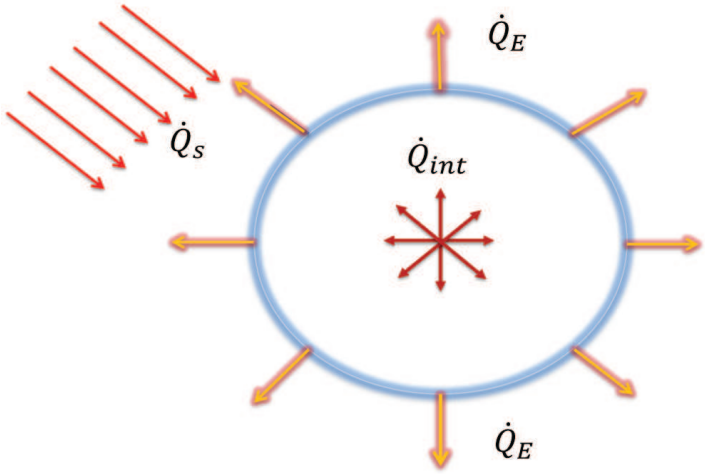

Figure 1.3: The Earth's surface layer as a closed system and the heat balance

of the radiation and conduction assuming the atmosphere thickness (H) very small in comparison to the radius of the Earth (R):

$$\begin{aligned} m_E c_E \frac{dT_E}{dt} &= \dot{Q}_S - \dot{Q}_E + \dot{Q}_{int} \\ 4\pi R^2 H \rho c_E \frac{dT_E}{dt} &= 4\pi R^2 \sigma \alpha_E T_S^4 - 4\pi R^2 \sigma \epsilon_E T_E^4 + 4\pi R^2 \sigma k_E \frac{(T_{int} - T_E)}{H} \end{aligned} \tag{1.1}$$

with, $\dot{Q}_S$ the rate of the primarily heat received from the Sun, $\dot{Q}_E$ the radiates heat in all directions, $\dot{Q}_{int}$ the internal additional power due to the nuclear reaction, ρ the average density of the atmosphere, σ is the Boltzman constant, T_{int} the interior temperature of the Earth, T_E the average Earth's surface, α_E the Earth's absorbtivity and ϵ_E the Earth's the radiation emissivity.
The system described by the equations 1.1 reaches a constant temperature T_E assuming a constant value for the three rates of heat over a long period of time. However, if any parameter of the system is perturbed, one or more of the three heat rates will change, the non-linear system will undergo a transient process and will reach a new equilibrium state with a different temperature T'_E.

In particular, an increase in the Earth's average radiative absorption (α_E) would cause an average temperature increase, while a decrease of α_E, would cause an

average temperature decrease. Such variations of the average atmospheric temperature will inevitably result in regional and global climatic changes with significant and, probably, adverse effects on the environment, the ecosystems and the human population.

In terms of the simplified model described by equation system 1.1, the net effect of the presence of the greenhouse gases (GHG's) is a decrease of the Earth's radiation emissivity (ε_E) due to the absorbtion of the Earth radiation (in the infrared spectrum) by the GHG. This reflects a fraction of the heat rate $\dot{Q}_E$ back to the surface layer of the Earth. The immediate consequence of this reflection is that the current temperature of the surface layer is higher than what would have been in the complete absence of the GHG's.

In case GHG's were entirely absent from the atmosphere, the heat losses $\dot{Q}_E$ would have been significantly higher because the average emissivity of the Earth (ε_E) would have been much higher than its present value. Hence, the Eqs.1.1 would predict a lower surface temperature T_E than the current average temperature.

The GHG's may be likened to a blanket around the Earth that keeps the planet warm. If this blanket becomes too thick, the inside temperature will increase and will cause several regional and global long-term effects that are unwanted and detrimental. The 40% increase of the CO_2 concentration in the last three centuries and, especially, the highly accelerated increase of this parameter in the last fifty years, as seen in Fig. 1.4, are causing the Earth atmosphere to become significantly thicker.

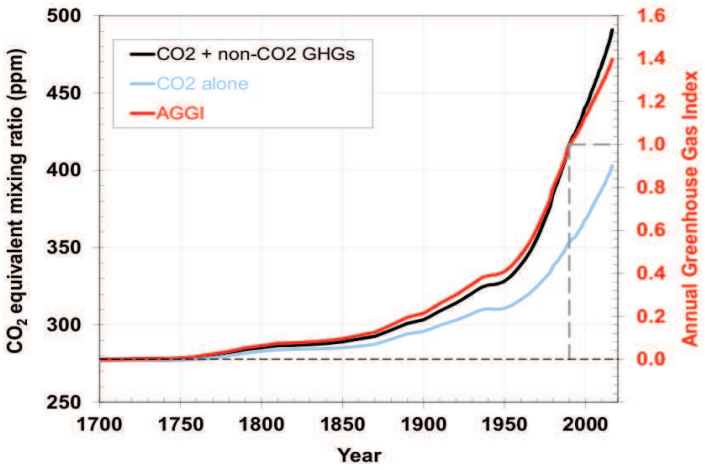

Figure 1.4: Data from Mauna Loa Observatory

Most of the carbon dioxide emissions come from fossil-fuel burning to produce energy. So to fix climate change, it's necessary to sort out a new way of getting energy which require energy system planning on an international scale.

The International Energy Agency(IEA) is an autonomous body within the framework of the Organization for Economic Co-operation and Development(OECD). Its purposes is to act as an energy advisor to the 29 member countries of the OECD. Every year the IEA publishes its report "World Energy Outlook" to promote energy security among its member countries through collective response to physical disruptions in oil supply and provide authoritative research and analysis on way to ensure reliable, affordable and clean energy for member countries and beyond; in addition the Energy Technology Perspectives (ETP) report is an annual study of energy technology and innovation to accelerate climate action.

The focus of ETP is the 2°C Scenario (2DS), which describes an energy system consistent with emissions trajectory that limit the average temperature increase to 2°C by the end of the century in order to avoid the worst consequences of global warming. A two degree warming scenario translates to deep cuts in emissions, as much as 70% by 2050, with a decarbonized or even carbon negative economy by 2100, according to the Intergovernmental Panel on Climate Change (IPCC). IPCC also suggests that such deep cuts would not affect economic growth. The sustainable development is like a table with three legs: development is not sustainable if it is not economically, environmentally and social sustainable. A technology that is perfectly clean but not economic is not sustainable, a technology that is perfectly clean but not economic is not clean.

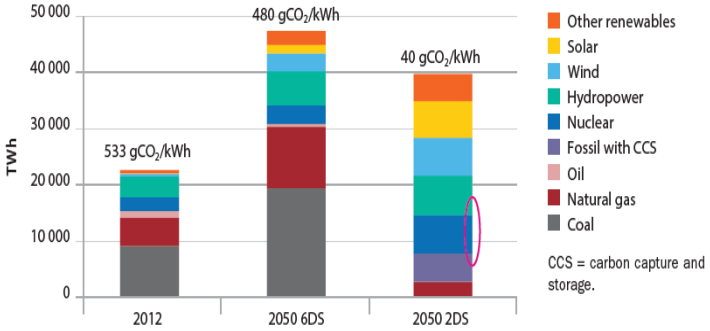

Figure 1.5: From IEA/NEA 2015

The Fig. 1.5 shows how the contribution of the all energies resources to emission

reductions would play out in terms of total global electricity production under the 2DS scenario to 2050. In particular, it's pointed out the important role played by the Nuclear energy: it would represent the single most important low-carbon electricity generating technology by 2050.

In this scenario the fusion technology doesn't appear as it is considered just a new technology: over the past two decades the operation of a series of experimental devices has enabled considerable advances, however the plasma created in current prototype devices is not significant enough to achieve sustained power.

The Intenational Thermonuclear Experimental Reactor (ITER) is a new, significantly larger prototype fusion device designed to demonstrate the scientific and technological feasibility of the fusion energy on a large scale. As fusion will not be employed for commercial electricity production until at least the second half of the century it is not considered in the ETP 2015 scenarios.

The European Fusion Development Agreement (EFDA) has promoted socio-economic research on fusion to investigate both the social acceptability and the economic competitiveness of fusion power plants in a future energy market. The results reported in [4], derived with the global energy model EFDA Times, shown the penetration of the fusion technology as energy source with 33% to the global electricity generation system by 2010(Fig.1.6a) for the Basic scenario providing a limit of 550ppm to GHG concentrations and assuming the availability of fusion energy from 2050.

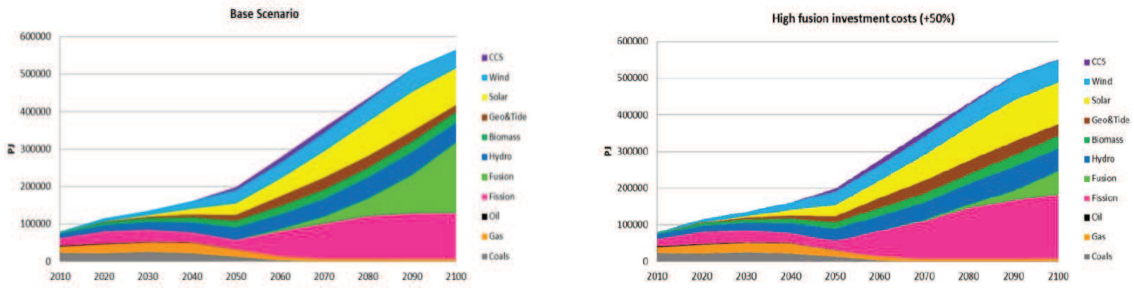

Figure 1.6: Fusion share in the global electricity system for basic scenario (on the left) and increasing 50% the fusion plant cost (on the right)[4]

A sensitive analysis has been performed considering different scenario taking into account for example lower and higher operation and maintenance costs as well as higher investment costs to build a fusion plant[4]. In particular a condition with a

fusion plant cost 50% higher than the base scenario induce a drastic reduction of the fusion power production up to only a third of the production in the Base scenario in 2100 as shown in Fig.1.6b.
This is an evidence of the importance of the fusion plant study in terms of the technologies with the related cost.

1.2 The thermonuclear fusion and Tokamak

The production of energy from nuclear reaction is based on the differences in the nuclear binding energy per nucleon (proton or neutron). It has been derived from measurement of the masses of the nuclei, when it was observed that the masses of nuclei are always smaller than the sum of the proton and neutron masses which constitute the nucleus.

This mass difference corresponds to the nuclear binding energy according to Einstein's energy-mass relation $E = \Delta \cdot c^2$. Consequently, it should be possible to obtain nuclear energy either by fission of the nuclei of the heaviest elements or by fusion of the lightest ones (see Fig.1.7).

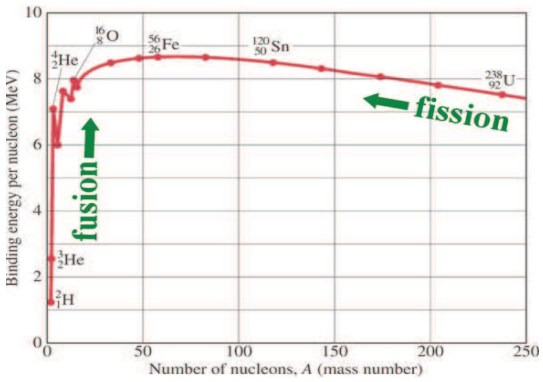

Figure 1.7: Bending Energy per nucleon in MeV vs the number of nucleons

The energy release per nucleon is of the order of 1 MeV for fission reactions and in the order of a few MeV for fusion reactions. This is 6/7 orders of magnitude above typical energy releases in chemical reactions which makes the attractiveness of the nuclear power.
In the fusion reaction, before the positively charged nuclei can be brought close enough together (less than 10^{-15} m) for fusion to take place, sufficient energy must

be supplied to overcome the force of electrostatic repulsion between them. This force is proportional to the product of the nuclear charges and so it increases as the atomic numbers of the interacting nuclei increase.

Hence for nuclei carrying a given amount of energy, the rates of the fusion reactions decrease, in general, with increasing the atomic number. It is only with the very lightest nuclei, those of hydrogen and helium isotopes, that conditions appear to be attainable under which the fusion reactions become fast enough to have the potential practical value.

The most important fusion reaction in the world, allowing the life in the earth, is in the stars. In particular, in the Sun about 680 million of tons of H are burnt every second and converted in H_e with a generation of $3.8 \cdot 10^{23}\ kW$ of energy. The dominant mechanism is the proton-proton fusion chain reaction in which helium is formed out of hydrogen releasing an energy of 26.7 MeV for each reaction. The chain reaction is so slow that a complete conversion of star's hydrogen would take more than ten billions years. In the sun, this fusion process is possible due to the high core density ($\sim 10^{31}\ m^{-3}$), sustained by the gravitational force. This is not attainable on earth, since densities in this range cannot be reached.
The measurements of the cross sections ($< \sigma v >$) of reactions involving light nuclei, reported in Fig.1.8, showing that the only way to exploit fusion process on the earth which offer any promise of producing more energy than expended in bringing them about, except for a possible combination of deuterium and the rare helium-3, is that involving the two heavier isotopes of hydrogen, namely deuterium and tritium (reaction 1.2).

$$D + T \rightarrow {}^4H_e(3.5\ MeV) + n(14.1\ MeV) \tag{1.2}$$

Despite the D-T curve has a maximum around a particle energy of 100 keV (Fig.1.8) , the mean temperature needed to have a sufficient number of reactions in a future fusion reactor is $\sim 10\ keV$. This comes from the ignition condition when all energy losses are compensated by the $\alpha-$particle from the fusion reaction for which the fusion product of the density (n), the temperature (T) and the confinement time (τ) must satisfy the following condition:

$$nT\tau > \frac{12kT^2}{< \sigma v > -4c_1 Z_{eff}(kT)^{1/2}} \tag{1.3}$$

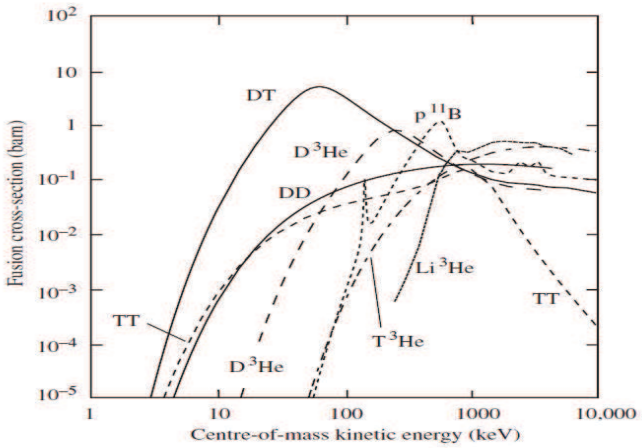

Figure 1.8: Fusion cross sections versus centre-of-mass energy for reactions of interest to controlled fusion energy. The curve labelled DD represents the sum of the cross sections of the various branches of the reaction

where Z_{eff} is the effective charge of the plasma and c_1 the bremsstrahlungs constant. The RHS of the Lawson condition in 1.3 has a flat minimum of about $3 \cdot 10^{21}$ [$s\ keV/m^3$] around 10 keV.

The temperature required is about ten times the core temperature of the sun: at this temperature atoms are ionized. The state of this hot, ionized gas is called "plasma". This matter state consists in a globally neutral system of many charged particles, which is characterized by presenting collective behavior: in sense that the particle motions depends not only on local condition but also on the plasma state in remote regions due to the long range action of the Coulomb force. The main results, often, will be derived in the "collisionless" regime in which the local forces, due to the ordinary local collisions, can be neglected with respect to the long-range electromagnetic forces.
The Lawson criteria in 1.3 dictates the strategy for developing fusion power as an energy producing system: attain temperatures of around 10 keV and achieve the required density and energy confinement time simultaneously. At the moment, two mechanisms to achieve fusion processes are being studied:

- the hot plasma is confined by strong magnetic fields with a density in the order of $10^{20}m^{-3}$, which is 10^5 times smaller than the atom density of a gas under normal condition, with the energy confinement time in the range of $2-4$

seconds as required by the Lawson criteria 1.3.

- the other extreme intends to reach a very high density and temperature of a Deuterium-Tritium target using high power lasers, causing an implosion. In this case the confinement time is extremely short: it is the time required for the particles to leave the hot implosion center. Since it is the mass inertia which causes the finiteness of this time, this approach to fusion is called Inertial Confinement Fusion(ICF).

The main approach nowadays in fusion research is based on the magnetic confinement. The plasma, consisting of a charge particles, can be confined by strong magnetic fields, but in linear configurations (e.g. magnetic bootle) the end losses are by far to large to reach the necessary energy confinement time τ_E of the order of seconds. These end losses can be completely avoided in a toroidal system.

However, in a simple toroidal system with purely toroidal magnetic field, the magnetic field curvature and gradient result in a vertical drift which is in oposite directions for ions and electrons. The resulting electric field coupled with the magnetic field cause an outward drift of the whole plasma, and therefore such a simple magnetic configuration will be unstable. To avoid this charge separation, it is necessary to twist the magnetic field lines by additional magnetic field components. A poloidal component is therefore added, so the main particle trajectory becomes helical, keeping most of the plasma in the central part of the torus Fig.1.9.

The magnetic field generates nested surfaces, the flux surfaces, characterized by constant magnetic flux and pressure. On these flux surfaces, plasma transport is fast, as it is always parallel to magnetic field. Perpendicular to the flux surface, transport is hindered by the Lorentz force which imposes to charged particles a circular motion around the field lines and therefore plasma parameters can vary strongly in this direction.

In this configuration the pressure increases perpendicularly to the flux surfaces confining the hot plasma in the centre of the torus. In the core region of a fusion reactor, it is thus possible to achieve the conditions necessary to heat the plasma up to about 10 keV reaching the Lawson condition 1.3.

Among magnetic confinement devices, three main configurations can be distinguished: tokamak , reversed field pinch and stellarator. The first two create the poloidal magnetic field with an induced plasma current, the latter uses complex

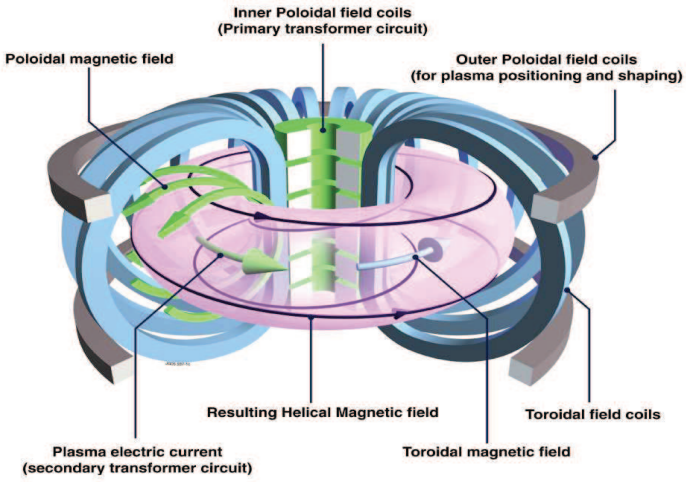

Figure 1.9: Tokamak concept. The innermost cylindrical coil (*Primary transformer circuit*) is the transformer coil for inducing a plasma current. The toroidal coils above and below the machine create a vertical field for plasma shaping and control the machine.

shaping of the magnetic field coils to generate directly helically twisted magnetic field lines.

The tokamak (from TOroidal'naya KAmera s MAgnitnymi Katushkami- toroidal chamber with magnetic coils in Russian) represents the most advanced fusion concept. It is the most used and studied configuration, and, at the moment, the most promising one for next step fusion reactors: with this configuration, parameters needed for fusion have been reached, but not all at the same time for a sufficient duration to obtain an energy gain.

1.3 The Fusion Power Plant and current drive efficiency

Pioneering work on Fusion Power Plant (FPP) must be credited to the USA, in particular to the ARIES team, who carried out a series of tokamak FPP studies between 1986 and 2000 (ARIES-I, II, III and IV, PULSAR, ARIES-RS and ARIESAT).

In Europe, after a preliminary series of study from 1990 to 2000, within the European fusion programme, demonstrating the safety, environmental and economic potential of fusion power a more comprehensive and integrated study started in the mid of 2001: the European Power Plant Conceptual Study(PPCS) for commercial fusion power plants.
During four years, in the mid of 2005 five power plant tokamak models have been designed, named PPCS A,AB,B,C and D[5]. The first three models were developed considering limited extrapolations of the knowledge both in physics and technology. Instead, regarding the other models, advanced physics scenarios have been identified and combined with advanced blanket concept that allow higher thermodynamic efficiencies of the power conversion system.
All models meet the overall objectives of the PPCS (design, safety,economics) and it can be concluded that a first generation fusion power will be economically acceptable, with major safety and environmental advantages by appropriate design and material choises[6][7][8].
One important outcome of the conceptual study of a fusion power plant (FPP) is the identification of key issues and of time-line for their resolution prior to the construction of the first plant. Europe has elected to follow a 'fast track' in the development of fusion power [9], with two main devices prior to the first commercial power plant: ITER and DEMO. These devices will be accompanied by extensive $R\&D$ and by specialized machines to investigate specific aspects of plasma physics, plasma engineering, materials and fusion technology.
Nowadays with the construction of ITER well underway, attention is turning to the design of a successor device that should be the nearest-term reactor design capable of producing electricity, operating with a closed fuel-cycle and to be the single step between ITER and the commercial reactor, namely: **DEMO**nstration fusion power plant.
The timing of realization are placed at the end of 2030/2035 close to the end of the ITER experiments with deuterium-tritium; the planned route is to define the conceptual design of the machine and at the same time to start the studies defining the parameters of this machine and the elements that allow define the operating conditions of the device.

The conceptual approaches for this demonstration reactor are essentially two:

- the Western European strategy supposed to take advantages from the first results of the ITER experiment, is oriented towards a pulsed reactor with the plasma characteristics not far from those of ITER. The design and construction are planned in a relatively short time (20-30 years). This device is not intended as a "commercial" reactor but as a "test bench", realized in terms of many Demo's, aimed at verifying physical and technological parameters inferred from the ITER experiments. Regarding Europe an important part of the roadmap to Fusion Electricity Horizon 2020 is devoted to a conceptual design study to explore a number of DEMO plant design options and to clarify what should be the objectives of the device and what $R\&D$ is required before the construction of an actual plant.
  The planned strategy foresees two phases. The first is aimed at realizing DEMO1 a pulsed "low extrapolation" device employing technologies, as far as possible mature, reliable regimes of operation (to be extrapolated from the ITER experience) and using materials suitable for the expected level of neutron fluence. The second phase is a steady-state option (DEMO 2) based on more 'advanced'and demanding performances requiring innovative technologies and advanced physical assumptions (identifying wether there are realistic possibilities). However, establishing performance requirements and realistic project cost estimates and development schedules are expected to be a strong driver in the selection of the technical features of the device. Safety also plays important role in the ultimate selection of plant design choices and operating conditions (e.g., choice of materials, coolants). Safety analysis must be constantly updated to match the evolution of the DEMO design.

- The strategy of Eastern Europe,Japan, India and China, is directed towards the construction of a fusion reactor (with characteristics close to those of a commercial plant) delivering a power of $1500MW$, capable of delivering electricity in the greed. Japan is following an even more "aggressive" program and has indeed developed the SlimCS (small central solenoid) reactor with a fusion power of approximately 3000 MW, as its next fusion facility project.[1]

[1]However, more recently the country seems to be more oriented toward a new design, with a fusion power varying between 1300 and1500 MW.

The western and eastern conceptions of DEMO can be traced back to a common origin, associated with the formula defining the fusion power in terms of geometrical and plasma machine parameters:

$$P_{fus}(MW) = 1.1\beta^2(B_t[T])^4\ V[m^3] \tag{1.4}$$

being $V = 2\pi R\pi a^2 = 2\pi^2 \frac{R^3 k}{A}$ the torus volume, where $A = R/a$ is the aspect ratio, $k = a/b$ with b the major radius and β the kinetic to magnetic pressure ratio

$$\beta = \frac{nT}{B_t^2/2\mu_0}$$

According to eq.(1.4) it is evident that, for a fixed fusion power, increasing the e.g. β value we can reduce the volume of the machine and therefore the cost of the reactor. A further key parameter to define fusion power is the normalized β_N defined through the identity

$$\beta = \beta_N \frac{I}{aB}$$

where β_N changes with current and pressure profiles. Its maximum achievable values range between $4 \div 5$ according to the limits imposed by the occurrence of MHD instabilities in plasma.
Redefining β in terms of β_N eq. (1.4) can be rewritten as

$$P_{fus} = \beta_N^2 \left(\frac{I}{aB_t}\right)^2 B^4 2\pi^2 R^3 \frac{k}{A^2} = \beta_N^2 I^2 B_t^2 2\pi^2 \frac{R^3}{a^2}\frac{k}{A^2} = 2Rk(\beta_N I B\pi)^2 \tag{1.5}$$

Therefore the fusion power has a square dependence on β_N in turn constrained by the occurrence of MHD instability.
The two approaches for the construction of DEMO reactor can be therefore identified with the working point of β_N as specified below :

- The Eastern Europe strategy is a design fixing the operating point of the reactor at β_N values close to the critical limit. This choice allows to work with a highly unstable plasma, on the other side reduces the machine cost, since P_{fus} scales linearly with the torus major radius and quadratically with β_N. A further benefit in the direction of cost reduction is determined by the on set of self generated plasma currents (boostrap currents)[2] which are estimated to cover 80% of the total amount necessary for a steady-state operation.

[2]The bootstrap current is a current parallel to the magnetic field that is driven by the radial pressure gradient through the pressure anisotropy it generates in an inhomogeneous magnetic field.

- the Western Europe strategy is based on a design foreseing a β_N far from the critical value with most of the inductive current generated by the central solenoid and a limited use of additional heating systems necessary to achieve the plasma ignition. This choice naturally involves a pulsed reactor (with a long pulse of about 6 hours) with considerable size necessary to support the dimension of the central solenoid generating the inductive current.

The difference among the five DEMO reactor models reported in figure (1.1) lies essentially on the choices of the different values of β which is related to the bootstrap current fraction contributing to the plasma heating by a further pivotal parameter defined below

		EUROPE(Power Plant Conceptual Study)		USA	JAPAN	RUSSIA
	ITER(SS)	Mod-A	Mod-B	ARIES-AT	DEMO-slim CS	DEMO-S
$P_{thermal}$=1.18 P_{fus}(GW)	0.36	5.9	4.2	1.9	3.6	2.9
P_{el_net}	0	1.5		1	1	0.7
η_{th}	==	25	36	53	28	24
R0(m)	6.2	9.5	8.6	5.2	5.5	7.8
A	3.1	3		4	2.6	5.2
b/a	1.7	1.7	1.7	2.2	2	1.85
B_t(T)	5.3	7	6.9	5.3	6	7.7
I_p(MA)	9	30	28	12.8	16.6	11.2
f_{GW}	0.75	1.2	1.2	1.1	0.98	0.98
H_H	1.5(ITB)	1.2	1.2	1.4	1.3	1
$\beta_{N,th}$	2.9	2.8	2.7	5.4	>3.5	4.7
I_{bs}/I_p	0.5	0.45	0.43	0.91	0.77	0.59
$q_{div,rel}/q_{ITER}$(at P_{rad}=80%)	1 (eq. to 4.8 MW/m²)	4.6	4.3	3.3	5.7	3.1
P_{heat}/R_0(MW/m)	22.5	130	115	68	121	78
P_{aux}(MW)	33+40	246	270	35	60	117

Table 1.1: In this table from [10] are highlighted the strong extrapolation as compared to EU guideline; aggressive scenario exist also for EU PPCS but not reported here(nowadays for DEMO2 β_N is set to 3.8). From the parameters reported here we can see that the major radius of the pulsed model (Mode-A) is around double of which related to the steady-state reactor as well as the β_N value is much lower. Furthermore the power on the divertor for booth steady-state and pulse reactor is around five times greater than that of ITER.

$$f_B = \frac{I_b}{I_p} = 0.022 q_{95} \sqrt{A} \beta_N \tag{1.6}$$

being I_p the plasma current, I_b the bootstrap current and q_{95} is the safety factor[3] value at the plasma edge more precisely at 95% of plasma minor radius. In the

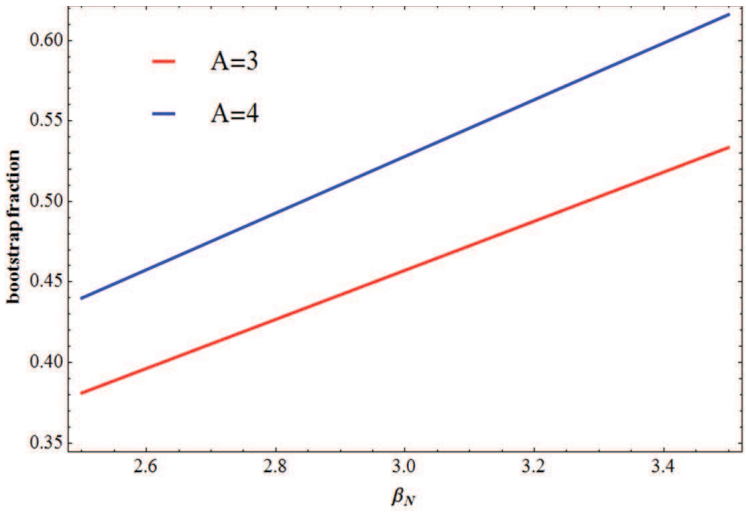

Figure 1.10: The bootstrap current fraction versus β_N at a fixed value of $q_{95} = 4$ for different value of the aspect ratio A

figure (1.10), showing the behavior of f_B versus β_N for two different values of A, we can see that to have a high value of f_B we must increase the A values ($\approx 4 \div 3.5$) as well as those q_{95} at the boundary ($\approx 4 \div 5$) and fix $\beta_N \geq 3$.
The linear dependence of the bootstrap current fraction on q_{95} doesn't allow to raise this value indefinitely since it is inversely proportional to the current (from Eq. 1.7) and below a certain current values the fusion power becomes too small. A scaling relation connecting the safety factor to the machine parameters is given below

$$q_{95} = \frac{5a^2 B}{RI} f(k, \rho, A) \tag{1.7}$$

being $f(k, \rho, A)$ a function of the plasma elongation k, triangularity ρ and aspect ratio A.
All DEMO reactors must have gain factor Q (the ratio among the fusion power and the heating power) around 30 unlike ITER, for which $Q = 10$ is expected[4].

[3] q is the toroidal angle covered by a field line when it performs a full poloidal turn

[4] ITER is indeed not expected to deliver any power in the electric network

The Q value has a strong dependence on the γ_{cd} factor which is the Current-Drive efficiency (CD), namely the CD efficiency is the ratio between the produced plasma current and the effective heating power. The following formula puts in relationship the fraction of bootstrap current with Q

$$Q = \frac{P_{fus}}{P_h + \frac{\overline{n_e} R I_p}{<\gamma_{cd}>}(1 - f_{bs})} \quad \text{with} \quad I_p = I_{CD} + I_{bs} \text{ and } \gamma_{cd} = \frac{\overline{n_e} R I_{CD}}{< P_{cd} >} \tag{1.8}$$

being f_{bs} the bootstrap current fraction, P_h the heating power, I_p the total plasma current with the discharge of the central solenoid set to zero ($V_{loop} = 0$).
Fig.1.11 shows the gain Q versus the fraction of the bootstrap current for different values of the current drive efficiency ($\gamma_{CD}[A\ W^{-1}\ 10^{20}\ m^{-2}]$), the best condition is at the ignition($P_h = 0$) for which $Q = \infty$ and $f_{bs} = 1$.
Furthermore, we can see for different current drive efficiency the amount of the current drive fraction necessary to reach a fixed Q value. In case of $Q = 20$ the more realistic condition is to consider a low value of the current drive efficiency (~ 0.3) increasing the fraction of the bootstrap current value (~ 0.8)[14].

Furthermore for the steady-state reactor to generate an high bootstrap current

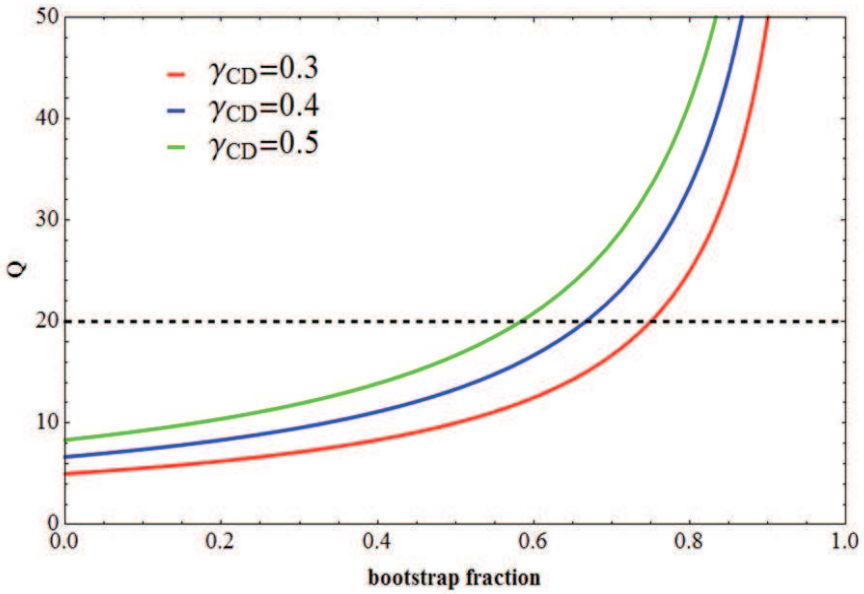

Figure 1.11: The Q gain versus the bootstrap current fraction for a fixed major radius $R = 7.5\ m$, plasma current $I_p = 20\ A$, fusion power $P_{fus} = 2500\ MW$ and heating power $P_h = 0$.

fraction we must have a very high pressure gradient profile reported in fig.1.12 reproduced from [11].

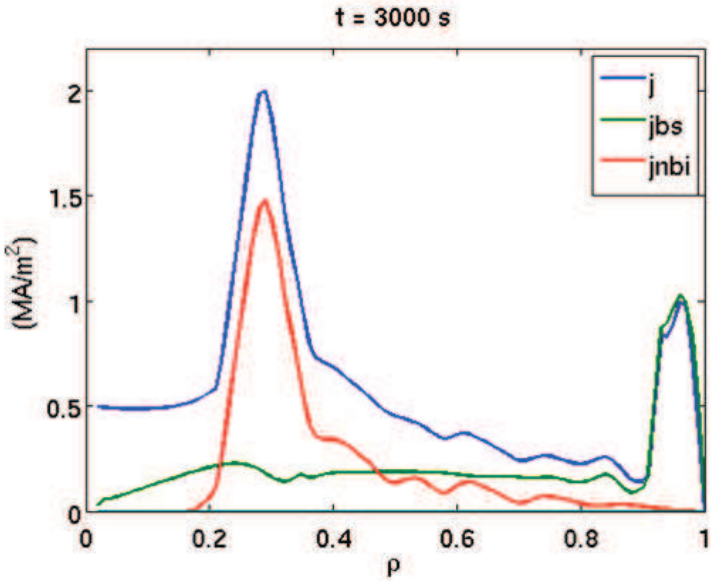

Figure 1.12: The different contributions to the plasma current simulated with CRONOS for a pulsed DEMO scenario[11].

However some physical issues have to be solved for a steady-state reactor:

- compatibility of high density with high confinement: it has been demonstrated that a useful tool to get this compatibility is producing highly shaped discharges (high elongation and triangularity) ;
- compatibility of high plasma purity and high radiation fraction needed to alleviate the divertor heat load ; within such a framework a proposed solution is impurity seeding to increase emission of radiation and plasma detachment in the divertor;
- compatibility of large beta values with high confinement: the mechanisms of stabilization of MHD modes can rely on plasma rotation and active coils;
- alpha/fast ion confinement: the discharges with shear reversed q-profile can trigger Alfvenic instabilities at shot time scales which can produce sudden loss of confinement of fast ions. This has been demonstrated in a series of experiments on JT-60U.

Regarding the technical issues it will be necessary to have current drive(CD) systems capable of delivering power in steady state and to be used in feedback control loops to achieve discharges with $f_B \approx 0.7 - 0.9$. The limited efficiency of the CD systems imposes that the electricity power, produced by the reactor to be recirculated to run these CD systems, could be a substantial fraction of the produced power (of the order of 20% or more). It will be useful to revisit the ECRH system source at high frequency high power, now provided by Gyrotron, trying to increase the system efficiency.

An important role for a steady state DEMO reactor is played by the measurement and control the current and pressure profiles: the reason is due to the need of the MHD stability which has to be controlled by a careful choice of these profiles. In a DEMO environment it is not clear if it is possible to export the diagnostic system used for the present tokamaks (including polarimetry, motional stark effect, MHD spectroscopy, interferometry, Thomson scattering). Furthermore, a large fusion output imply the capability of dealing with plasmas with high radiation fraction and strong heat and neutron load on plasma facing components. A more complete and recently overview of the DEMO design approach can be found in [12].
An idea of the physics dimensions can be inferred from a look to the formula related to cost of electricity (CoE) generated by a fusion reactor, namely

$$CoE \sim \left[\frac{1}{\mathcal{A}^{0.6}\eta_{th}^{0.5}}\right]\left[\frac{1}{R^{0.4}}\frac{1}{(B*I)^{0.8}}\frac{1}{(\beta_N)^{1.2}}\frac{1}{(n/nG)^{0.3}}\right] \tag{1.9}$$

being, the reactor availability $\mathcal{A}$ the ratio among the reactor life time and the working time, the thermodynamic efficiency η_{th} the ratio among the the fusion energy and the produced electric energy [13].
According to the previous relation, the costs can be broken in two parts:

- The first on the left specified by the reactor availability A and by the thermodynamic efficiency (η_{th})
- The second links the various design parameters of the whole device, being nG the Greenwald density limit.

The parameters entering the previous relations have not all separated functions. According to Eq. 1.9 a naive conclusion could be that it is economically convenient

to operate with β_N as large as possible (see Fig.1.13), in order to minimize the external current drive whose generation systems have low efficiency, and with a plasma density close to Greenwald density limit.

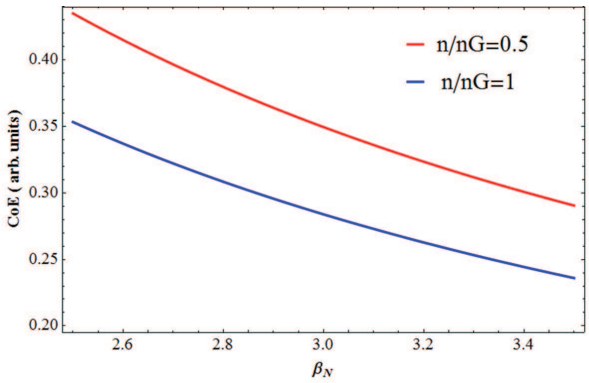

Figure 1.13: The CoE value versus β_N at the fixed $R = 7.7\ m, I = 9.5\ MA, B = 5.5\ T$ for two different values of the density fraction related to the Greenwald density limit.

Above the ignition value, see fig. 1.14, the DEMO size is the most important feature mainly determining relevant economical attractiveness.
Below ignition threshold heating power has to be supplied in order to sustain the fusion reaction, making the plant less attractive. The general rule that can be derived is "the bigger is the more economically convenient"[14]. The DEMO dimensions depend on different elements, hereafter summarized

- ignition prescribes the minimum major radius fig. 1.14
- the pulse length suggests larger R and P_{fus}

The preliminary conclusions, drawn in five years of PPCS are:

- the plasma physics investigation is especially important for β_N and for the Greenwald density fraction n/n_{GN};
- based on the present tokamak physics base, steady state should be abandoned from the DEMO objectives but kept as an important goal.
  Demo should not be conceived as an economically competitive device, rather it should be considered as a guiding tool allowing the proper understanding

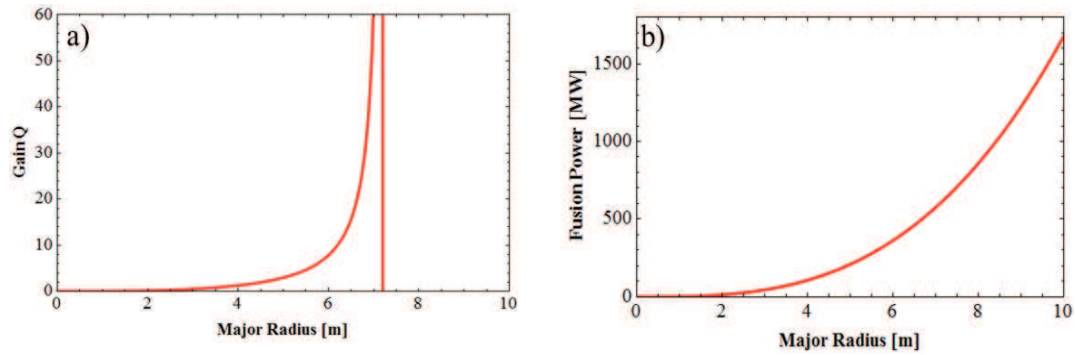

Figure 1.14: The fusion gain (a) and the fusion power (b) as a function of the reactor size.

of the features determining the economic potentials of a fusion power plant, by providing the proper hint to determine the size, the pulse length (see 1.15) and further criteria to optimize engineering and physical parameters;

- technology progress especially important for toroidal magnetic field (B_t) and the current drive efficiency (η_{CD}).

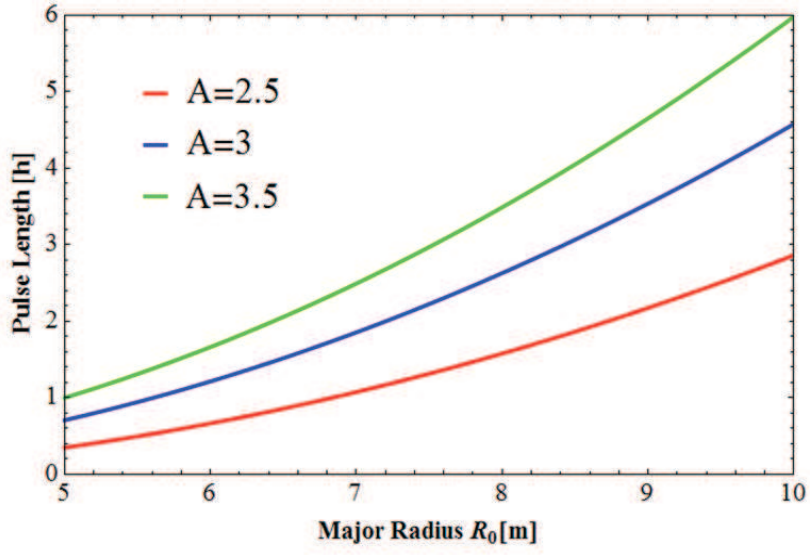

Figure 1.15: The pulse length as a function of the major radius for a fixed plasma current $I_p = 19MA$, toroidal magnetic field $B_t = 6.5T$, the density Greenwald fraction $n20 = 1$ for different values of the aspect ratio $A = R/r$.

1.4 The ECRH/ECCD requirements in a Tokamak Plant

The requirements on plasma pressure and confinement time to reach ignition find a minimum for a plasma temperature of $10keV$ (Eq. 1.3). Calculation of the reaction rate using a Maxwellian distribution function shows that the alpha heating becomes dominant for $T > 5 - 7\ keV$ while below the contribution from fusion power is almost negligible (see Fig.1.16). In order to reach this temperature, other heating sources are essential.

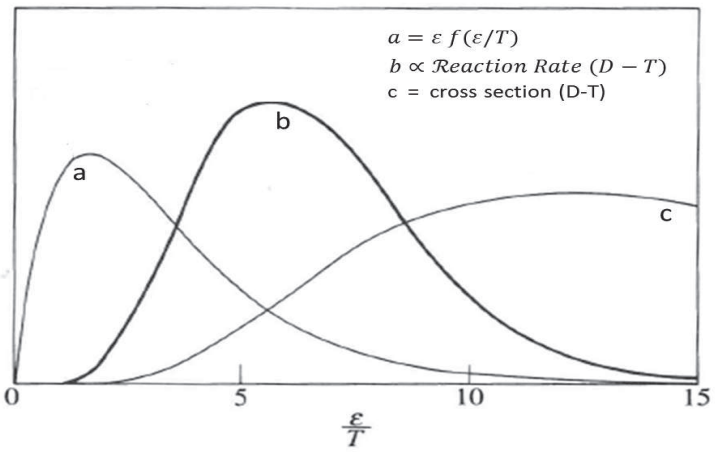

Figure 1.16: The reaction rate per unit of volume (b) versus ϵ/T (the energy of the bombarding particle ϵ over the plasma temperature) together with the particle distribution function (f) multiply by ϵ (b) and the cross section (c) of the D-T plasma reaction at T=10keV. At this temperature the reaction rate become predominant from the tail of the distribution (b) and far from the maximum of the reaction cross section(c).

In case of a tokamaks the easiest way to increase the plasma temperature is through the ohmic heating but unfortunately this is not sufficient. Plasma is a conductor, and the flowing of a plasma current produce heating ($P = \eta j^2$ with η the resistivity and j the current density). However plasma resistivity decreases with temperature ($\eta \propto T^{-3/2}$) and this limits the efficiency of ohmic heating, which alone may lead to a maximum plasma temperature of $3\ keV$ for typical reactor parameters. The resulting temperature gap must be filled by auxiliary heating systems and without them it is not possible to ignite a reactor.

In order to meet the auxiliary heating power requirements expected for tokamak reactors, a broad-based experimental physics and technological development program has been in progress for a number of years to evaluate the potential heating methods. From these studies several promising candidates have now emerged. As the basic physics of each of these methods has become better understood the important criteria for evaluating the viability of any scheme has becomes increasingly related to its projected cost and efficiency, rather than on its technical characteristic alone and without to forget the Reliability, Availability, Maintainability and Inspectability (RAMI) analysis for all of them which is an important element to evaluate for a commercial reactor.

It is for this reason that, although the primary most successful auxiliary heating has been with neutral beam injection (NBI) throwing high energy particles in the plasma, RF heating methods have come under intense development due to the comparatively simpler rf power generation systems and projected favorable wave penetration and power deposition characteristic. In Fig.1.17 all the heating systems has been evidenced.

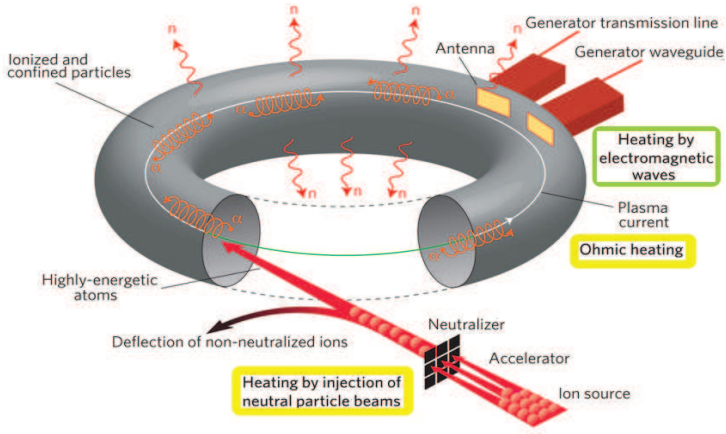

Figure 1.17: The three main additional heating systems for plasma in a Tokamak: radio frequency waves, neutral beam injection and plasma current with the central solenoid.

1.4.1 Energy transfer mechanism

The launched wave in the plasma will be damped simply because the accelerated particles experience a drag due to collisions. This is not the case of a hot plasma in the balk, where the temperature values are approximately $T_i \approx T_e \approx 5\ keV$ and the density value is $n = 5.0 \cdot 10^{-19} m^{-3}$, for which the derived collision frequency ν (1.10) is of the order of a few kHz.

$$\nu = 2.9 \cdot 10^{-12} n ln\Lambda T^{-3/2} \approx 20\ kHz \tag{1.10}$$

In the electromagnetic theory the ratio $\nu/(2\pi f)$ is characteristic of the importance of dissipative effects due to the collisions with respect to the wave oscillation. For small values of ν/ω, the motion is almost dissipation-less and huge fields and large perturbations in the particle motion are necessary if any significant amount of energy is to be damped in the plasma.

In the plasma, with the previous characteristics, the direct dissipation of the wave by collisions will be negligible at the frequencies in the MHz range or higher and in this case the resonance play the major role in the absorption. Under resonance conditions, a small excitation will create either a huge response in the particle's motion (wave-particle resonance) or large wave field build up (wave resonance). The two different mechanism determine the frequency and wavelength ranges of interest.

The first mechanism is based on the Landau dumping for which if the particle is to extract energy from the wave, the particle must experience a steady electric field in its own rest frame. Hence, in a situation where the particle has an initial velocity of magnitude V and in the direction $\hat{v} = \mathbf{V}/V$, and the component of the wave phase velocity in the direction in which the particle is moving is $V_{ph} = \omega/(\mathbf{V} \cdot \hat{v})$, the condition for interaction between the particle and the wave is $V = V_{ph}$, given by a dispersion relation derived by linearizing the Vlasov equation close to a give perturbed Maxwellian distribution[15].

In a steady magnetic field $\mathbf{B}_0$, the component of the particle's velocity along $\mathbf{B}_0$ is unaffected by the magnetic field, and the Landau resonance condition leads to $\omega - k_{||} V_{||} = 0$, being $V_{||} = \omega/k_{||}$ and $k_{||} = \mathbf{k} \cdot \mathbf{B}_0/B_0$. This resonance condition can be applied to two different physical damping mechanisms in a plasma depends on

the force type acting on the particle which determine the wave energy dissipation toward the particle:

- $F_{||} = qE_{||}$, if the wave has a component of the electric field and a component of the wave vector both parallel to B_0 the force allowing the wave-beam energy exchange is simply given by the electrostatic force when the Landau resonance condition is satisfied;

- $F_{||} = \frac{1}{2}(\frac{mv_{\perp}^2}{B_0}\frac{dB_z^w}{dz})$ due to the gradient in the component of the wave magnetic field (B_z^w) interacting with the magnetic moment of the particle (the z direction defined by the static magnetic field $\mathbf{B}_0$); in fact, for any slow variation of the magnetic field given for example by $B = (0,0,B(y))$ in the y direction the Lorentz force F averaged on the Larmour period acting on the particle assume the expression $< F >= -\frac{1}{2}mv_{\perp}^2 B_0'/B\mathbf{e}_y$. This is the so called transit time magnetic pumping (TTMP).

The second mechanism, due to the cyclotron damping, occurs when the wave electric field has a component perpendicular to $\mathbf{B}_0$. In this case the cyclotron resonance can increase the energy of the particle if the electric field vector has a circularly polarized component rotating at the same frequency with which charged particles are gyrating around $\mathbf{B}_0$ with the same handedness. The angular frequency of gyration is given by $\Omega = q\mathbf{B}_0/m$ (with q and m the charge and the mass of the particle respectively) and the resonance condition for resonance is:

$$\omega - k_{||}v_{||} = \Omega \tag{1.11}$$

The resonance frequencies (and cut-off frequency) of a launched wave into the plasma depend on plasma characteristics, such as toroidal magnetic field $\mathbf{B}_0$, plasma density and temperature. For the present tokamak experiments the typical resonance frequencies are in the range of $30 - 100\ MHZ$ for the Ion Cyclotron Resonance Heating (ICRH), $1 - 10\ GHz$ for the Lower Hybrid (LH) and $50 - 170\ GHz$ for the Electron Cyclotron Resonance Heating (ECRH).

In particular, the wave propagation in the electron cyclotron range of frequencies is generally well described by cold plasma approximation[16]. In this approximation the plasma pressure is assumed very small compared to the magnetic pressure. In this case the thermal motion of electrons may be negligible in terms of oscillations of

the wave $v_{ph} >> v_{th}$, where v_{ph} is the phase velocity of the wave and v_{th} is an electron thermal velocity and the Larmor radius is small compared to the wavelength. The plane wave solutions of Maxwell's equation in Fourier space give rise to a dispersion relation, known as the Appleton-Hartree equation, which leads to a condition for the refractive index $\vec{N} = \omega/c\vec{k}$.

In particular, for the case of perpendicular propagation to the magnetic field $\mathbf{B}_0$ ($N_{||} = 0$) the dispersion relation gives two different solutions for the $N_{\perp}$ component: the Ordinary mode (O-mode) for which the electric field component of the wave is parallel to $\mathbf{B}_0$ and the extraordinary mode (X-mode, that can propagate only inside the plasma as is not a transversal wave) for which the electric field component of the wave is perpendicular to $\mathbf{B}_0$.
The absorbtion of electromagnetic waves in the electron cyclotron frequency depends strongly on the parameters of the target plasma and on the mode and direction of propagation with respect to the magnetic field. The parameter characterizing the absorption for the most relevant modes is given by the optical thickness defined by

$$\tau = \int_0^l \alpha ds \tag{1.12}$$

where the integral is along the ray path s of the wave trajectory and the absorption coefficient α has the expression

$$\alpha = -2\vec{k''} \cdot \frac{\vec{v_g}}{v_g} \tag{1.13}$$

being $k'' = (\omega/c)N''$ the imaginary part of the wave vector $k = k' + ik''$ [17, 18].
The fractional power absorbed by the plasma in a single transit through the cyclotron resonance layer is then obtained by

$$P_{abs}/P_{inj} = (1 - e^{-\tau}) \tag{1.14}$$

We can see an illustration of the function P_{abs}/P_{inj} on the Fig.1.18 where it's shown that for $\tau > 3$ the fraction of absorbed power is greater than 95%.

The optical depth for a wave propagating in a tokamak can be derived using a plasma slab approximation in which the magnetic field varies as $\mathbf{B}_0 = 1/R$ and neglecting the relatively small poloidal magnetic field.
The analytical expressions of the optical thickness, derived for all the harmonics of the O-mode and X-mode, show a strong dependence from the electron density and

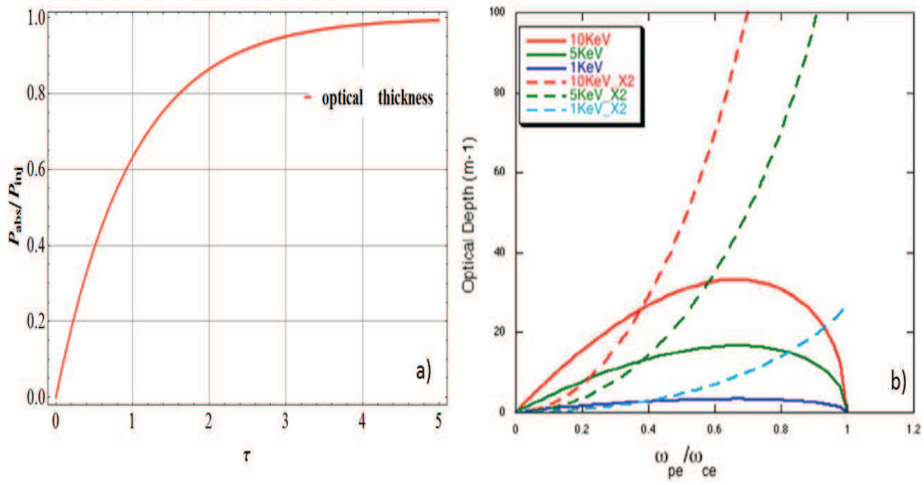

Figure 1.18: On the left a): the fraction of absorbed power as a function of optical depth; on the right b): the optical thickness of the O-mode and X-mode versus the plasma density at 140 GHz for different values of plasma temperature.

temperature [18].
In Eq.(1.15,1.16) has been reported for $N_{||} = 0$ the expression of the optical thickness for the two principal candidate modes that will be used to heat the plasma, the fundamental harmonics for the O-mode and the first harmonics for the X-mode:

$$\tau_{OM1} = \pi^2 \frac{\omega_{pe} * 2}{\omega_{ce}^2} \left(1 - \frac{\omega_{pe}^2}{\omega_{ce}^2}\right)^{1/2} \frac{V_{Te}^2}{c^2} \frac{R}{\lambda} \tag{1.15}$$

$$\tau_{XM2} = 2\pi^2 \frac{\omega_{pe}^2}{\omega_{ce}^2} \frac{\left(6 - \frac{\omega_{pe}^2}{\omega_{ce}^2}\right)^2}{\left(6 - 2\frac{\omega_{pe}^2}{\omega_{ce}^2}\right)^2} \frac{V_{Te}^2}{c^2} \frac{R}{\lambda} \tag{1.16}$$

being R the major radius of the tokamak and λ the injected wavelength and $V_{Te} = (k_B T_e/m_e)^{1/2}$ the thermal velocity of the electrons.
The main differences among the O-mode and X-mode are:

the O-mode polarized wave cannot propagate in a region where the plasma frequency is larger than the wave frequency, it means that to propagate the wave in a very high density plasma we need to increase the external magnetic field instead for the X-mode the fundamental harmonics is hidden by the cut-off from the low field side (LFS) and the first harmonics ($XM2$) has the same accessibility of the fundamental harmonics of the O-mode but the density cut-off is lower. The first harmonic O-mode will be attractive in devices with high temperature because of the

high cut-off density.

The second point that makes the differences between ordinary and extraordinary mode polarization is the absorption: in particular in booth cases the absorption is proportional to the density and temperature but for the first harmonic X-mode the absorption is stronger (with the increase temperature) than in the fundamental O-mode as reported in Fig.1.18b.

The required power for the ECRH system is influenced by the launching angle, the excitation mode whose absorption is determined by the plasma characteristic (density and temperature) 1.16. An estimation of the EC power needed during a plasma discharge for a DEMO pulsed reactor has been evaluated form a pulsed DEMO reactor in [19] and reported in Fig. 1.19.

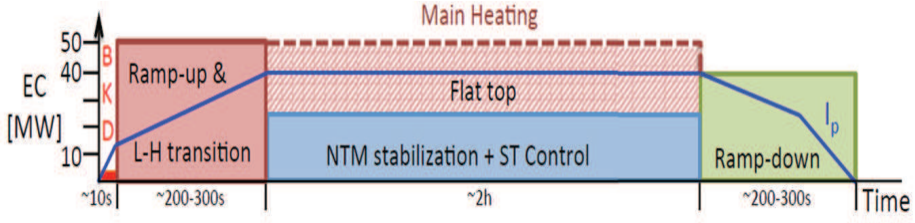

Figure 1.19: The auxiliary EC power along a DEMO pulse discharge phases [24].

1.4.2 Current Drive and instability dumping

All the heating systems, whose scheme is reported in Fig.1.17, not only heat the plasma but are also able to drive plasma current if expressly designed. This feature is particularly important for steady-state tokamak scenarios (advanced scenarios), where fully non-inductive currents flow in the plasma. In these advanced scenarios, auxiliary heating systems are the main actors for non-inductive current generation, together with the contribution of the bootstrap current, which is an off-axis current generated by the neoclassical transport and which depends on density and temperature gradients. Auxiliary heating systems are therefore the main actuators for plasma heating and current drive (CD).

The EC waves gives only perpendicular energy to electrons, no net longitudinal momentum transfer but it is possible to produce also current drive launched the

wave with an angle $\theta \neq 0$ between the wave vector $\mathbf{k}$ and the magnetic field $\mathbf{B}_0$. The Electron Cyclotron Current Drive (ECCD) efficiency is very low but the high localization can be exploited for current profile control aiming to MHD stability or q profile shaping.
The EC wave can produce non inductive current drive exploiting two different and opposite effects: the Fisch&Boozer effects acting on the collisionality and the Ohkawa effects related to the trapped particles balance.

Staring from the resonance condition in Eq. 1.17, injecting a wave into to plasma from the low field side (LFS) with a certain angle $\theta > 0$ ($\theta < 0$) the resonance will be up-shift (down-shift) (see Fig. 1.20) inducing an asymmetric increasing energy followed by a collisionality reduction with implies an asymmetric losses and a net co-current(counter-current) generation (Fisch&Boozer effect).

$$\frac{\Omega_{ce}}{\omega_0} = \frac{c/v_{||}}{\sqrt{c/v_{||}^2 - 1}} \left(1 - \frac{N_{||}}{c/v_{||}}\right) \tag{1.17}$$

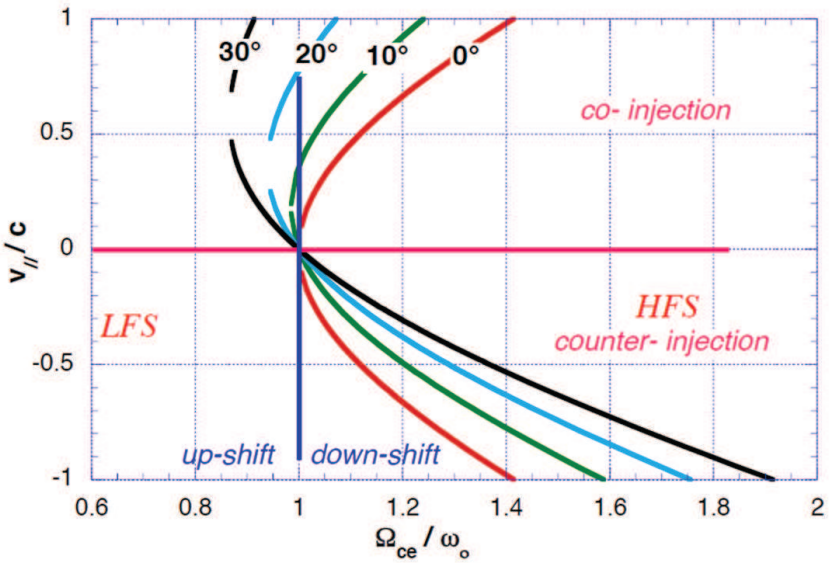

Figure 1.20: On left: schematic representation of the particles orbits inside a tokamak. On the right: the particle distribution orbit in the velocities (parallel and perpendicular to the magnetic field) where ε the ratio among minor and major radius of a tokamak

In the other hand, the particles gained transversal electric field from the injected wave can enter in the trapped cone, which define the condition for trapped particle

in a toroidal geometry (see Fig.1.21). The Ohkawa effect is based on the fact:

the particle moving in the trapped particle cone will not be more able to drive current (due to the bouncing of such particle in the trapped region) which create an asymmetry for the particles going in the opposite direction than does not absorb EC wave and continue to circulate. This asymmetry produce a net current drive term in the opposite direction with respect to the resonant electrons absorbing the wave.

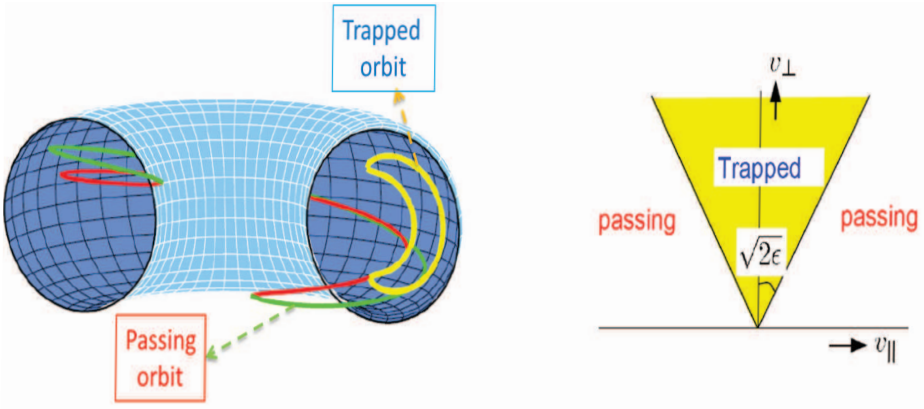

Figure 1.21

The important role is played by the current drive efficiency for a commercial reactor working in a steady-state condition. Two different figure of merit has been employed to investigate the current drive efficiency. The dimensional coefficient, reported previously in Eq.1.8, estimates the effect of the temperature variation on the total driven current and the dimensionless coefficient in Eq. 1.18 which take into account the local variation of the collisionality due to the wave particle interaction[20]:

$$\xi_{CD} = \frac{e^3}{\epsilon_0^2} \frac{n_e R_0}{T_e} \frac{I_{CD}}{P} \tag{1.18}$$

A deeply investigation on the optimization of the efficiency coefficients for a DEMO plasma has been reported in [21] where the launching condition and frequency are the main component affecting the efficiencies. The optimum beam frequency derived in [21] are in the range around 230 GHz for the steady-state and 290 GHz for pulsed operation.

In order to optimize the tokamak performance much attention has been focused on operational pressure limit imposed by non-ideal MHD instabilities, such as the

effects of bootstrap current drive magnetic island. When the duration of sustaining high toroidal beta plasma is longer than the resistive diffusion time scale $\tau_R = \mu_0 r^2/\eta$ (η is specific resistivity of plasma at the radius r of rational surface), neoclassical tearing mode (NTM) appears in the magnetic island, when the poloidal beta exceeds critical values. The most simple form of the modified Rutherford equation describing the evolution of the island width is given by the following expression:

$$\frac{\tau_R}{r^2}\frac{dw}{dt} = \Delta' + \epsilon^{1/2}\beta_p \frac{L_q}{L_p}\frac{\beta_p}{w} \tag{1.19}$$

being Δ' the classical stability index defined as the logarithmic jump of the radial magnetic field perturbation across the rational surface, ϵ the aspect ratio and L_p (L_q) the pressure (the magnetic shear) gradient length. The first term of the right-hand side of 1.19 is the Rutherford term and the second is the destabilizing term of the bootstrap current.

At high β_p (poloidal beta) and low collisionality, the pressure gradient in the plasma gives rise to a bootstrap current. If an island develops, the pressure within the island tends to flatten out, thereby removing the drive for the bootstrap current. This give rise to a helical 'hole' in the bootstrap current, which increase the size of the island. The ECCD, due to the a tailored current deposition, will be used to stabilize the NTM mode restoring the bootstrap lack current in the island center (O-point). The most significant NTMs are those with $m/n = 3/2$ *or* $2/1$ for which a first study for their stabilization in a Demo reactor determined the requirements for the ECCD system in terms of the frequency range ($270 - 280\ GHz$ for different current profile [22]) and the amount of power ($2.5\ MW$ or $3.3\ MW$ for $q = 3/2$ or $q = 2$ respectively to reach the stabilizing condition $j_{ECCD}/j_{bs} > 1.2$ [23]).

In the last conceptual EU DEMO study the frequency of the EC system has been reduced to $204\ GHz$ and a list of the required power with the deposition location has been provided and reported in Fig.1.22 [24].

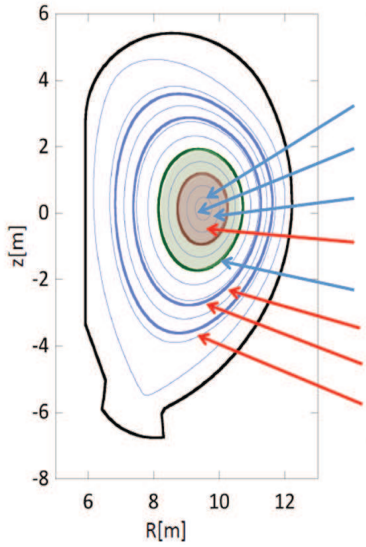

Task	Power [MW]	r/a	Mode
Breakdown and start-up	6-10	~central	H/CD
L-H transition in Ip ramp	50 – (80)	central	H/CD
Main Heating	Up to 50	central	H
Sawtooth control	tbd	< 0.3	CD
Ip Ramp down	40	>0.3	H
Disruption control (under study)	tbd	0.7	CD
NTM control (3,2)	>15	0.7	CD
NTM control (2,1)	>15	0.865	CD

Figure 1.22: Main EU DEMO EC tasks with corresponding power required and deposition location [24]

Chapter 2

EM source for additional plasma heating and instability dumping

A major objective to be pursued in the design of future fusion reactors is the decrease of re-circulated power, which draws a special attention to the wall-plug efficiency of heating and current drive systems. The conceptual study for a self-sustainable DEMO-nstration reactor foresees for the current drive systems an efficiency larger than 30% [14]. This represents a critical requirement to develop the future electron cyclotron systems for next generation fusion devices.

As discussed previously to heat up electrons that in turn raise the temperature of the hydrogen-based plasma in order to facilitate fusion for future power plants we can use millimeter waves carrying high power.

All microwave power electronics operate on the principle of converting the kinetic energy of an electron stream (electron current) to coherent electromagnetic radiation. In solid-state microwave electronics, the electron stream is sustained by applying a voltage between the emitter and collector electrodes (bipolar junction transistor or "BJT") or the source and drain electrodes (field effect transistor or "FET") at the two extreme ends of the device. This electron stream diffusively drifts through a solid medium (semiconductor). In contrast, in most vacuum microwave electronic devices, the electron stream is sustained by its inertia after its initial acceleration by a voltage applied between a cathode and anode placed in close proximity at one end of the device. In this way the vacuum amplifier designer can significantly increase the peak power in the e-beam by increasing the cathode-anode

voltage as well as the beam current. There are two intrinsic features of the typical vacuum device that provide this high-voltage design capability.

The first advantage, working with a vacuum, is due to the possibility of high voltages utilization without exceeding breakdown limits. Furthermore, the e-beam voltage electronics are completely separated from the interaction region. That gives the designer added flexibility to increase the cathode-anode dimensions at high voltage without changing the interaction circuit size. This is a crucial point, because the interaction circuit size is fundamentally constrained by the choice of operating frequency.

The second inherent advantage is that the vacuum amplifier can gate the high-power e-beam in a shortest rise time. In a solid-state power amplifier once the output frequency has been specified the emitter-collector/source-drain separation must be below a maximum length and in to prevent the dielectric breakdown to increase the output power we must increase the current combining multiple transistor increasing the rise times for turning on the emitter-collector current.

The vacuum tube with much more flexibility allows to generate high power at high frequency even if in this case we have some limitations due to the basic physics of the beam-wave interaction, ohmic heating in the cavity, heating in the collector of the spent electron beam. In case of continuous-wave(CW), which are required for heating of magnetic fusion plasmas, ohmic heating is a critical limiting factor and the corresponding scaling of the power with the frequency is:

$$P_{max} \propto 1/f^{5/2} \tag{2.1}$$

which has been observed over a broad range of devices. This is a simple result of the area of the device components scaling as λ^2 and the penetration depth of the microwave induced currents scaling as $\lambda^{1/2}$.

The electromagnetic wave at high power in a vacuum tube is generated interacting high energetic beam with the waveguide mode in a cold cavity. The emission mechanism is essentially governed by the Bremsstrahlung effect: the particles beam broken by the interacting wave will be bunched to emit coherently at a given resonance condition.

The only difference among the various tube lives in the particle bunching mechanisms, which will be deeply discussed in the next chapter, such as: Free Electron Laser (FEL), Gyrotron and Cyclotron Auto-Resonance Maser (CARM).

The most reliable and mature technologies for the electron cyclotron resonance heating (ECRH) and electron cyclotron current drive (ECCD) is provided by the Gyrotron system. In ITER installation the 24 of 170 GHz gyrotron systems with 1 MW microwave power each has been released with the collaboration of Japan, Russia and EU.

Studies for self-sustained DEMO operation claims for ECCD system an efficiency exceeding 30% for large continuous-wave power ($\approx$ 1 MW) at high frequency ($\approx$ 250 GHz)[14]. Nowadays, the scientific community is devoting a special effort to extend above 200 GHz the operational frequency range of the gyrotron, the most mature technology in the field of mm-wave tubes. A notable result has been recently achieved with the demonstration of a 300 GHz source with 0.5 MW output power and an efficiency of 20% [26].

The main problems with gyrotron appear when we need to increase the output power using a moderately relativistic beam as the resonance condition, at which the beam-particle energy exchange take place, will be affected by the relativistic factor with a considerable reduction of the system efficiency. Conversely, the lose resonance during the gyrotron interaction can be balanced considering a RF system tuned at the Doppler-shift interaction (CARM), as will be discussed later.

In this frame a research and development program has been undertaken at ENEA Frascati Research Center, aimed at realizing a microwave tube based on a Cyclotron Auto-Resonance Maser (CARM) oscillator [27], characterized by a high value of the frequency Doppler up-shift allowing a consistent reduction of the static magnetic field in the interaction cavity. The price to be paid is the necessity of exploiting high quality electron beams, with velocity spread below 0.5%, in order to ensure appropriate mode selection, adequate wave-beam power transfer with the required efficiency.

2.1 The Enea CARM design

A CARM source delivering *1 MW* at *250 GHz* with an efficiency of *30%* has been planned to be realize in the next years. In this section is given an overview of the main elements composing the device design, whose layout is reported in Fig. 2.1.

The relevant components are listed below:

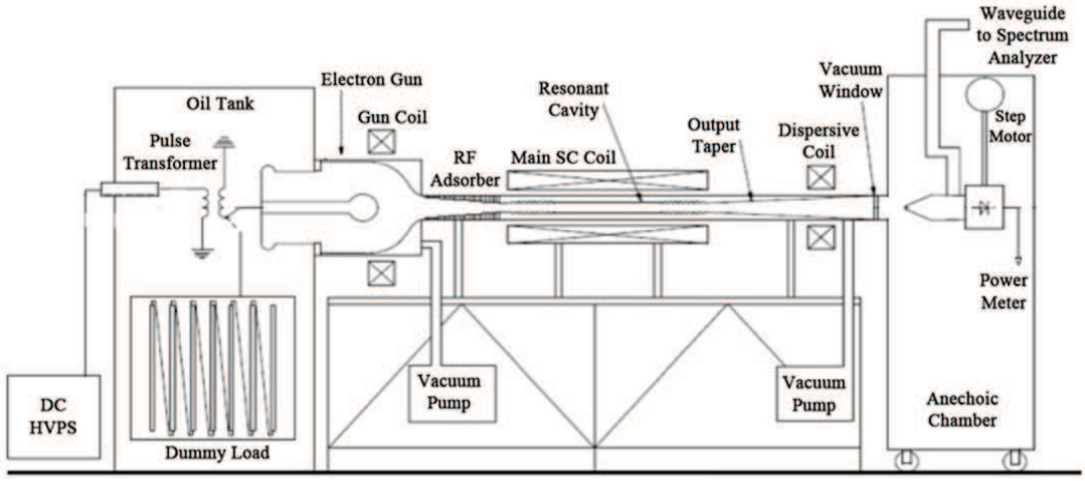

Figure 2.1: Layout of the CARM source including all the ancillary devices.

a) High Voltage Modulator

b) Electron Gun

c) RF Circuit

d) Magnetic Circuit

e) Beam Dump

f) Vacuum System

g) Supporting Structure

h) Diagnostic Tools

i) Cold Test Facility

j) Experimental Room

k) Control Room and Control System

a) ***High Voltage Modulator***

The High Voltage Modulator is one of the most crucial, complex and expensive part of the whole CARM system. The relevant complexity comes from the

noteworthy required stability of its electrical parameters, comparable to that of the modulators for High Power Klystrons.

The design and realization complexity has suggested the strategy of developing the ENEA CARM project in two steps.

The first step is mainly aimed at the realization of a CARM device to be tested in pulsed operation, with a maximum pulse length of *50* μs, at low repetition rate. With these tests the CARM electrical parameters will be optimized for maximizing the output power at the nominal output frequency.

The second step is instead aimed at developing a long pulse to CW CARM prototype equipped with a depressed collector for beam energy recovery, and a Vlasov-like output mode converter to conveniently extract the RF power.

Due to the power losses into the RF circuit, an intensive, forced water, cooling circuit will be necessary.

The main difference between the two steps is in the pulse length, even if rise and fall times and flat top accuracy of the pulses will be the same for both the steps. A different design approach has been provided for the HV modulator .

The single shot operation is an easiest way to test the single components and parts of the CARM and the CARM assembly as a whole. Apart of the Modulator all the other CARM components and units are or will be designed for CW operation. The pulsed modulator for the first step will cover the pulse length range from *1* to *50* μs with a voltage tunability of *0.1%* at the maximum output voltage of *700* kV. The other two important modulator parameters are the voltage ripple and the flat top smoothness, which should be in the range of *0.1%* too.

The modulator will be fully immersed in a metallic oil tank together with a dummy load and the cathode holder of the Electron Gun.

b) ***Electron Gun***

The electron beam is emitted and formed inside a diode type electron gun and then transported through a drift tube immersed in a direct high magnetic field. Most of the resulting helical beam properties are strongly dependent on the gun design. In general the electron beam is very sensitive to small changes of the emitter dimensions, emitter surface roughness and to its chemical properties. The road map followed during the preliminary design of the electron gun is the limitation of both the maximum surface electric field and the initial electrons velocity spread.

As a rule of thumb, for a gun designed for CW operation, the surface electric field at any point inside the gun region must be less than *10 kV/mm*.

The electron velocity spread is determined by the geometrical shape of the electrodes, their surface roughness, the emitter temperature and its uniformity over the whole emitter surface.

The space charge effect is proportional to the beam current density and is known as an emitter current load. In the preliminary design of the emitter the current density has been limited to *3* A/cm^2, a value that will assure it a long lifetime ($>$ *10.000* h). The emitter operational temperature was limited to *1300* $°C$ to minimize the electron beam initial thermal velocity spread and to increase the emitter resistance to poisoning. These values are lower than the present technological limits and will guarantee the highest possible beam quality.

c) ***RF Circuit***

The CARM RF circuit is the assembly of the RF cavity, the RF beam expander provided by the output tapered bringing the radiation to the vacuum window. Any component is designed for CW operation.

Within the RF resonant cavity of a CARM, usually oscillating in a TE_{mnp} mode, the electron beam energy is partially transferred to the high frequency electric field. The energy transfer efficiency depends on the electron beam quality, mainly determined by a high performance gun design. The efficiency level also depends on the

appropriate coupling between the electron beam and the cavity $TEmnp$ mode. The RF cavity must therefore guarantee an efficient beam interaction with the generated electromagnetic wave, characterized by a Doppler up shifted frequency, and the suppression of the down shifted (cutoff) counterpart. The mode selection is therefore of crucial importance for the CARM efficiency.

An oversized cylindrical cavity, which dimensions are set by the acceptable RF power dissipation limits on the cavity wall and by the electric breakdown in vacuum, will be used. In general it is extremely difficult to design a stable high Q cavity operating far from the cutoff. In addition the electron beam geometry along the CARM longitudinal axis has to be accurately studied because any interaction with the cavity walls, mainly during CW operations, must be absolutely avoided.

In this frame, the use of a quasi-optical resonant cavity, even though a fairly natural solution from the conceptual point of view in this frequency range, has been "a priori" discarded because of the thermal loads induced by the RF on the reflecting mirrors and also because of the difficulties with the electron beam transport.

The solution adopted for the ENEA CARM is a cylindrical smooth cavity delimited by Bragg reflectors, which, although complicated from the mechanical point of view, provides a distributed feedback and does not exhibit crucial drawbacks on the cavity cooling and on the electron beam transport.

The resonant cavity is connected to the larger CARM circular output waveguide through an accurately designed taper able to avoid any accidental mode conversion. The electron beam waste energy is dissipated on the CARM collector while the microwave radiation is launched into an anechoic chamber through a short circular transmission line. A CVD circular vacuum window, axially brazed on the collector wall, separates the evacuated CARM device from the transmission line. The optimum vacuum level is assured by a suitable pumping system assisted by an accurate mechanical design of the CARM RF inner components.

The CARM prototype object of the second design step, will be completed with an output mode converter, transforming the TE_{mn} operational mode into a gaussian

RF beam, and with a depressed collector in order to increase the overall efficiency of the device.

d) ***Magnetic Transport System***

The magnetic channel provides the correct electron beam formation before the injection into the cavity. It consists of a gun coil, a large cavity coil and a kicker coil. On the occurrence an additional correcting coil, positioned before the cavity coil, will be used to properly shape the desired magnetic field topology along the CARM longitudinal axis. All the components of the CARM assembly must be aligned very accurately along the CARM horizontal axis in order to realize an efficient beam transport and an optimal beam–RF coupling into the resonant cavity.

The gun coil encircles the gun region of the CARM and provides the necessary magnetic field for an appropriate electron beam emission and transport inside the diode.

The design of this coil has been done with the help of the CST Microwave Studio® (tracking module) to obtain the proper magnetic field intensity, which, in synergy with the static electric field inside the diode, allows the most appropriate electron beam kinematic conditions at the input of the RF cavity for the optimum CARM operations.

The relatively weak magnetic field in the gun region can be obtained by a short, water-cooled, coil. Its diameter must be larger than the grounded gun electrode. Its large cross section, short length and significant weight require a sophisticate supporting structure and an accurate alignment procedure.

The cavity magnetic field, due to its relatively high intensity, will be provided by a superconducting magnetic coil.

Both length and field intensity profile of the cavity coil have been evaluated by following the induced electron motion trajectory tracking along the system.

The design of additional coils for an accurate field profile correction is however foreseen to optimize the beam-wave interaction.

d.2) ***Kicker Coil***

The magnetic system includes also a kicker coil that generates a field with a nominal value in the range *0.08 - 0.1 T*, perpendicular to the longitudinal CARM axis. This coil is aimed at removing any stray electrons by forcing them into the grounded wall .

e) ***Beam Dump***

Once left the resonant cavity region, the exhaust electron beam is uniformly spread on the collector walls, where its waste energy is finally dissipated.

The impact of the high-energy electron beams (*700 keV*) of the ENEA CARM on the metallic collector walls generates hence a significant amount of X-ray radiation by bremsstrahlung. Thus the beam dump has to be carefully designed for absorbing the X-ray flux. Usually a multi-layered lead screen encloses this part to protect the surrounding area from the stray X-ray radiation. The beam impact also heats the CARM collector due to both scattering and ohmic losses. Therefore, the beam dump is cooled through suitable water pipes brazed on the outer part of its wall.

f) ***Vacuum System***

An efficient vacuum system is of capital importance for the correct operation of any high-power microwave tube. This system is designed to maintain inside the CARM an extremely low pressure at high pumping rate. In general a bad vacuum level is responsible for two extremely dangerous phenomena. The first one is a vacuum breakdown due to a high electric field across the electrode gaps. The second one is a surface breakdown due to a high surface electric field. There are rules regulating the limiting values for both cases that must be strictly respected during the design.

The CARM region under vacuum is about two meters long with a minimum cross-section radius of *15 mm*. The very first CARM prototype will operate at pulse lengths up to *50 μs*. Thus to maintain a pulse repetition rate of *10 Hz*, a double side pumping is required. Most of the components in the evacuated region cannot be slotted or drilled for a better pumping performance. Thus these components need to be carefully designed from the mechanical point of view in order to assure a suitable vacuum level around them.

A low vacuum level is also important for the emitter just to avoid a poisoning possibility. A special chemical treatment of the components assembled in the vacuum region before the final assembling has been therefore considered.

g − h) ***Supporting Stucture and Diagnostics***

An anechoic chamber is the most important diagnostic tool for characterizing a CARM device. It is a large metallic box, whose inner walls are lined with microwave absorbing material, pyramidally shaped for reducing the RF reflections. This chamber in practice simulates the free space propagation. The microwave pattern generated by the CARM output waveguide inside the anechoic chamber is sampled with a horn pickup, an open-ended rectangular waveguide with a cut off frequency of about *170 GHz*, externally dressed by RF absorbing epoxy foam. The microwave signal picked up by the horn is split by two. One half of this signal is directly sent to a power meter, the second half is instead sent to a frequency spectrum analyzer in order to have a complete characterization of the RF power launched in the vacuum chamber. The horn is supported by a dielectric rod and moved inside the anechoic room by a remotely controlled motor. The total emitted RF power can be measured by mapping the radial pattern of the microwave radiation and then by integrating it over the whole chamber volume.

i) ***Cold Test Facility***

The Cold Test facility is an important section of any microwave laboratory aimed either at the development of new devices or at the characterization of the existing

ones. The optimum performances of any microwave devices in facts depend on the accuracy of the cold tests.

The frequency of the ENEA CARM is part of a not completely explored sector of the frequency spectrum, so that many microwave components, also necessary for completing the cold test facility, must be expressly designed and developed at home. In particular a complex mode converter for feeding the CARM cylindrical resonant cavity in the TE_{53} mode, starting from the TE_{10} mode generated by a network analyzer in rectangular waveguide, is presently investigated.

A preliminary list of an essential outfit for our cold test facility is given in the following:

1. Network analyzer with output frequency up to *300 GHz*,
2. Mode converters from the TE_{10} mode in rectangular waveguide (*WR 3* or *WR 4*) to the cavity mode (i.e. the TE_{53}) in circular waveguide.
3. Circular tapers to connect the previous mode converter to the oversized circular waveguide of the resonant cavity.
4. Splitters, bends, attenuators, phase shifters, directional couplers and so on.

2.2 Gun Design and e-Beam Qualities

According to the discussion reported in the previously section, the generation of an electron beam with appropriate qualities is the prerequisite to achieve the desired CARM performances.

A thermionic gun has been designed and proven to be a suitable tool for the production of the electron beam with the foreseen velocity and angular spread. In Table 2.1 we have summarized the design parameters of the gun-beam system.

The considered gun is essentially a diode, which, unlike the triode gun used for gyrotron, is a non-adiabatic device. The relevant constituents: the cathode and the

Table 2.1: **Gun properties**

Cathode Voltage	$500 \div 700\ kV$
Relativistic Factor γ	$2 \div 2.4$
Beam Current	$1 \div 10\ A$
Pitch ratio $(v_\perp / v_\parallel)$	γ^{-1}
Axial and transverse velocity spread	$< 0.5\ \%$
Electric field at the cathode surface	$< 10\ kV/mm$

anode, are shown in Fig. 2.2.

The gun parameters of Table 2.1 have been figured out on the basis of a simple argument, which takes the heating power as pivoting reference. RF and electron beam power are linked by

$$P_{e-b} = \frac{P}{\hat{\eta}} \tag{2.2}$$

Furthermore, since P_{e-b} is given by the product of the current time the accelerating voltage

$$P_{e-b} = IV \tag{2.3}$$

we obtain

$$I = \frac{P}{\hat{\eta}\, V} \tag{2.4}$$

If we require a total electron efficiency around *30%* and demand for a CARM rf power of about *1 MW* we find for the corresponding e-beam power $P_{e-b} \cong 3\,MW$, which can be achieved by imposing suitable constraints on the accelerating voltage and beam current.

The efficiency of *30%* can be obtained if the beam energy spread is suitably small, therefore the most convenient design solution is that of as high as possible accelerating voltage to increase the e-beam kinetic energy and a low current to avoid additional velocity spread, induced by the space charge effects. By choosing e.g. an

accelerating voltage of *600 kV*, the resulting beam current is about *4.5 A*.

A non-secondary issue in the design of the gun is the necessity of producing an electron beam with a ring shape to be positioned on a selected radial RF-field maximum of the desired cavity mode, allowing the optimum coupling conditions. Usually, those devices use the whispering gallery modes for operation which determines the beam profile (see Fig. 2.2). The electrons emitted from the ring are pushed ahead by the strong electrostatic field given by the accelerating tension and are guided by a longitudinal magnetostatic field generated by a gun coil.

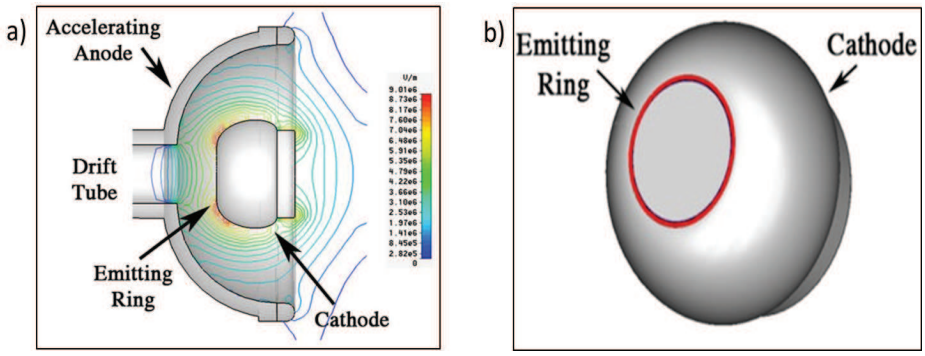

Figure 2.2: a) Diode-like gun, b) Emitter ring

Having specified the value of the accelerating voltage we can provide a first idea of the relevant geometrical dimensions by starting from the following relation between the cathode and anode radii $R_{cath,an}$ in the case of a spherical shape

$$R_{cath} = \frac{R_{an}}{2}\left(1 - \sqrt{1 - 4\,\frac{V}{E_{surf}R_{an}}}\right) \tag{2.5}$$

which implies an equilibrium condition between the accelerating field V and the electric field E_{surf} at the cathode surface . The condition to be fulfilled to ensure the positivity of the of the argument of the square root in the previous equation is

$$R_{an} \leq 4\,\frac{V}{E_{surf}} \tag{2.6}$$

the use of the threshold value of $E_{surf} \cong 10^7\,\frac{V}{m}$, ensuring no cold field emission effects, implies $R_{an} \cong 30\ cm$.

The electron beam generation and transport can be roughly divided in three parts:

a) The electrons are emitted from a circular corona at the cathode emitting surface, which is kept flat to ensure an homogeneous longitudinal velocity. At the exit of the corona the electrons are captured by the gun accelerating (longitudinal) field and guided by a superimposed static magnetic field, focusing the beam by compensating the transverse components of the velocity, induced by a transverse electric field having a cusp at the transition edge of the diode and drift tube (see Fig. 2.3).

b) Near the drift tube the electrons receive a transversal kick induced by the transverse electric field acting as a beam defocusing lens.

c) Inside the drift tube the electron beam undergoes the combined effect of the fringing fields of the gun coil and the cavity coils (Fig. 2.3 and Figs. 2.4) .

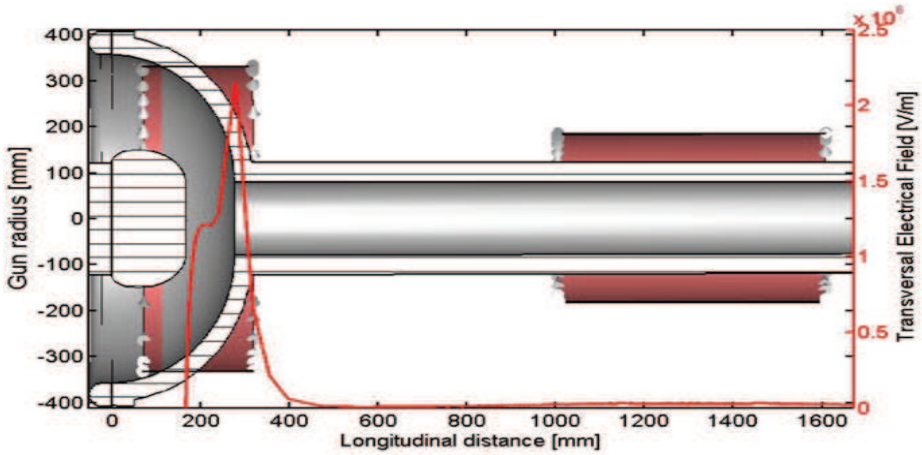

Figure 2.3: Gun geometry with the transverse electric field induced by the anode edge whose values are reported on right side of the $y - axes$.

The longitudinal and transverse velocities (in m/s) along the gun (axis) in mm is shown in Figs. 2.4a, 2.4b respectively.

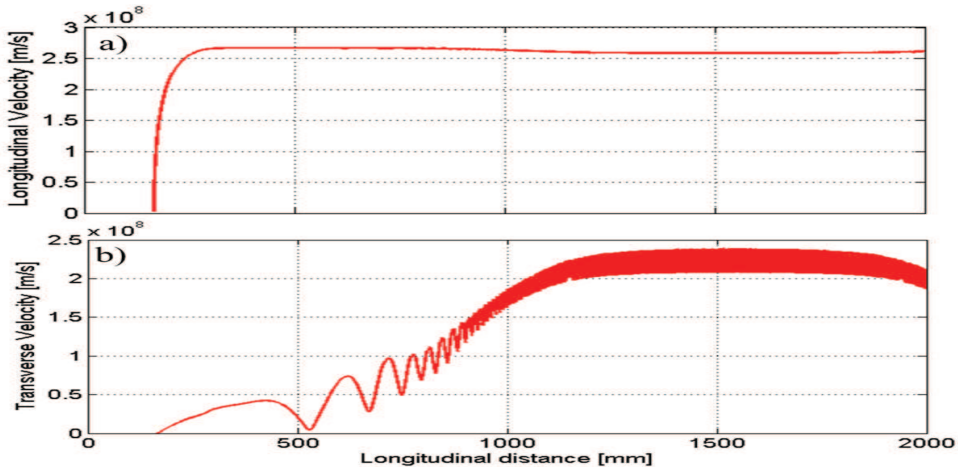

Figure 2.4: Longitudinal a) and transverse b) velocity vs. longitudinal direction of the gun axial symmetry.

The longitudinal and transverse relative velocity spread are reported in Figs. 2.5a and 2.5b respectively, while the pitch ratio is shown in Fig. 2.6. The results provided by the simulation are compatible with the homogeneity requests quoted in the previous sections.

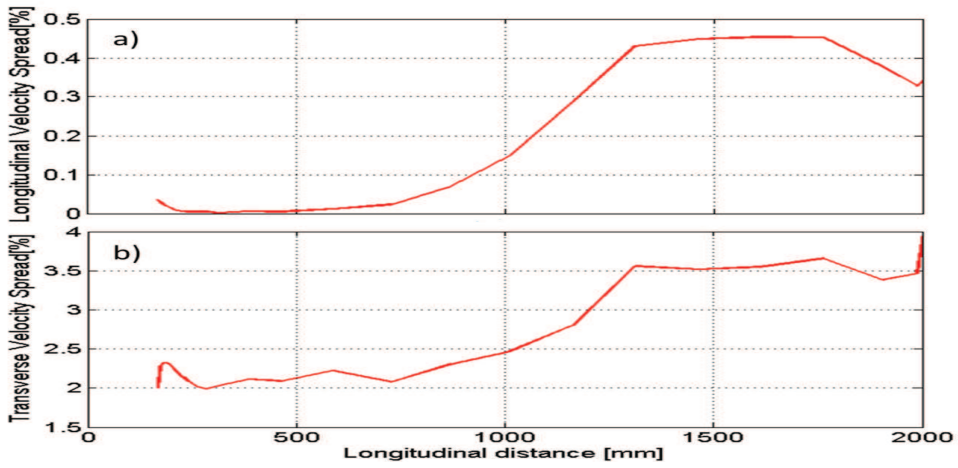

Figure 2.5: Longitudinal a) and transverse b) particles velocity spread vs. longitudinal direction of the gun axial symmetry.

The proposed gun design is based on a non-adiabatic electric field solution, with a transverse component in correspondence of the ending edge of the diode (see Fig.

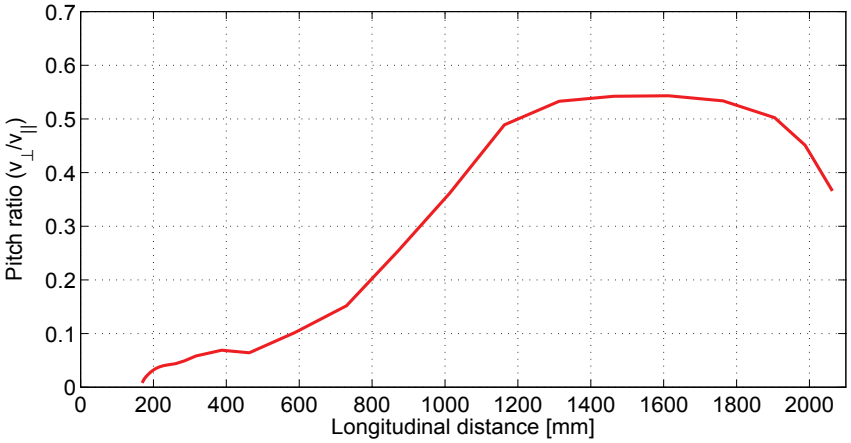

Figure 2.6: Pitch ratio vs. longitudinal direction of the gun axial symmetry.

2.3). The magnitude of the effect can be easily understood, the use the standard formulae for the Pierce gun design, we write the electric field at anode

$$E_A \cong \frac{V}{|R_{cath} - R_{an}|} \frac{R_{cath}}{R_{an}} \tag{2.7}$$

thus getting, for our design parameters an anode field value on the order of $10^6 \frac{V}{m}$, which agrees with the results provided by the simulation.

Owing to the cusp the effect of the field on the electrons can be viewed as a defocusing with a focal length specified by

$$f = -4\frac{V}{E} \cong -4\frac{\rho_c}{\rho_a}(\rho_c - \rho_a) \tag{2.8}$$

An idea of the relevant effect on the particle dynamics is given in Fig. 2.7, where the effect of the field edge on the transverse velocity is emphasized.

As already stressed, the electrons are produced in a ring shaped form to fulfill the optimum overlapping with the chosen operating mode inside the CARM cavity. In the technical annexes we will report the details of mode selection and the beam transport conditions ensuring the safe transport of the annular beam, along the line from the cathode to the interaction region.

In Figs. 2.8 we have reported the beam transverse section at different positions inside the channel from the cathode to the CARM cavity; the electrons are

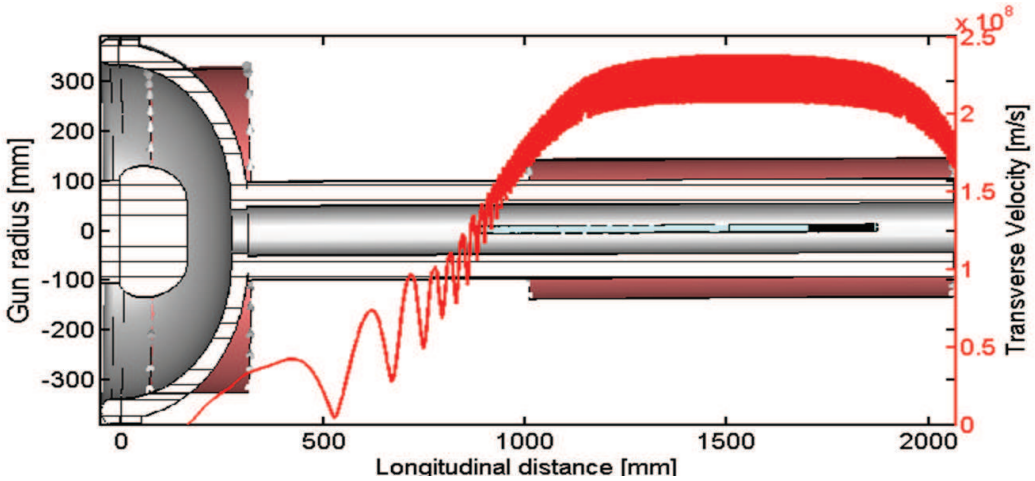

Figure 2.7: Transverse velocity from the cathode to the drift tube

distributed along a circular corona ring and crucial parameters are

1. The average beam radius vs. z (see Fig. 2.9).

2. The beam corona section vs. z (see Fig. 2.10).

The beam is captured on a ring orbit with smaller radius inside the cavity, owing to the large strength of the CARM magnetic field. The radius stability is related to stability the magnetic field produced by the set of the solenoids. The width of the corona undergoes a kind of strong focusing effect yielding a minimum at the center of the cavity and is then defocused. The importance of the beam radius control comes from the coupling conditions with the CARM operating modes.

The preliminary considerations, developed in this section, show that the e-beam can be transported preserving its shape, which can be controlled to ensure the desired electron beam electromagnetic mode coupling in the resonant cavity. The specific design details are reported in the next section.

The beam shaping accuracy, with particular reference to its annular structure, is very important because strictly associated to the interaction between electrons and electric field modes in the resonant cavity, that critically depends on the beam shape and thickness along the cavity itself. It is evident that the mode excitation

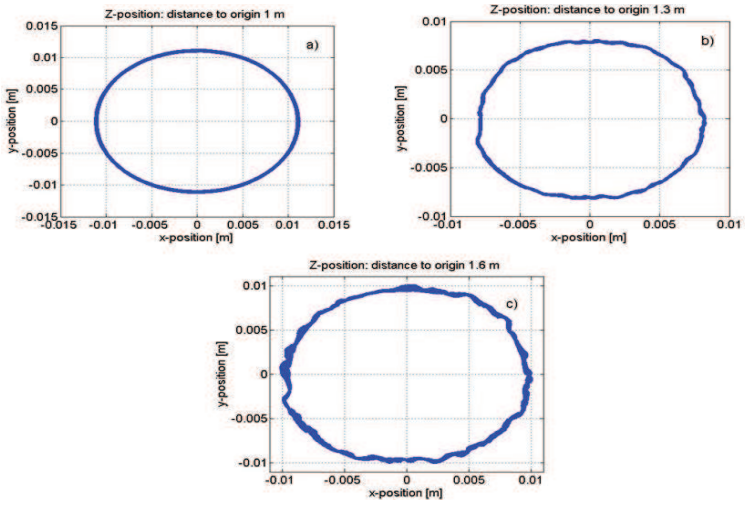

Figure 2.8: The electron beam ring at different positions along the transport line: a) at the cavity entrance, b) at the cavity middle, c) at the cavity output.

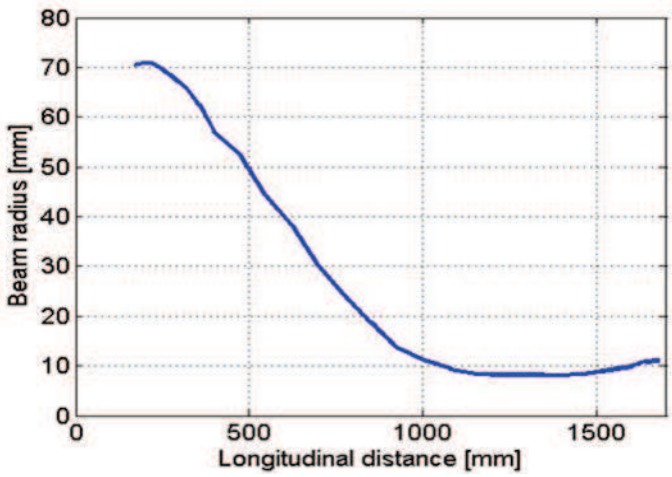

Figure 2.9: Average radius of the electron beam vs. longitudinal coordinate $z[mm]$.

crucially depends on the portion of beam overlapping the structure of the transverse eigenmodes. This mechanism is crucial for determining the number of excited modes, which can simultaneously grow and eventually induce a reduction of the CARM efficiency. The matching between electron beam and electric field in the resonant cavity will be therefore one of the pivotal topics of the next section.

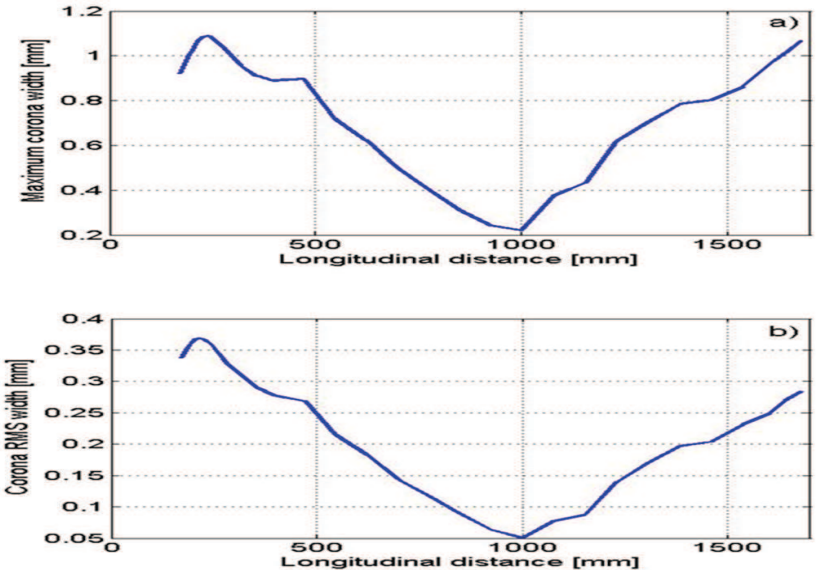

Figure 2.10: Average corona thickness vs z.

2.3 The e-Beam Transport Line Modeling

In Fig. 2.11 a detailed field profile with the expected intensity values has been reported a superimposed to the core part of the device from the cathode to the region in which the interaction between the electron beam and the high intensity magnetic field determines the CARM coherent emission.

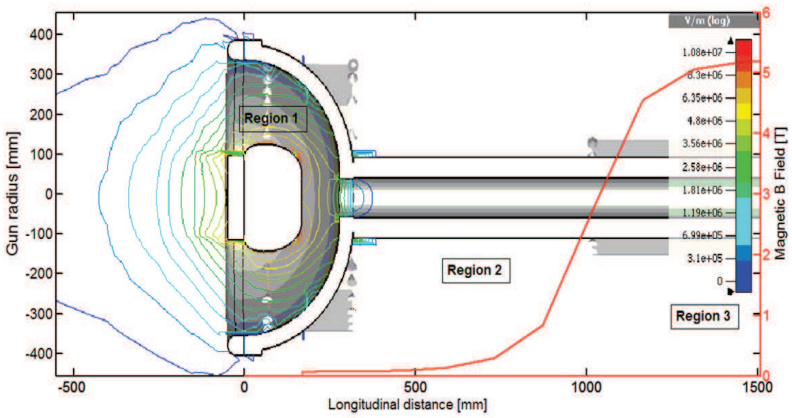

Figure 2.11: Magnetic field intensity profile from the cathode to the interaction region with the three operating region: 1) Acceleration and beam forming region, 2) Adiabatic tapering, 3) High field interaction region.

As already stressed previously, the transport line from the cathode to the cavity region, is of paramount importance to obtain an e-beam with suitable characteristics for the CARM operation. The relevant design strategy can be summarized as it follows (see Fig. 2.11):

a) The first part segment (namely the transition from region 1) to 2) has the role of bringing the electrons to a kinetic energy of $0.6\ MeV$, furthermore it is supposed to induce a kick due to the electric field of the edge cusp (see below) leading to a transverse component velocity, yielding an appropriate pitch angle of the e-beam providing a suitably large coupling with the cavity modes.

b) The "drift" section before the region 3), where the combined magnetic field of the principal and correcting coil is present, has a manifold role.

c) To Control the transverse motion components, by adjusting the pitch to an optimum value.

d) To control the radius of the anular beam and eventually the thickness of the corona

e) To match the section of the beam to the cavity mode to be enhanced by the CARM interaction. The matching should be achieved in an adiabatic way by eliminating (through a gentle tapering of the e-beam ring radius) the coupling to unwanted mode in the region of the cavity containing the Bragg reflector (see Fig. 2.11 where we have superimposed the field intensity tapering to the cavity region).

In Fig. 2.12 we have reported the pitch ratio evolution along the longitudinal coordinate and we have underscored the region where the kick occurs and the successive concurring effect of the magnetic field, which, among the other things, counteracts the growth of the transverse motion.

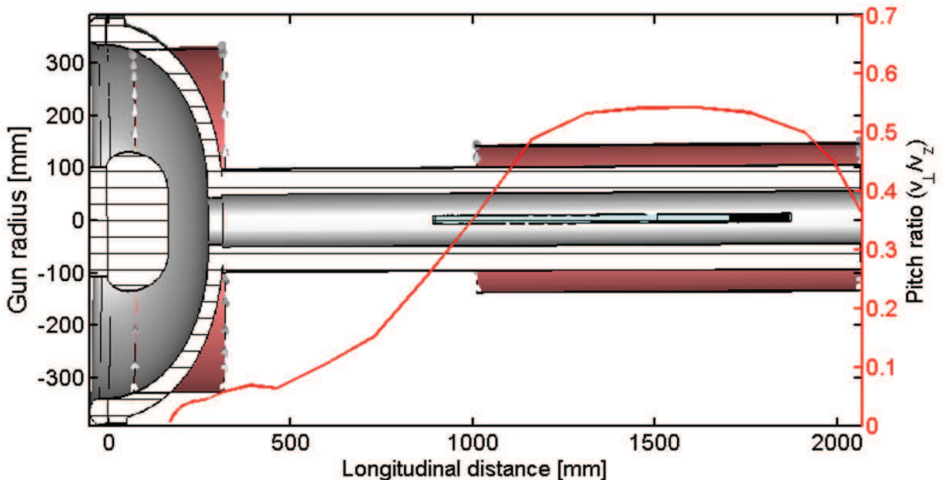

Figure 2.12: Pitch evolution $\left(\frac{v_\perp}{v_z}\right)$ vs. the longitudinal direction.

In Fig. 2.13 has been reported the evolution along the transport line of the spread of the longitudinal velocity, which grows with increasing transverse velocity component, but remains, in the interaction region well within the limits for a safe CARM operation.

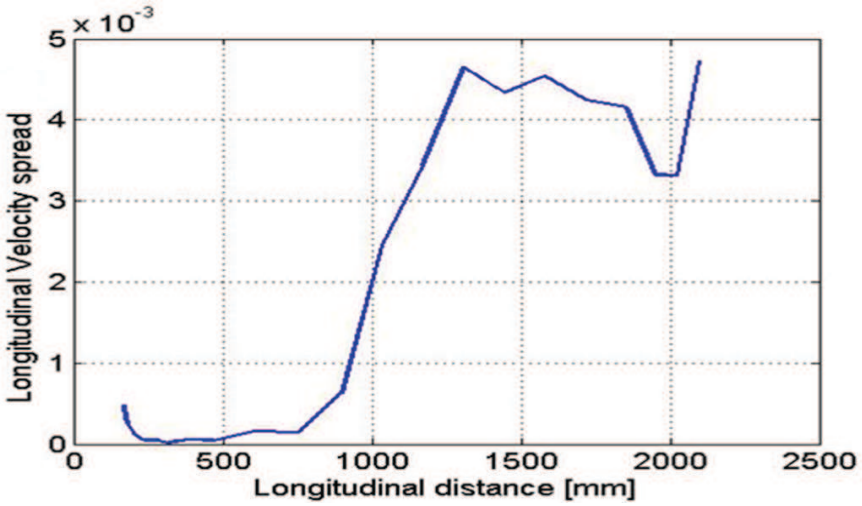

Figure 2.13: Relative longitudinal velocity spread $\left\langle \frac{\Delta v_z}{v_z} \right\rangle_{rms}$ along the transport line (coordinate z).

In Fig. 2.14 it is shown the beam radius vs. the transport coordinate and it is evident that in the interaction region the beam has the suitable dimensions to couple to the cavity modes.

A more appropriate idea is offered by Fig. 2.15, yielding the transverse profile of the beam at different position along the transport line. It is evident that the control of either radius and the thickness of the circular corona may become problematic.

The study we have developed so far is not based on a very refined theory to optimize the transport detail. We have indeed merely used a ray-tracing procedure to study the particle distribution and not an elaborated technique, as in the case of strong focusing, based on a formalism a lá Courant and Snyder. Within such a context concepts like emittance and Twiss parameters could provide a substantive help too. We must however emphasize that we are dealing with the transport of an e-beam with unusual characteristics. In standard acceleration and transport problems the beam is solid (without any hole) so that the concept of quantities like emittance and phase space domain are easily defined. To overcome such a drawback, we have developed a different point of view, namely we have visualized the beam as a collection of beamlet around the corona as illustrated in Fig. 2.16. The use of

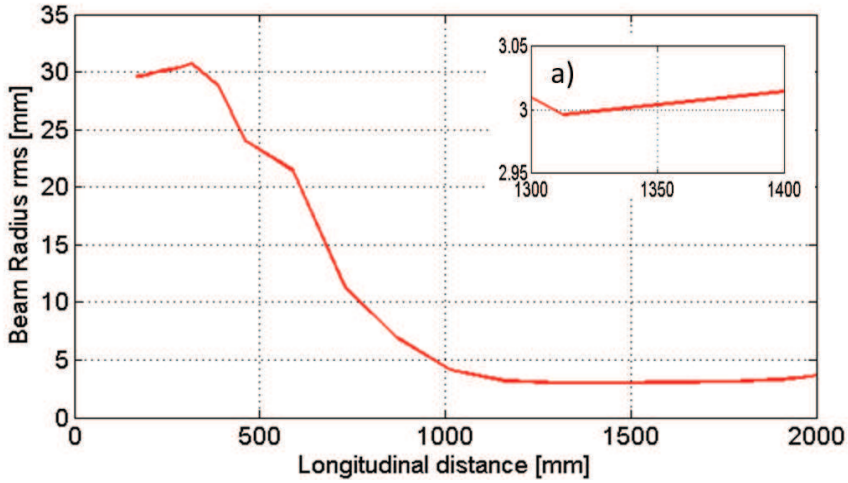

Figure 2.14: Annular beam radius vs. the longitudinal coordinate optimized for the interaction with the waveguide mode TE_{53}. In the square a) has been evidenced the beam radius value at the entrance of the smooth cylindrical section of the cavity where the coupling coefficient assumes the maximum value as will be discussed in the last chapter (see Fig. 4.6)

such a point of view is helpful to check the reliability of the previous analysis and reconcile our procedure with a more conventional point of view.

According to the usual procedure we define the r.m.s. of the x and y position and of the relevant velocity components, defined as

$$\begin{aligned} \xi^{'} &= \frac{d\xi}{dz}, \\ \xi &= x, y \end{aligned} \tag{2.9}$$

We then introduce the 2×2 covariance matrices

$$
\begin{aligned}
&\hat{C}_{x,x'},\, \hat{C}_{y,y'},\, \hat{C}_{x,y},\\
&\hat{C}_{\xi-\xi'} = \begin{pmatrix} \sigma_{\xi\xi} & \sigma_{\xi\xi'} \\ \sigma_{\xi'\xi} & \sigma_{\xi'\xi'} \end{pmatrix},\ \hat{C}_{x,y} = \begin{pmatrix} \sigma_{xx} & \sigma_{xy} \\ \sigma_{yx} & \sigma_{yy} \end{pmatrix},\\
&\sigma_{\xi\xi} = \sqrt{\langle \xi^2 \rangle - \langle \xi \rangle^2},\\
&\sigma_{\xi'\xi'} = \sqrt{\langle \xi'^2 \rangle - \langle \xi' \rangle^2},\\
&\sigma_{\xi\xi'} = \sqrt{\langle \xi'\xi \rangle - \langle \xi' \rangle \langle \xi \rangle}.
\end{aligned}
\tag{2.10}
$$

To give an idea of how these quantities evolve, we have reported in Figs. 2.17 the evolution along the longitudinal direction of the square root of the associated determinants. In Fig. 2.17a we have reported the behavior of $\sqrt{\left|\hat{C}_{x,y}\right|}$ which represents the *rms* area of the annular beam. The evolution of $\sqrt{\left|\hat{C}_{x,x'}\right|}$, $\sqrt{\left|\hat{C}_{y,y'}\right|}$ is shown in the plots of Fig. 2.17b. These quantities could be interpreted as the the longitudinal and vertical emittances [1]. A general conclusion which can be drawn from the previous plots is that the condition of minimizing either $\left|\hat{C}_{x,y}\right|$ and $\left|\hat{C}_{x,x'}\right|$, $\left|\hat{C}_{y,y'}\right|$ in the interaction region cannot be achieved, the "matching" condition consists in a gentle comporomise, to be achieved by relaxing the request on the surface minima.

A general comment and a caveat should be added; in designing the transport line of the CARM device we have been faced with a number of design problems, hereafter specified

a) The absence of an appropriate theoretical framework to handle this type of beam transport as in the usual Courant Snyder (*C-S*) theory, allowing the definition of quad-like lenses to drive the beam.

[1] There are technical issues regarding the definition of emittance suggested in this text. The quantity we have mentioned does not, strictly speaking, represent an emittance, it refers to the particle beam phase space area and is a conserved quantity during the transport. Its rigorous definition requires the use of canonical variables to properly treat the phase space and the relevant transport. Regarding our case we have used the transverse velocities, which, for the type of fields and forces involved in, are kinetic and not canonical variables. Furthermore, the quantities we have reported are not a transport invariant for different reasons, including the fact that we are not dealing with a Liouvillian transport along the entire line and that, inside the main solenoid, the *x-y* motion is coupled and therefore the real invariant is associated with the *6-D* phase space.

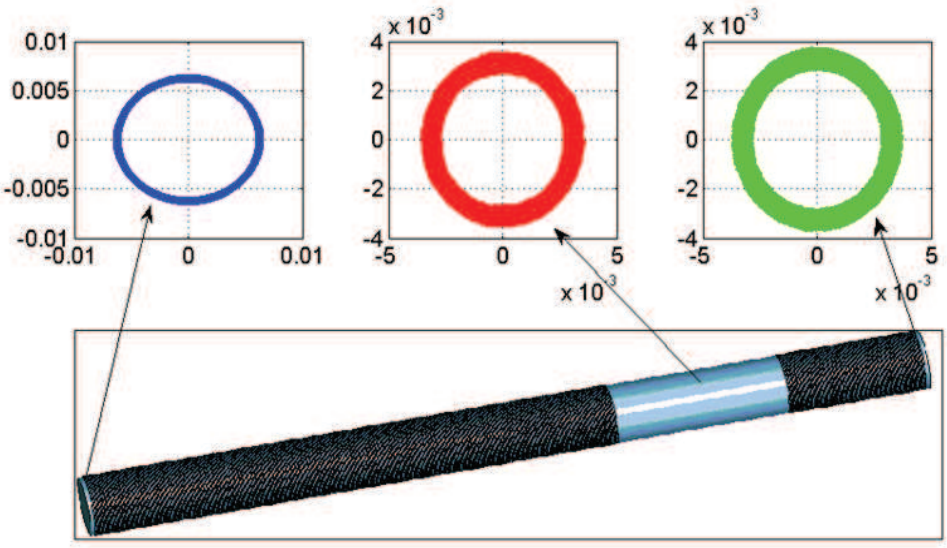

Figure 2.15: Geometrical distribution of the beam at different position along the longitudinal axis, *a*) $z = 900\ mm$, *b*) $z = 1613\ mm$, *c*) $1873\ mm$.

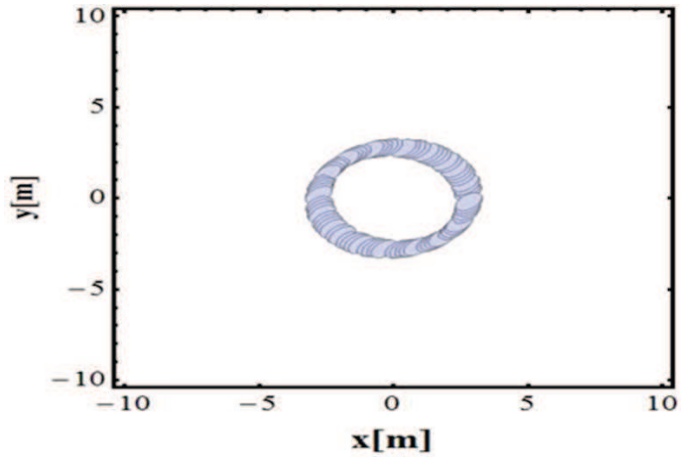

Figure 2.16: Beamlet realization of the beam circular corona.

b) The difficulties associated with the control of either annular beam radius an corona thickness.

c) The extreme sensitivity of these quantities to the magnet field distribution inside and outside the cavity interaction region.

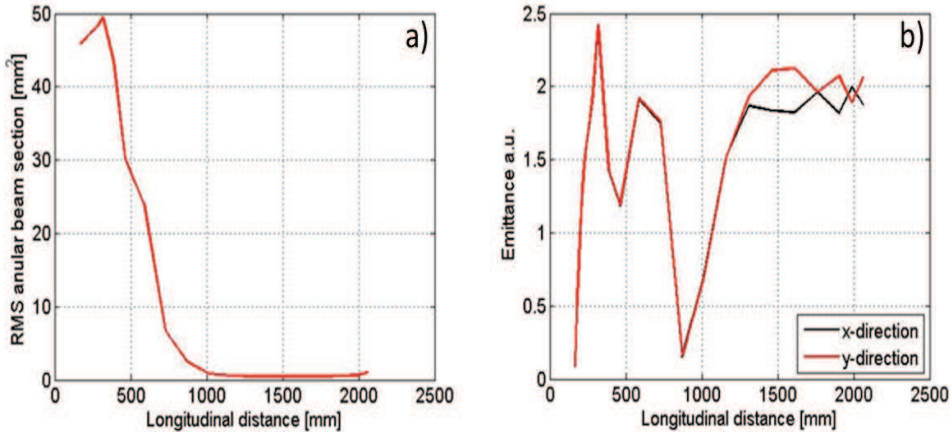

Figure 2.17: a) Annular beam r.m.s. area $\left(\sqrt{\left|\hat{C}_{x,y}\right|}\right)$ vs longitudinal coordinate; b) emittance (arbitrary units) $\left(\sqrt{\left|\hat{C}_{x,x'}\right|}, \sqrt{\left|\hat{C}_{y,y'}\right|}\right)$ vs. thelongitudinal coordinate (in current units the a.u. units should be multiplied by $10 \cdot mm \cdot mrad$).

d) The importance of the emitting cathode surface roughness, only partially accounted for.

The results we have obtained show that

i) A *C-S* like theory can be partially recovered and some of the relevant paradigmas can be exploited within the present context.

ii) The annular beam geometry and shaping can in principle be controlled, but an analysis of the relevant criticity has not been done.

iii) A global matching of the beam (including the adequate condition on velocity spread) can be obtained, but optimization criteria has not been found yet.

Chapter 3

Beam-wave interaction from FEL to CARM

In this chapter Free Electron Laser (FEL), Cyclotron Auto-Resonance Maser and Gyrotron devices will be described by putting in evidence the common physical mechanisms underlying the operation of different types of free electron coherent generators. The strategy we will follow is that of identifying a set of key parameters to characterize these devices (gain, saturation intensity...) and model the relevant dynamics in terms of these macroscopic quantities. We will provide a fairly complete analogy with undulator magnet FEL, to take advantage of the scaling "law" developed in the past for the relevant design. We will proceed by an accurate modeling of the beam wave interaction in CARM/Gyrotron devices. We deduce the equations ruling the evolution of the system and state the analogy with that ruling the dynamics of U-FEL. We show, by numerical benchmarking with a homemade 1-D code, the compatibility of the analysis with the U-FEL semi-analytical formulae.

3.1 FEL, Gyrotron, CARM interaction: a common point view

The FEL, Gyrotron and CARM utilize free electrons in a vacuum to convert energy from a DC power source to an RF signal. The basic processes governing the electromagnetic (EM) radiation is the Bremsstrahlung effect when charged particles move with a variable velocity. In particular the magnetic bremsstrahlung occurs

when electrons move along curvilinear trajectories in an external magnetic field. Such radiation is produced when electrons, that are initially uncorrelated and producing spontaneous radiation with random phase, are gathered into microbunches which subsequently radiate in phase. This field can be either constant (in case of CARM/Gyrotron) or periodic (in case of FEL). A constant magnetic field can be produced by a permanent magnet or solenoid, while a periodic field can be produced by a periodic array of magnet elements.

CARM/Gyrotron are sources of coherent magnetic bremsstrahlung based on electron oscillations in a constant external applied magnetic field. This kind of devices belong to a wider family, the cyclotron resonance masers(CRMs).

The layout of a generic CRM in Fig. 3.1 shows electrons move along the waveguide axis performing oscillations in a constant magnetic field H_0 and interacting with an EM wave propagating in the $\overrightarrow{k}$ direction. Among CRMs, the most advanced are gyro devices, which utilize magnetron-type electron guns (for gyrotron) or a diode gun (for CARM see the previous chapter) which produce annular electron beams in which electrons execute small cyclotron orbits at frequency $\Omega_{CARM} = eB/m$, being B the external magnetic field and $e,\ m$ charge and mass of the electron respectively.

The resonance condition of the beam-wave interaction appears when the Doppler-shifted wave frequency is close to the frequency of electron oscillations or one of its harmonics[28, 29]:

$$\omega = s\frac{\Omega}{\gamma} + k_z v_z \tag{3.1}$$

where s is the harmonic number, v_z the electron axial velocity and k_z the axial component of the wave vector. This resonance condition can be fulfilled for any wave phase velocity ($v_{ph} = \omega/k_z$). The radiated waves can be either fast ($v_{ph} > c$) or slow ($v_{ph} < c$) wave. Operation with fast waves (like Gyrotron/CARM) has certain advantages, especially at short wavelengths, because fast waves can propagate even in free space. Therefore, these waves are not localized near the walls of the microwave circuit and there is no need to utilize slaw wave structures with elements smaller than a wavelength. Correspondingly, the interaction space can be extended in the transverse direction, which allows one to substantially increase the radiated power levels.

Fast and slow wave devices are characterized by different bunching mechanisms[30].

In the case of fast wave it is caused by the $v_\perp \cdot E_\perp$ product, where $v_\perp$ is the electron transverse velocity, $E_\perp$ is the wave transverse electric component. The electric force effect changes the relativistic electrons mass modulating the particles cyclotron rotation through the Eq. 3.1 inducing a bunching. In the slow-wave devices the basic mechanism of radiation is the Weibel instability, in which the dominant effect is axial bunching caused by the axial $v_\perp \times B_\perp$ Lorentz force, where $B_\perp$ is the transverse magnetic component. The Lorentz force modulating the particle axial velocity will induce a bunch acting on the last term in the Eq. 3.1 [31, 32, 33, 34, 35].

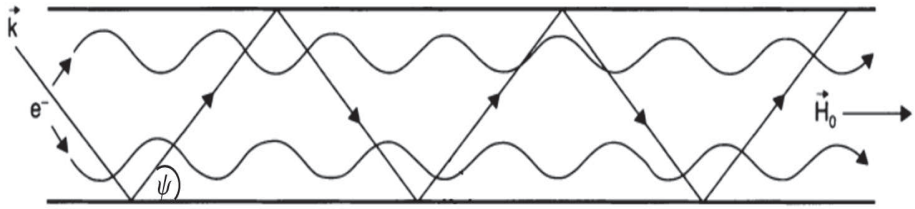

Figure 3.1: The CRM interaction scheme where an annular electron beam e^- interacts with a waveguide mode of a cylindrical cavity surrounded by an axial magnetic field H_0; being ψ the Brillouin angle of the eigenwave.

The free-electron lasers (FELs) are the most common devices based on radiation from electrons oscillating in periodic external fields. In Fig. 3.2 is illustrated the typical configuration employed in the FEL interaction.

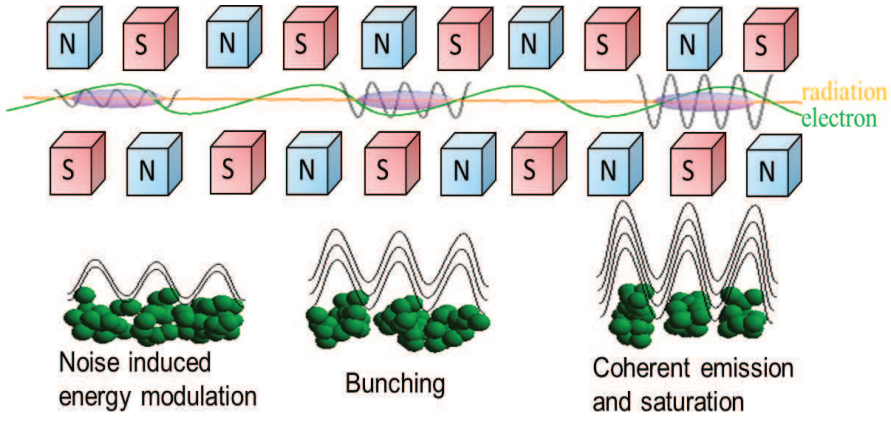

Figure 3.2: The FEL lasing process: energy modulation, bunching and coherent emission.

While in CRMs the electron oscillation frequency is just the electron cyclotron

frequency, in FELs the electron oscillation frequency is $\Omega_{FEL} = k_u v_z$, where $k_u = 2\pi/\lambda_u$ the undelator period.

The derivation of the wavelength (λ_{FEL}), characterizing the emission process inside the undulator, can be obtained using a fairly simple argument. The difference in velocities is such that, after one undulator period, the radiation has slipped ahead of the electron beam by the so called *slippage length*

$$\delta = (c - v_z)\,\frac{\lambda_u}{c} = (1 - \beta_z)\;\lambda_u \tag{3.2}$$

Since δ is linked to the phase advance of the electromagnetic wave with respect to the electrons, constructive interference of the wave front of the emitted radiation at the next undulator period is ensured if

$$\delta = \lambda_{FEL} \tag{3.3}$$

where λ is the frequency of the co-propagating field.

The last two equations yield the FEL resonance condition, which can also be cast in the form

$$\begin{aligned} \omega_{FEL} &= \frac{2\pi\, c}{\lambda_{FEL}} = \frac{\omega_u}{1 - \beta_z}, \\ \omega_u &= \frac{2\,\pi\, c}{\lambda_u} \end{aligned} \tag{3.4}$$

to this aim we note that the electrons, with relativistic factor γ, enter inside the undulator, where, on account of the Lorenz force induced by the magnetic field, acquire a transverse velocity component $\beta_\perp$, the longitudinal velocity can accordingly be written as

$$\begin{aligned} \beta_z &= \sqrt{1 - \frac{1}{\gamma_z^2}}, \\ \gamma_z &= \frac{\gamma}{\sqrt{1 + \alpha^2}} \end{aligned} \tag{3.5}$$

being $\beta_\perp^2 + \beta_z^2 = 1 - 1/\gamma^2$.

If the relativistic factor is large enough to allow a series expansion of the square root, in the first of the eqs. 3.5, at the lowest order in $\frac{1}{\gamma^2}$, results

$$\omega_{FEL} \cong 2\,\frac{\gamma^2}{1+\alpha^2}\omega_u \tag{3.6}$$

being $\alpha = K/\sqrt{2}$ with $K_{FEL} \propto eB_0\lambda_u$ the undulator strength which take into account the effect of the transverse motion on the longitudinal velocity [36]:

$$\begin{aligned} \beta_\perp &\approx \frac{K_{FEL}}{\sqrt{2}\gamma} \\ \beta_z &\approx 1 - \frac{1}{\gamma^{*2}} \end{aligned} \tag{3.7}$$

being $\gamma^* = \gamma/\sqrt{1 + K_{FEL}^2/2}$.

The previous derivation can be extended to CARM by noting that the relevant "***resonance***" condition, can be determined by using the same argument as before about constructive interference, which occurs whenever the accumulated slippage between radiation and electrons, in a helix period, equals the wavelength λ.

We remind that in a CARM-FEL a moderately relativistic e-beam, moves, inside a wave guide under the influence of an axial magnetic field, executing a helical path with a cyclotron frequency $\Omega_0 = \dfrac{e\,B}{m_e}$.

The kinematical variables of the electron beam are specified by the longitudinal (v_z) and transverse ($v_\perp$) velocity components, linked to the relativistic factor γ by

$$\begin{aligned} \beta_z^2 + \beta_\perp^2 &= 1 - \frac{1}{\gamma^2}, \\ \beta_{z,\perp} &= \frac{v_{z,\perp}}{c}, \\ \alpha &= \frac{v_\perp}{v_z} \end{aligned} \tag{3.8}$$

where α is the already defined pitch factor.

The electrons, with longitudinal velocity v_z, interact with a co-propagating electromagnetic field characterized by a wave-vector k_z, linked to the wave phase velocity v_p by

$$k_z = \frac{\omega}{v_p} \tag{3.9}$$

In this case the link between helix period and guiding magnetic field is provided by

$$\Lambda = \frac{c}{\Omega} \tag{3.10}$$

we impose the resonance condition as

$$(v_p - v_z)\,\frac{\Lambda}{c} = \lambda \tag{3.11}$$

where we have used the phase velocity v_p to determine the radiation electron slippage. This is nothing else that a different form of the condition 3.1.

The above equation has been derived by using a kinematical argument and the analogy with U-FEL has been the pivotal element of the discussion. The physical origin of the previous identity can however be understood on the basis of different arguments, involving e.g. momentum (electron and fields) conservation.

We can further elaborate the previous identities, denoting by ω_R the resonant frequency, we obtain, from eq. 3.1

$$\begin{aligned} \omega_{CARM} &= \frac{\Omega}{1 - \dfrac{v_z}{v_p}}, \\ \Omega &= \frac{\Omega_0}{\gamma} \end{aligned} \tag{3.12}$$

It is worth stressing that, being the phase velocity dependent on the field frequency, eq. 3.12 is not an explicit solution for ω, but only an approximation.

Before further pushing the analogy between U and CARM FEL, we dwell on the physical meaning of the previous equations.

The CARM resonance condition can also be derived by requiring the matching between eq. 3.1 and the waveguide dispersion relation

$$\omega^2 = c^2(k_\perp^2 + \beta_p^2 k_z^2) \tag{3.13}$$

where $k_\perp$ is the transverse mode wave number, associated with the cutoff frequency $\omega_c = ck_\perp$. It is easily checked that, from 3.1 and 3.12, one gets

$$\omega_\pm \cong \frac{\Omega}{1 \mp \dfrac{\beta_z}{\beta_p}} \tag{3.14}$$

The down shifted intersection (see Fig.3.3), yielding the gyrotron mode [37], will not be considered in the following.

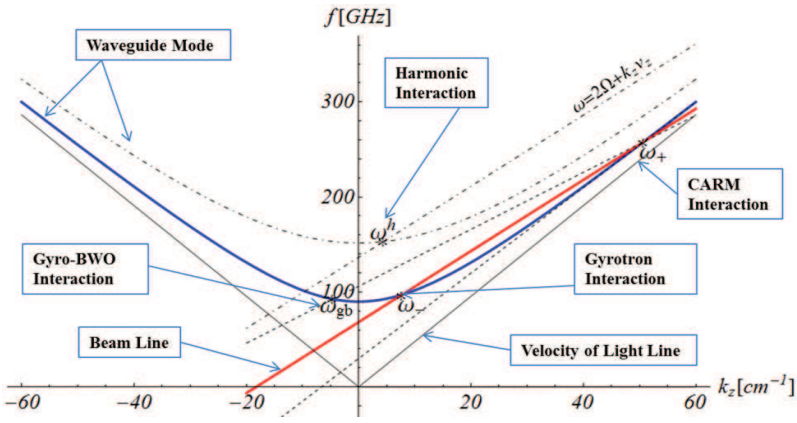

Figure 3.3: Brillouin diagram for the different conditions of electron cyclotron resonance selections provided by the intersections of the different beam lines (straight lines) whit the dispersion curves of the operating cavity mode.

The upper shifted counterpart ω_+ is the resonant (CARM) frequency and, to better understand its role, it will be rewritten as

$$\omega_{CARM} \cong \frac{\Omega}{1-\frac{\beta_z}{\beta_p}} = \frac{\Omega}{1-\frac{1}{\beta_p}\sqrt{1-\frac{1}{\gamma_z^2}}} \cong 2\beta_p\,\gamma_z^2\Omega, \qquad \gamma_z = \frac{\gamma}{\sqrt{1+(\gamma\beta_\perp)^2}} \tag{3.15}$$

according to the assumption that γ_z be sufficiently large that $\sqrt{1-\frac{1}{\gamma_z^2}} \cong 1-\frac{1}{2\,\gamma_z^2}$.

Eq. 3.15 accounts for the frequency Doppler up-shift mechanism, characterizing most of the free electron devices.

It is important to emphasize that, at least formally, we have established so far an important analogy between CARM and U-FEL, namely $\Lambda \leftrightarrow \lambda_u$, which justifies the remark that the two devices are "topologically" equivalent.

The role of the transverse velocity needs a more accurate comment. In the case of the U-FEL the transverse component, induced by the Lorenz force, is the tool allowing the coupling with the co-propagating electromagnetic (transverse) field (see Eq. 3.7).

In the case of the CARM the role of the transverse velocity component is the same as that of the undulator strength in the undulator FEL, as results comparing the Eqs. 3.7,3.15

$$K_{CARM} = \gamma\beta_\perp. \tag{3.16}$$

This velocity component should be induced during the electron beam preparatory phase, before the injection into the cavity.

What has been described so far are the physical conditions underlying the “spontaneous” emission, which is the prerequisite for the onset of the coherent emission process. As is well known, it occurs via the bunching mechanism. The interaction of the electrons with the cavity electric field mode determines their energy modulation, which transforms into a density modulation, followed by a coherent RF emission when the electrons are bunched on a scale comparable to the RF electric

field wavelength.

This description encompasses all devices of FEL type, CARM is however made peculiar by the fact that the auto-resonance is guaranteed even near saturation because any increase of Ω is balanced by a corresponding decrease of the longitudinal velocity[1].

A further important quantity, characterizing U-FEL, is the number of undulator periods, which is associated with the oscillations executed by an electron, while travelling inside the undulator. In the case of CARM it can be linked to the number of helical turns of the electrons inside the magnet. Accordingly we get

$$\begin{aligned} \Omega \frac{L}{\beta_z c} &= 2\,\pi\,N \\ N &\cong \frac{L}{\Lambda} \end{aligned} \tag{3.17}$$

We have fixed the main element of our strategy and in the following section we will see how the correspondences, we have established, may provide an effective tool to evaluate the CARM evolution.

3.1.1 Small Signal Theory: FEL vs CARM analytical solution

In this section we will push further the analogy with U-FEL by showing that the equation describing the CARM field evolution in the linear regime, can be written by taking advantage from simplified expression valid in the former case.

In the analysis of the previous section we did not include any consideration regarding the interaction of the wave with the e-beam. The dispersion relation in Eqs. 3.7-3.13 are appropriate for the "cold" wave guide condition, which merely applies to

[1]The efficiency enhancement is induced in undulator based FELs by tapering the undulator, by reducing e.g. the undulator period, in order to maintain the resonance condition in eq. 3.4 fixed when β_z decreases, thus realizing the effect naturally entangled with CARM operating mechanism.

the kinematic of the mode propagation.
The CARM dynamics, associated with the radiation intensity growth in the wave guide, undergoes different phases characterized by the amount of the field power density.
The weak coupling regime is characterized by a power level well below the threshold of the saturation intensity (namely the power density halving the small signal gain) and the relevant theory can be treated using perturbative methods and, to some extent, useful information can be drawn using analytical means.

We have stressed that the mechanisms leading to the CARM process are closely similar to those leading to U-FEL, we can therefore suspect that a closely analogous set of equations can be exploited to describe both devices.

The CARM beam-wave interaction can be described with a self-consistent physical model, as discussed by different authors [37, 38, 39, 40], in terms of three dimensionless parameters which take into account the appropriate kinematic conditions matching the electron longitudinal and wave group velocity and the cyclotron frequency. Within such a context a pivotal parameter is the frequency detuning δ defined as

$$\delta = 1 - \frac{\beta_z}{\beta_{ph}} - \frac{\Omega}{\omega_r}, \tag{3.18}$$

where, $\beta_{ph} = v_{ph}/c$, $\beta_z = v_z/c$, are the phase velocity and longitudinal velocities of the electrons, respectively, normalized to the speed of the light, $\Omega = eB/(m\gamma)$ is the relativistic cyclotron frequency with B the external magnetic field. Being the CARM a laser-like device, a further quantity of crucial importance is the small signal gain coefficient which, within this framework, can be written as

$$I_g = \frac{2\mu_0|e|}{mc\gamma}\frac{\beta_{ph}}{\beta_\perp^4}\frac{\left(1-\frac{\beta_z}{\beta_{ph}}\right)^3}{\left(1-\beta_{ph}^{-2}\right)}I_0[CJ]^2, \tag{3.19}$$

where $\beta_\perp = v_\perp/c$ is the transverse velocities of the electrons normalized to the speed of the light, I_0 is the beam current and $[CJ]$ is the beam-wave overlapping coefficient. Finally the peculiar nature of the CARM offers the possibility of achieving large efficiency, as a consequence of the auto-resonance mechanism, and the quantity controlling such effect is the recoil parameter reported below

$$b = \frac{\beta_\perp^2}{2\beta_z\beta_{ph}\left(1-\frac{\beta_z}{\beta_{ph}}\right)}, \tag{3.20}$$

Furthermore, the CARM beam-wave interaction is described by the following set of differential equation [38, 39] (see Ceccuzzi et al. [41] for the relevant approximations)

$$\begin{aligned}
\frac{dF}{d\zeta} &\approx I_g \left\langle e^{i\theta} \right\rangle_{\theta_0} + \left[\overline{I}_g \left\langle u e^{i\theta} \right\rangle_{\theta_0} \right], \; \overline{I}_g = \left(b - \frac{1}{2} \right) I_g \\
\frac{du}{d\zeta} &\approx Re[F e^{-i\theta}] \\
\frac{d^2\theta}{d\zeta^2} &\approx (b\Delta - 1)|F| cos(\theta + \phi) - \left\{ b \frac{d}{d\zeta} \mathfrak{Q}(\zeta) - \frac{1}{2} \frac{d}{d\zeta} Re(iFe^{-i\theta}) \right\} \\
\frac{d\mathfrak{Q}(\zeta)}{d\zeta} &\approx -Re(i \frac{dF_s}{d\zeta} e^{-i\theta})
\end{aligned} \tag{3.21}$$

where the normalized u, θ variables are associated with the electron energy and the electron-wave phase respectively, $\mathfrak{Q}$ is the axial momentum correction, ζ is the normalized space variable and $< ... >_{\theta_0}$ accounting the average on the initial phase distribution. The terms within square and curly brackets and the second equation, accounting for the energy variation, can be neglected in the small or weakly saturated regime. We are therefore left with a pendulum like equation and the first, accounting for the field amplitude evolution, in full analogy with the U-FEL case.

In the other side, a significant result from such a treatment is the derivation of a modified dispersion relation including the interaction of the electrons with the wave guide modes linearizing the Maxwell-Vlasov equation[40]. According to refs. [37, 40] we find

$$\frac{\omega^2}{c^2} - (k_\perp^2 + k_z^2) + \tilde{\varepsilon}_{mnl} \frac{2k_\perp^2 (\omega - k_z v_z)}{\left(\omega - \frac{\Omega_0}{\gamma} - k_z v_z \right)} - \tilde{\varepsilon}_{mnl} \frac{k_\perp^2 \beta_\perp^2 (\omega^2 - c^2 k_z^2)}{\left(\omega - \frac{\Omega_0}{\gamma} - k_z v_z \right)^2} = 0, \tag{3.22}$$

where $\tilde{\varepsilon}_{mnl}$ plays the role of coupling parameter, being (m, n) the interacting waveguide mode number and l the harmonics of the electron cyclotron frequency due to the axial magnetic field. It depends on the beam current and on the geometrical parameters of the waveguide itself and will be specified later in this section. In eq. (3.22) the terms containing the coupling ε_{mnl} are those ruling the field electron evolution, we simplify the analysis by neglecting the first because the second is dominating near the resonance. We are therefore left with

$$\frac{\omega^2}{c^2} = (k_\perp^2 + k_z^2) - \varepsilon_{mnl} \frac{k_\perp^2 \left(\omega^2 - c^2 k_z^2\right)}{\left(\omega - \dfrac{\Omega_0}{\gamma} - k_z v_z\right)^2}. \tag{3.23}$$

The previous identity is the crucial element of the forthcoming discussion and, for later convenience, we set

$$\begin{aligned} \tilde{k}_z &= k_z + \delta_{k_z}, \\ k_z &= \left(\frac{\omega^2}{c^2} - k_\perp^2\right)^{\frac{1}{2}} = \frac{\gamma\omega - \Omega_0}{\gamma v_z} \end{aligned} \tag{3.24}$$

with δ_{k_z} representing the deviation of the field longitudinal wave vector, induced by the coupling with the electrons. Inserting eq. 3.24 into 3.23 we find that δ_{k_z} is specified by the following fourth order algebraic equation

$$\beta_z^2 \delta_{k_z}^4 + 2\beta_z^2 k_z \delta_{k_z}^3 + \varepsilon_{mnl} k_\perp^2 \delta_{k_z}^2 + 2\varepsilon_{mnl} k_\perp^2 k_z \delta_{k_z} - \varepsilon_{mnl} k_\perp^4 = 0 \tag{3.25}$$

The roots of the above equation specifies the evolution of the CARM field amplitude along the coordinate z, according to

$$E(z) \propto \sum_{j=1}^{4} e_j e^{i(\delta_{k_z})_j z} \tag{3.26}$$

where j refers to the roots of eq. 3.25 and e_j are integration constants, fixed by the conditions

$$\begin{aligned} &E(0) = 1, \\ &\left(\left(\frac{d}{dz}\right)^k E(z)\right)_{z=0} = 0, \\ &k = 1,\ 2,\ 3. \end{aligned} \tag{3.27}$$

Neglecting the opposite propagation wave $\omega - kc$, the dispersion relation 3.22 will be reduced of one order and taking into account a small value for δ_{kz} results[37]

$$\cancel{\beta_z^2 x^4} + 2\beta_z^2 (t^2-1)^{1/2} x^3 + \cancel{\epsilon_{mnnl}^{TE} x^2} + \cancel{2\epsilon_{mnnl}^{TE} (t^2-1)^{1/2} x} - \epsilon_{mnnl}^{TE} = 0 \tag{3.28}$$

whose imaginary solution is given by the following expression

$$\Gamma_{mnl} = K \left(\frac{\epsilon^{TE}_{mnnl}}{\beta_z^2 (t^2-1)^{(1/2)}} \right)^{1/3} \quad \text{with} \quad K = \frac{3^{1/2}}{2^{4/3}} \tag{3.29}$$

In Fig.3.4 are reported the imaginary solution of the forth (Eq. 3.25) and third order (Eq. 3.29) polynomial versus the normalized resonance frequency $(\Omega/(ck_{11}))$ for an electron beam energy of 1 MeV with 500 A of current interacting with the TE_{11} mode of a waveguide having a radius $r_w = 1.4$ cm[40]. At the resonance condition $(\Omega/(ck_{11}) = 2.87)$, achieved with an external axial magnetic field $B_0 = 4.01$ kG, the difference of two solutions is reasonable.

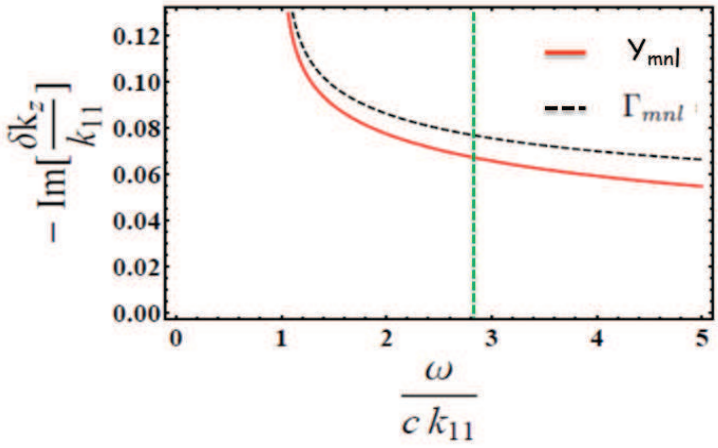

Figure 3.4: The imaginary part of the complex conjugate solution of the forth degree polynomial(black-dashed line) and of the approximate cubic polynomial(red-continuously line) versus the normalized frequency. The vertical orange line is the normalized resonance frequency

The linearized field growth along the longitudinal coordinate can accordingly be obtained by plotting $|E(z)|^2$ as shown in Figs. 3.5, 3.6.

The evolution curve has the well-known shape, characterizing also the Self Amplified Spontaneous Emission (SASE) FEL operating mode, namely a lethargy region where the system (electrons and radiation) organizes the coherence and a linear (in logarithmic scale) growth with a characteristic gain length l_g. In the case of CARM such a quantity is specified by [40]

$$l_g^{-1} = 2\Gamma_{mnl} = \sqrt{3}\left[\frac{\varepsilon k_\perp^4}{16 k_z \beta_z^2}\right]^{\frac{1}{3}} \tag{3.30}$$

Let us now invoke the analogy with the U-FEL, whose gain length is defined as [42]

$$l_g = \frac{\lambda_u}{4\,\pi\,\sqrt{3}\,\rho} \tag{3.31}$$

with ρ being the Pierce parameter linked to the small signal gain coefficient g_0 by the identity [42]

$$\rho = \frac{(\pi\, g_0)^{\frac{1}{3}}}{4\,\pi\, N} \tag{3.32}$$

The use of the correspondences established in the previous section and the comparison between eqs. 3.30, 3.31 allows the following identification

$$\rho = \frac{\Lambda\,\Gamma}{4\,\pi\,\sqrt{3}} \tag{3.33}$$

The dependence of U-FEL field amplitude on the longitudinal coordinate has been shown to be provided by [36, 42]

$$\begin{aligned}
a(\tau) &= \frac{a_0}{3(\nu+p+q)} e^{-\frac{2}{3}i\nu\tau}\left\{(-\nu+p+q)e^{-\frac{i}{3}(p+q)\tau} + \right. \\
&\left. +2(2\nu+p+q)e^{\frac{i}{6}(p+q)\tau}\left[\cosh\left(\frac{\sqrt{3}}{6}(p-q)\,\tau\right) + i\frac{\sqrt{3}\nu}{p-q}\sinh\left(\frac{\sqrt{3}}{6}(p-q)\,\tau\right)\right]\right\}, \\
p &= \left[\frac{1}{2}(r+\sqrt{d})\right]^{\frac{1}{3}}, \qquad q = \left[\frac{1}{2}(r-\sqrt{d})\right]^{\frac{1}{3}}, \\
r &= 27\,\pi\,g_0 - 2\,\nu^3, \qquad d = 27\,\pi\,g_0\left[27\,\pi\,g_0 - 4\,\nu^3\right]
\end{aligned} \tag{3.34}$$

and the intensity evolution is just given by $|a(\tau)|^2$.

The various parameters entering the above expression are recognized as

$\nu \equiv$ Detuning parameter
$z \equiv$ Longitudinal coordinate
$L \equiv N\,\lambda_u \equiv$ Interaction length
$\tau \equiv$ Dimensionless time

We can now get the correspondence with the CARM variables is obtained by defining the normalized detuning $\bar{\nu}$ parameter as

$$\bar{\nu} = \frac{\nu}{(27\pi\ g_0)^{1/3}} \tag{3.35}$$

and then by casting, using the relations 3.30-3.32, the dimensionless time in the form

$$\tau = \frac{z}{L} = \frac{z}{Nl_g 4\ p\ \sqrt{3}\rho} = \frac{2\ \Gamma z}{\sqrt{3}(pg_0)^{\frac{1}{3}}} \tag{3.36}$$

Thus finally ending up with

$$\nu\tau = 2\sqrt{3}\Gamma\bar{\nu}z \tag{3.37}$$

The complex amplitude 3.34 can now be assumed to be a function of the normalized detuning parameter $\bar{\nu}$ and of the inverse gain length Γ, which will be exploited to describe the small signal growth of the radiation field amplitude, namely

$$\begin{aligned} a(z,\Gamma,\bar{\nu}) &= \frac{a_0}{3} e^{-i\frac{4\Gamma\bar{\nu}z}{\sqrt{3}\beta_z}} \cdot \\ &\cdot \left\{ A_1 e^{-i\frac{2\Gamma z A_3^{(+)}}{\sqrt{3}}} + 2A_2 e^{i\frac{\Gamma z A_3^{(+)}}{\sqrt{3}}} \cdot \left[\cosh(\Gamma z A_3^{(-)}) + i\frac{\sqrt{3}\bar{\nu}}{A_3^{(+)}} \sinh(\Gamma z A_3^{(-)}) \right] \right\} \end{aligned} \tag{3.38}$$

with

$$
\begin{aligned}
A_1 :=& A_1(\bar{\nu}) = \frac{(-\nu + p + q)}{\nu + p + q} = \\
&= \frac{\left(\sqrt[3]{1 - 2\bar{\nu}^3 + \sqrt{1 - 4\bar{\nu}^3}} + \sqrt[3]{1 - 2\bar{\nu}^3 - \sqrt{1 - 4\bar{\nu}^3}} - \sqrt[3]{2}\bar{\nu}\right)}{\left(\sqrt[3]{1 - 2\bar{\nu}^3 + \sqrt{1 - 4\bar{\nu}^3}} + \sqrt[3]{1 - 2\bar{\nu}^3 - \sqrt{1 - 4\bar{\nu}^3}} + \sqrt[3]{2}\bar{\nu}\right)}, \\
A_2 :=& A_2(\bar{\nu}) = \frac{(2\nu + p + q)}{\nu + p + q} = \\
&= \frac{\left(\sqrt[3]{1 - 2\bar{\nu}^3 + \sqrt{1 - 4\bar{\nu}^3}} + \sqrt[3]{1 - 2\bar{\nu}^3 - \sqrt{1 - 4\bar{\nu}^3}} + 2\sqrt[3]{2}\bar{\nu}\right)}{\left(\sqrt[3]{1 - 2\bar{\nu}^3 + \sqrt{1 - 4\bar{\nu}^3}} + \sqrt[3]{1 - 2\bar{\nu}^3 - \sqrt{1 - 4\bar{\nu}^3}} + \sqrt[3]{2}\bar{\nu}\right)}, \\
A_3^{(\pm)} :=& A_3^{(\pm)}(\bar{\nu}) = \frac{1}{\sqrt[3]{2}}\left(\sqrt[3]{1 - 2\bar{\nu}^3 + \sqrt{1 - 4\bar{\nu}^3}} \pm \sqrt[3]{1 - 2\bar{\nu}^3 - \sqrt{1 - 4\bar{\nu}^3}}\right), \\
(p \pm q)\tau =& \frac{\sqrt{3}}{\sqrt[3]{2}} 2\Gamma z \left(\sqrt[3]{1 - 2\bar{\nu}^3 + \sqrt{1 - 4\bar{\nu}^3}} \pm \sqrt[3]{1 - 2\bar{\nu}^3 - \sqrt{1 - 4\bar{\nu}^3}}\right) = \\
&= 2\sqrt{3}\Gamma z A_3^{(\pm)}
\end{aligned}
\tag{3.39}
$$

In Fig. 3.5 we have provided a comparison between the prediction of the CARM theory and of the U-FEL scaling equations, given in eq. 3.34. The agreement is satisfactory and further comments will be given below.

We should put in evidence that the linear solution obtained solving the dispersion relation 3.23 has been regularized neglecting the oscillating root of the equation 3.25 as reported in Fig. 3.6 the comparison of the amplitude signal with and without the oscillating solution .

The following two remarks are in order to complete the previous discussion

a) The dispersion relations for CARM and U-FEL lead to a fourth and third degree algebraic equations respectively. This is a consequence of the fact that the CARM field equations have been derived without the assumption of paraxial approximation, while, in the case of U-FEL the small signal problem is solved by the approximation of slowly varying envelope (SVE). This assumption leads

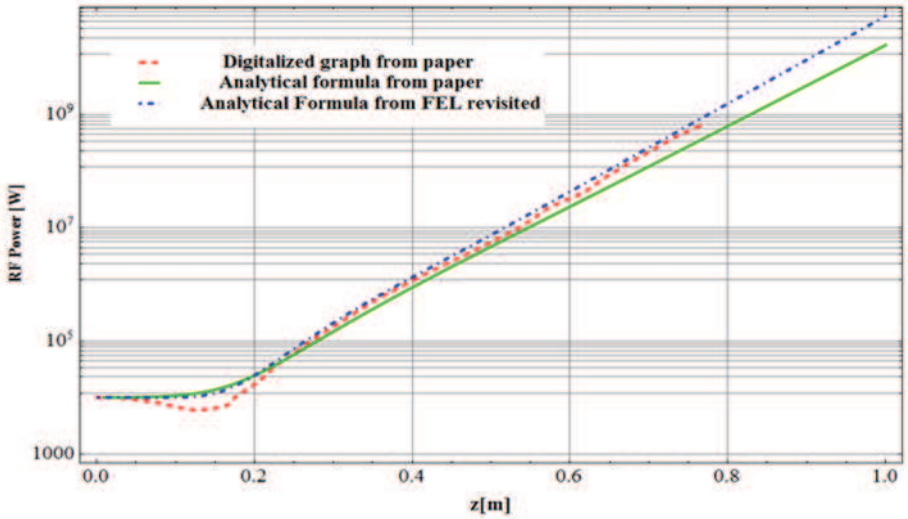

Figure 3.5: Comparison between U-FEL (blue) and CARM (green) SSR (small signal growth) intensity growth curves with the result reported in the Wurtele paper ref. [40].

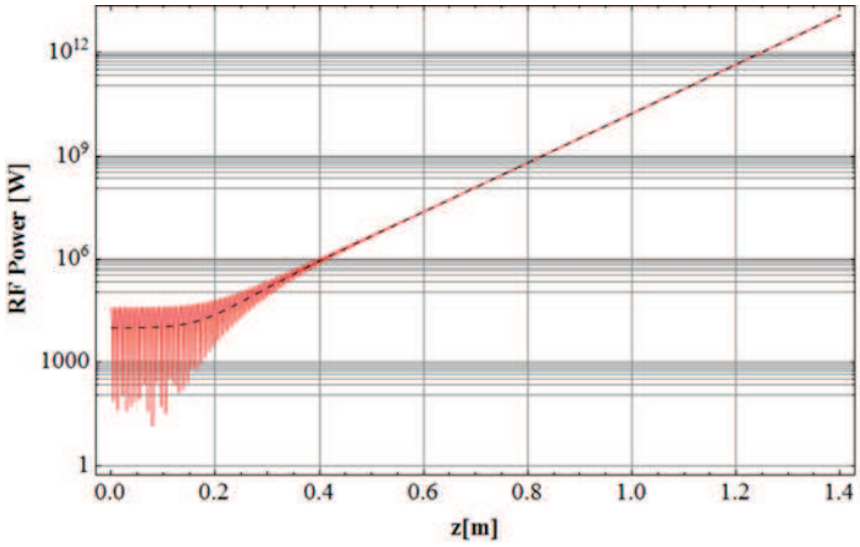

Figure 3.6: The growth intensity of the Small signal CARM by solving the the forth order equation Eq. 3.25(continuously red line) and neglecting the one of the real root(dashed black line).

to a treatment involving algebraic equations of one degree lower. In adapting U-FEL to CARM theory, according to the previous prescriptions and to ref. [39], we did not find particular differences, except for the lethargic parts,

where the SVE approximation is not fully justified and smoothen the field oscillations.

b) The Eqs. 3.23-3.30 have been written without fixing the waveguide mode structure, we can however factorize the ε coupling parameter as the product of two terms, namely

$$\begin{aligned} \varepsilon &= \Xi\, \mathrm{f}, \\ \mathrm{f} &= \frac{4\,\pi\,\beta_\perp^2}{\gamma\,\beta_z}\left(\frac{I_b}{I_A}\right) \end{aligned} \tag{3.40}$$

where $I_{b,A}$ denote the beam and Alfvén current, the parameter Ξ summarizes the details of the cavity mode and the effect due to the geometrical overlapping between electrons and wave-guide modes and will be more carefully discussed in the following.

3.2 Non-Linear Regime and Saturated Power

In the previous section we have developed quite a straightforward formalism to prove that most of the scaling formulae developed within the framework of FEL theory can be adapted to the study and design as well of CARM devices, at least for the case of small signal regime.
In this section we include the non-linear contributions and show that the logistic curve model [42, 43] is an effective tool to study the evolution of the system up to the saturation.
The logistic growth curve belongs to the family of S-shaped curves, the model has been shown to be very effective in reproducing the evolution of any system undergoing a dynamical behavior ruled by an equation of the type

$$\frac{d}{d\,z}\mathrm{P} = \frac{\mathrm{P}}{l_g}\left[1 - \frac{\mathrm{P}}{\mathrm{P_S}}\right] \tag{3.41}$$

even though either CARM and U-FEL satisfy more complicated non- linear equations as to the growth of the power density. Eq. 3.41 captures the essential physics of the problem, namely a linear growth followed by a quadratic non linearity when

the power approaches $\mathrm{P_S}$ which denotes the saturated power. The solution of Eq. 3.41 can be written as

$$\mathrm{P}\left(z\right) = \mathrm{P}_0 \frac{e^{\frac{z}{l_g}}}{1 + \frac{\mathrm{P}_0}{\mathrm{P_S}}\left[e^{\frac{z}{l_g}} - 1\right]} \tag{3.42}$$

The definition of the CARM saturated power $\mathrm{P_S}$ is easily given by just following the prescription of ref. [44], we therefore set

$$\mathrm{P_S} \cong \eta\, P_E \tag{3.43}$$

where P_E is the electron beam power and η the efficiency of the device in turn provided by

$$\begin{aligned} &\eta = \eta_{sp}\eta_C, \\ &\eta_{sp} \cong \sqrt{2}\rho \\ &\eta_C \cong \frac{1}{\left(1 - \beta_p^{-2}\right)\left(1 - \gamma_0^{-1}\right)} \frac{\beta_\perp^2}{b} \end{aligned} \tag{3.44}$$

where we have denoted by $\eta_{sp,\,C}$ the single particle and collective efficiency, respectively [37]. The single particle efficiency, can be written using the analogy in terms of the Pierce parameter as t

$$\eta_{sp} \cong \sqrt{2}\rho = \frac{\sqrt{2}\Lambda\,\Gamma}{4\,\pi\,\sqrt{3}} \tag{3.45}$$

According to the previous identity the saturated power can be cast in the form

$$\begin{aligned} &\mathrm{P_S} \cong \frac{\sqrt{2}}{4\pi\sqrt{3}} \frac{\Lambda\,\Gamma}{\left(1 - \beta_p^{-2}\right)\left(1 - \gamma_0^{-1}\right)} \frac{\beta_\perp^2}{b} P_E, \\ &b = \frac{\beta_\perp^2}{2\,\beta_z \beta_p \left(1 - \frac{\beta_z}{\beta_p}\right)} \end{aligned} \tag{3.46}$$

According to the terminology of ref. [37],[38], b denotes the electron recoil parameter. It accounts for the auto-resonance contribution, including the effect of axial momentum and velocity change with the electron energy loss [44]. Regarding the

analogy with U-FEL it can be associated with the undulator tapering parameter [42, 45].

We have recovered all the crucial parameters (gain length and saturated power) to draw the CARM power growth curve, using the logistic equation. However, eq. 3.42 accounts only for the exponential growth prior the saturation and does not contain any lethargic phase. To overcome this problem we replace the exponential term in eq. 3.42 with the square modulus of the small signal amplitude derived in the previous section, thus writing

$$\begin{aligned} P(z) &\cong \mathrm{P}_0 \frac{|\beta(z)|^2}{1+\frac{\mathrm{P}_0}{\mathrm{P}_\mathrm{S}}\left(|\beta(z)|^2-1\right)}, \\ \beta(\tau) &= \frac{a(\tau(z))}{a_0} \end{aligned} \tag{3.47}$$

To check the validity of the previous formula we have developed an ad hoc numerical GRAAL (Gyrotron Radiation Amplification Auto-Resonance Laser) code to integrate the CARM equations which will be described in the next section.

3.2.1 The 1D GRAAL code

The dynamical systems accounting for the evolution of CARM devices is described by a set of equations coupling electrons and field refs. [37, 38, 46].
As described previously, the pivotal parameters characterizing the CARM dynamics are summarized by three dimensionless quantities: b, accounting for the auto-resonance (see Eq.3.20), Δ, normalized detuning (see Eq.3.18)

$$\Delta = \frac{2\left(1-\frac{\beta_z}{\beta_p}\right)^2\left(1-\frac{\omega_R}{\omega}\right)}{\beta_\perp^2(1-\beta_p^{-2})} \tag{3.48}$$

and I_g normalized beam current, proportional to the beam current I_b and expressible in terms of ρ parameter as

$$I_g = \left[\frac{4\sqrt[3]{2}\left(1 - \frac{\beta_z}{\beta_p}\right)}{\beta_\perp^2\left(1 - \beta_p^{-2}\right)}\,\rho \right]^3 \tag{3.49}$$

In terms of these parameters the CARM energy and phase equations, for TE modes interaction, can be cast in the form[37, 38, 46]

$$\begin{aligned} \frac{du}{d\zeta} &= \frac{[1-u]^{\frac{s}{2}}}{1-bu} Re(F_s e^{-i\theta}) \\ \frac{d\theta}{d\zeta} &= \frac{1}{1-bu}\left[\Delta - u - b\mathfrak{Q}(\zeta) + \frac{s}{2}[1-u]^{\frac{s}{2}-1} Re(iF_s e^{-i\theta})\right] \\ \frac{d\mathfrak{Q}(\zeta)}{d\zeta} &= -\frac{[1-u]^{\frac{s}{2}}}{1-bu} Re(i\frac{dF_s}{d\zeta} e^{-i\theta}) \end{aligned} \tag{3.50}$$

The normalized u, θ variables are associated with the electron energy and the electron-wave phase respectively, s is the order of the harmonics and F_s accounts for the complex mode field amplitude, whose evolution is fixed by the equation

$$\frac{dF_s}{d\zeta} = I_g \left\langle \frac{[1-u]^{\frac{s}{2}}}{1-bu} e^{i\theta} \right\rangle \tag{3.51}$$

From the mathematical point of view the problem is that of solving a system of nonlinear ODE, consisting of four differential equations three of which accounting for the electron motion and the other for the complex field amplitude evolution inside the cavity.

The adopted numerical procedure foresees the use of a Runge-Kutta scheme for the electron dynamics, with the field amplitude kept constant during one discretization step. Furthermore, a finite difference method has been applied to evaluate the differential equation concerning the amplitude wave evolution, in which the crucial step is the careful average on the electron phase distribution and on the transverse velocity distribution in order to include correctly the effect of the beam qualities.
To study the effect of the particles velocity spread, starting form a fixed γ_0 beam energy and an α_0 pitch, a Gaussian distribution of the transverse velocity has been

generated centred at the initial value of $\beta_{\perp 0}$.
For each particle we considered an ODE system characterized by a b($\beta^i_{\perp 0}$) and $\Delta(\beta^i_{\perp 0})$ parameter and the integral average on the electron phase and velocity distribution, has been evaluated by the use of a standard trapezoidal scheme.
Furthermore, the orbital efficiency has been obtained, by averaging the electron motion on the electron phase and velocity distribution, allowing to evaluate the CARM power growth.

The comparison between eq. 3.47 and the power evolution obtained via the numerical implementation are shown in Figs. 3.7, 3.8. The two curves compare fairly well; the use of these formulae for fixing the working points of a CARM device is therefore justified.

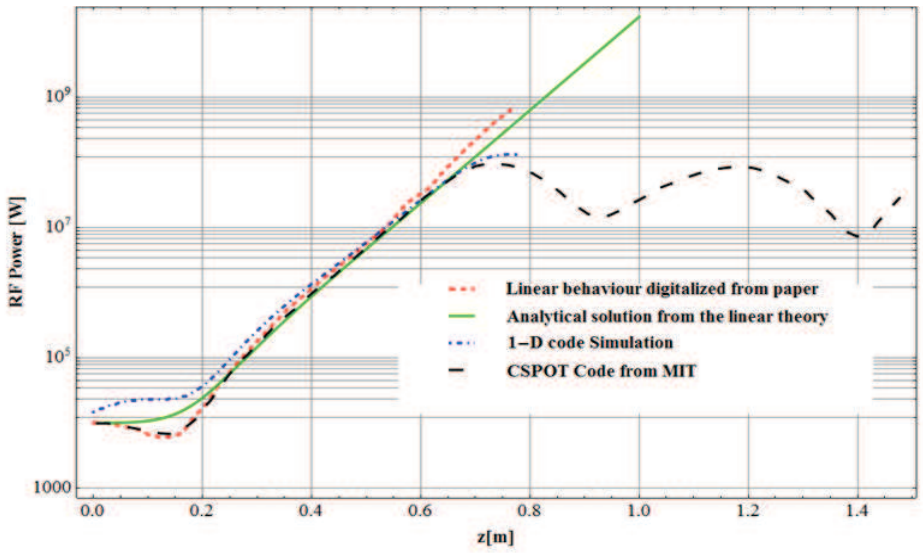

Figure 3.7: The analytical growth linear rate of the signal compared with the numerical simulation.

We have so far shown that a wise application of the CARM theory and U-FEL scaling formulae developed in the past may provide a heuristic tool useful for CARM device design. Further "practical" consequences from our treatment will be drawn in the forthcoming section.

The impact of the beam qualities, demanding for a high performance electron

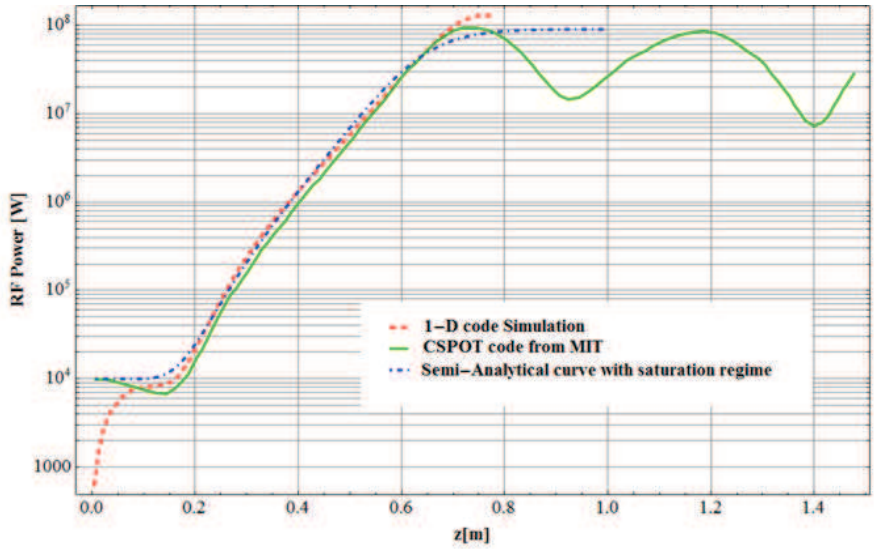

Figure 3.8: The revisited semi-analytical formula from FEL compared with numerical code.

beam which leads to an appropriate modeling of the gun as discussed previously, on the output power will be analyzed in the forthcoming section deriving appropriated scaling laws.

3.3 FEL to CARM scaling law

Before going further, we note that the complexity of the description of the free electron like devices stems from the large number of parameters characterizing these systems. A possible simplification comes from the fact that a few key parameters (as well as an appropriate combination of them) can be selected to express quantities like gain or efficiency in terms of simple formulae.
The CARM saturated power on the beam velocity spread can be derived from an accurate analysis of the numerical data and by an extension of an analogous expression obtained in the past for the U-FEL operation[36]. In the case of CARM, one important parameter is the normalized current I_g introduced in refs. [46, 47]. Fig.3.9 shows the CARM efficiency vs. the frequency detuning δ for different values of I_g as used by GRAAL code in order to reproduce the data from ref. [40] regarding

a CARM operation at 18 GHz and regarding the homogeneously broadened operation (namely with a beam without any significant velocity spread). The procedure that we have developed to get a general formula providing the dependence of the efficiency vs. the velocity spread is summarized below.

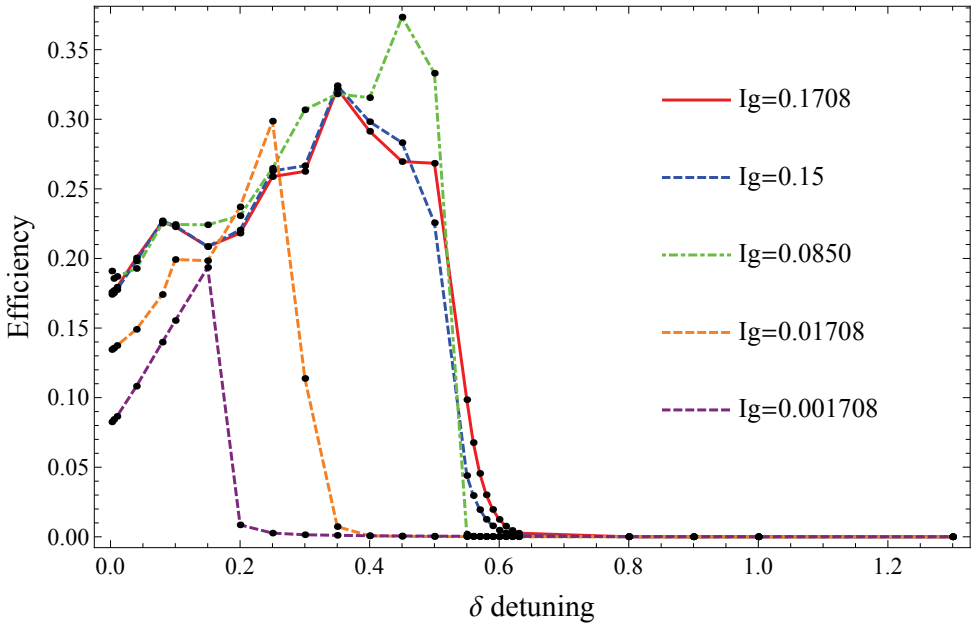

Figure 3.9: The efficiency versus the detuning parameter for a CARM amplifier at 18 GHz with a beam energy of 1.0 MeV and a pitch $(v_\perp/v_z)$ of 0.5 and an axial magnetic field $B_0 = 4.01\ kG$

After fixing the value of δ, maximizing the curves in Fig.3.9 for each normalized beam current, we have run the simulation taking into account the velocity spread and evaluated the corresponding efficiency. The results are presented in Fig.3.10a, where we have plotted the efficiency vs. the rms value $\sigma_{\beta_\perp}$ of the velocity spread (with a Gaussian distribution of the transverse velocity, centered at $\beta_{\perp 0}$, beam energy γ_0 and a pitch factor $\alpha_0 = v_{\perp 0}/v_{z0}$) for different I_g. A fit of the numerical data with a Lorentzian-like function yields the following expression

$$\eta = \frac{\eta_0}{1 + a\sigma^2_{\beta_\perp}}, \tag{3.52}$$

a being the fit parameter, $\sigma_{\beta_\perp}$ the beam velocity spread and η_0 the efficiency obtained neglecting the velocity spread of the beam electrons.

It has been found that the values of a, derived from the fitting procedure, strongly depend on the normalized current. It is therefore convenient to use a slightly different fitting strategy, involving the use of the inhomogeneous broadening parameters previously used for the study of U-FEL devices.
Taking advantage of the analogy between U-FEL and CARM devices and using the Pierce parameter (ρ) for CARM operation[48], it is possible to derive a "universal" semi-analytical curve describing the CARM efficiency. The pivotal parameter ruling the effect of velocity spread on CARM performances is completely equivalent to the inhomogeneous broadening parameter, already defined for a FEL device and reads [42]:

$$\mu_\varepsilon = \frac{2\sigma_{\beta_\perp}}{\rho}. \tag{3.53}$$

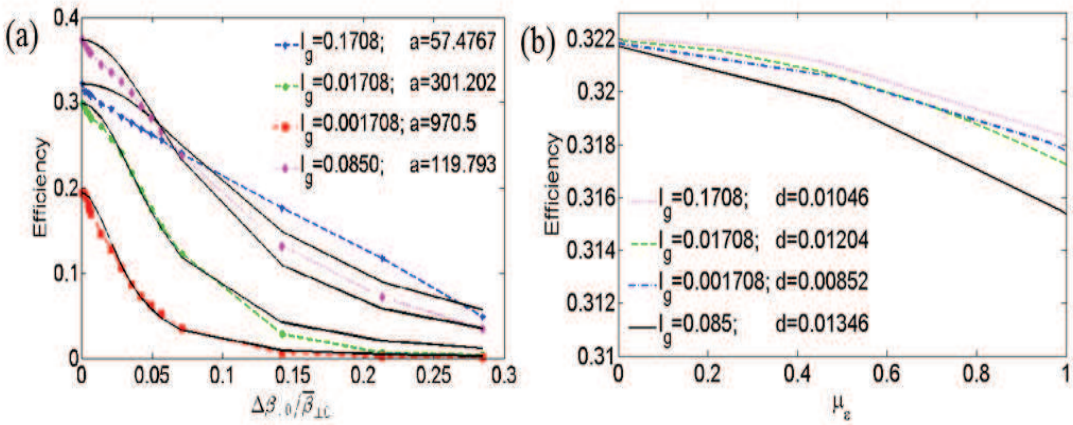

Figure 3.10: On the left side: a) the system efficiency using the beam parameters of Fig.3.9 for different normalized currents (dot-line) each of which fitted with a Lorentzian curve(continuous line);on the right side:b) the system efficiency versus the inhomogeneous broadening parameter

The efficiency versus μ_ε is plotted in Fig.3.10b). It is evident that the scaling reveals a kind of "universality" since the observed behavior is well reproduced by the relation

$$\eta = \frac{\eta_0}{1 + d\mu_\varepsilon^2}, \tag{3.54}$$

where the fit parameter d is almost the same for the different I_g . If we choose $d \approx 1.2 \cdot 10^{-2}$ the agreement between the numerical and the fitted values is more than satisfactory. It should, however, be stressed that the effect of beam quality

on the CARM saturation is almost negligible. The values we have assumed for the velocity spread (and hence for the corresponding μ_ϵ) are greatly exaggerated, since in the real CARM devices the values of μ_ϵ are significantly less than 1.
The problem of finding an appropriate scaling parameter in order to take into account the efficiency deterioration due to an insufficient the beam quality has been addressed in Ref.[47]. Similar criteria have been exploited in the cited paper, where the authors have employed an inhomogeneous scaling parameter proportional to the velocity spread through a coefficient depending on $I_g^{-1/2}$. In our case, in order to be consistent with the commonly accepted treatment of the U-FEL devices, we use $\mu_\varepsilon \propto I_g^{-1/3}$, and $\rho = 1/4\pi\chi I_g^{1/3}$ proportional to $I_g^{1/3}$.
The role of μ_ε is, however, manifold and allows the understanding of other parameters of pivotal importance, like the growth rate in a CARM device operating as an amplifier. As it is well known, the power growth increases, while the beam is propagating along the longitudinal axis as $P(z) \propto e^{z/L_g}$, where L_g is the gain length[48]. Moreover, a CARM amplifier operating with a beam of poor quality is characterized by larger values of L_g and therefore by a longer saturation length.
We have used a procedure analogous to that exploited for the efficiency to derive the dependence of L_g on $\sigma_{\beta_\perp}$. The analysis of the numerical data supports a quadratic dependence which can be expressed as (see Fig. 3.11a))

$$L_g = L_g^0 \left[1 + k\sigma_{\beta_\perp}^2\right], \tag{3.55}$$

k being the fitting parameter, strongly dependent on the different values of I_g . On the other side, the curves acquire a less dispersed behavior when plotted vs. μ_ε (see Fig. 3.11b).

This is however not the end of the story, because, as shown in Fig. 3.10a, the efficiency is extremely sensitive to the beam characteristics. An inspection to the figure shows that if the velocity spread slightly increases we may expect a significant decrement of the efficiency. To be on the safe side and ensure an operation of the CARM device with a sufficiently large efficiency the driving the use of a beam of electrons with "reasonably" small dispersion of the energy and velocity distributions. We can obtain an upper limit to the previously quoted dispersions, by noting that

1. The inhomogeneous line broadening induced by the longitudinal velocity spread

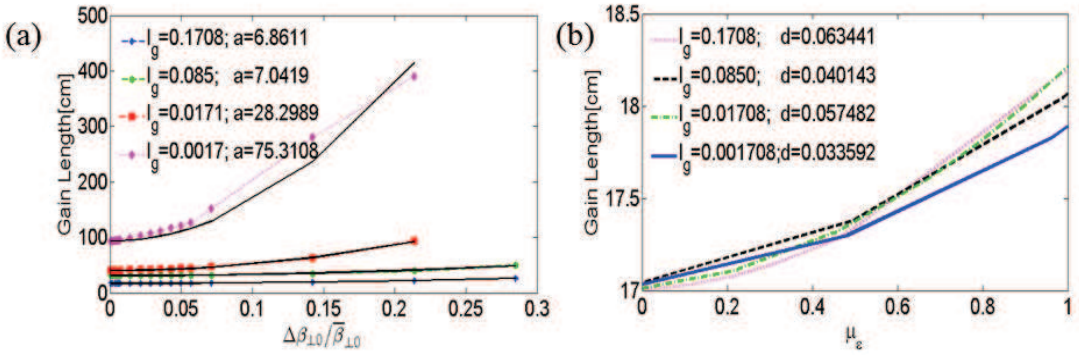

Figure 3.11: On the left side: a) the gain length obtained from the simulation data taken from the example reported in Fig.3.9 for different values of the normalized current (dot-line) each of which is fitted with a parabolic curve(continuous line);on the right side:b) the gain length versus the inhomogeneous broadening parameter

is (see Eqs. 3.15 with $\beta_p \approx 1$)

$$\left\langle \frac{\Delta\omega}{\omega} \right\rangle \cong \frac{\sigma_{\beta_z}}{1-\beta_z} \tag{3.56}$$

requiring that it be smaller than its homogeneous counterpart we end up with the following condition on σ_{β_z}

$$\frac{\sigma_{\beta_z}}{1-\beta_z} < \frac{1}{N} \tag{3.57}$$

2. From eq. 3.8 we end up with

$$\alpha^2\sigma_{\beta_z} + \sigma_{\beta_\perp} = \frac{1}{\overline{\alpha}}\sigma_\gamma \tag{3.58}$$

Using therefore $\sigma_{\beta_\perp} \leq 10^{-3}$ (as suggested by Fig. 3.10) and $\sigma_{\beta_z} \leq 3{\cdot}10^{-3}$ (as derived from eq. 3.57) we find $\sigma_\gamma \leq 0.5\%$.

3.4 Transverse Mode Selection: Operating Configuration

The coefficient Ξ reported in Eq. 3.40 summarizes quite a complicated expression including the transverse mode structure and should indeed be characterized by the

indices *m, n, l* labeling the TE mode coupling and the overlapping integral with the beam itself.

This last quantity defines the filling factor, which, in turn affects the gain coefficient and the gain length as well. The problem becomes more and more serious when higher order modes are considered for lasing. In this case the relevant spatial distribution is not provided by a Gaussian, covering smoothly a transverse surface as for TE_{11} mode, but by a kind of circular corona which, as already stressed, demands for an appropriate shaping of the transverse structure of the e-beam to optimize the coupling. Accordingly the beam transverse distribution should be modeled as a thin circular corona.

In Figs. 3.12 we have shown the linear part of the intensity evolution, along the z direction, together with the associated mode distribution. According to the previous remarks, it is not surprising that some collections of mode tend to grow in practically a undistinguishable way.

We must emphasize that, although Figs. 3.12 put the caveat that many transverse modes can be locked at saturation (thus creating problems of efficiency reduction), it should be stressed that it accounts for the fast growing root only and therefore it might lead to "pessimistic" conclusions.

The "degeneration" of the transverse mode evolution can however be removed by analyzing the relevant growth through the inclusion of all the roots of the dispersion equation. The transverse mode power growth is given in Fig. 3.13 which shows a more complicated growth pattern.

In conclusion although the cavity is evidently over-moded (see Fig. 3.14), the use of a convenient shaping of the annular electron beam may allow an efficient tool of mode selection, as further discussed in the following.

Furthermore, the equations system given by the dispersion relation of the resonance condition (Eq. 3.1) and the dispersion relation for the modes in a waveguide (Eq. 3.13) leads to the following expression for the CARM resonance (ω_+ in Fig.3.3)

$$\omega_+ = \frac{\beta_z^{-2}\Omega/\gamma - \sqrt{\omega_{cutoff}^2(1-\beta_z^{-2}) + \beta_z^{-2}\Omega^2/\gamma^2}}{\beta_z^{-2}-1} = \tag{3.59}$$

$$= \frac{\beta_z^{-2}\Omega\sqrt{1-\beta_z^2(1+\alpha^2)} - \sqrt{\omega_{cutoff}^2(1-\beta_z^{-2}) + \beta_z^{-2}\Omega^2(1-\beta_z^2(1+\alpha^2))}}{\beta_z^{-2}-1} \tag{3.60}$$

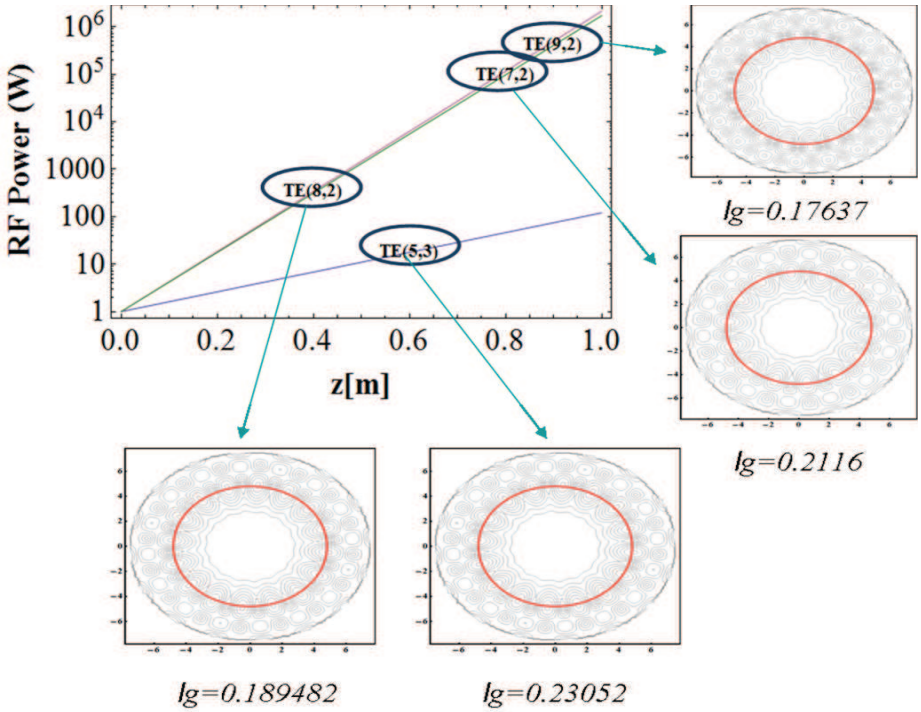

Figure 3.12: Linear growth regime (using the solution from Eq. 3.29) for different transverse mode distribution and associated gain length (lg) for a frequency resonance equal to *250 GHz*. The red circle represents the electron beam transverse distribution with radius R_b *=0.0048 m*, which is assumed to stay well inside the mode itself thus maximizing the filling factor.

being $\omega_{cutoff} = k_\perp/c$ and the pitch $\alpha = v_\perp/v_{||}$.

In Fig.3.15 has been reported the ω_+ values for an electron beam with particles having a longitudinal velocity spread of $\delta v_z = 0.5\%$ (with $\gamma = 2.17 (or E_b = 650\ keV)$ and pitch value $\alpha = 0.53$) interacting with the mode TE_{53} of a cylindrical waveguide (having a radius $r_w = 7.5\ mm$) surrounded by an axial magnetic field of $5.3T$. In this condition in a cold cavity analysis the beam will interact with only one mode

The limit for $\delta\beta_z$ can be derived starting from the approximated CARM resonance condition (Eq. 3.12) coupled with the dispersion relation for the modes in a waveguide (Eq. 3.13) and assuming a fixed k_z value during the interaction:

$$\delta\beta_z < (1-\beta_z)^2 \frac{c\delta k}{\Omega} \approx (1-\beta_z)^2 \frac{\gamma c}{\Omega_c} \frac{\nu_{mn} - \nu_{m'n'}}{R_w} \tag{3.61}$$

being $\Omega = \Omega_c/\gamma$, R_w the waveguide radius and (ν_{mn}/R_w,$\nu_{m'n'}/R_w$) the perpendicular wave vectors of the mode closest to the operating mode.

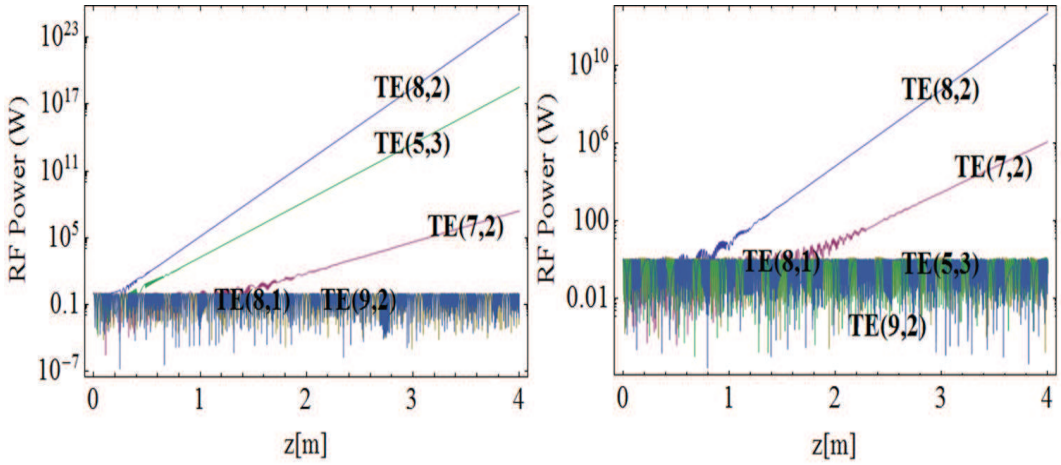

Figure 3.13: Mode intensity evolution including the lethargic part changing the radiation frequency (f) and the annular beam radius (R_b):
a) $f = 258\ GHz$, $R_b = 0.0048\ m$; *b)* $f = 250\ GHz$, $R_b = 0.0042\ m$.

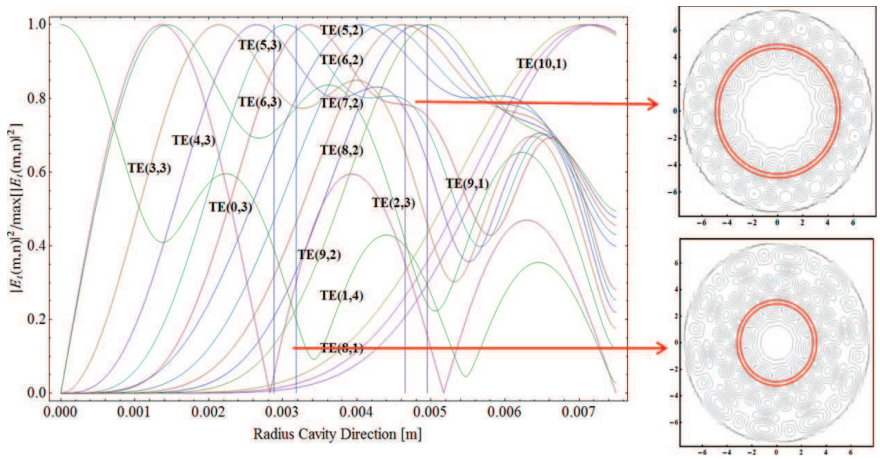

Figure 3.14: Transverse Mode distribution vs. the cavity radius, the vertical lines refer to beam transverse dimensions interacting with the $TE_{5,3}$ or $TE_{8,2}$ mode; on the right side the transverse mode distribution with the transverse annular beam in red.

The formula 3.61 could be refined considering also the induced spread on γ by the particles

$$\delta\beta_z < (1-\beta_z)^2 \frac{c}{\Omega_c} \frac{\nu_{mn} - \nu_{m'n'}}{R_w} \frac{1}{\frac{1}{\gamma} - \gamma(1-\beta_z)\beta_z(1+k^2)} \tag{3.62}$$

in this way for the example of Fig.3.15 the limit for $\delta\beta_z$ is 0.55%.

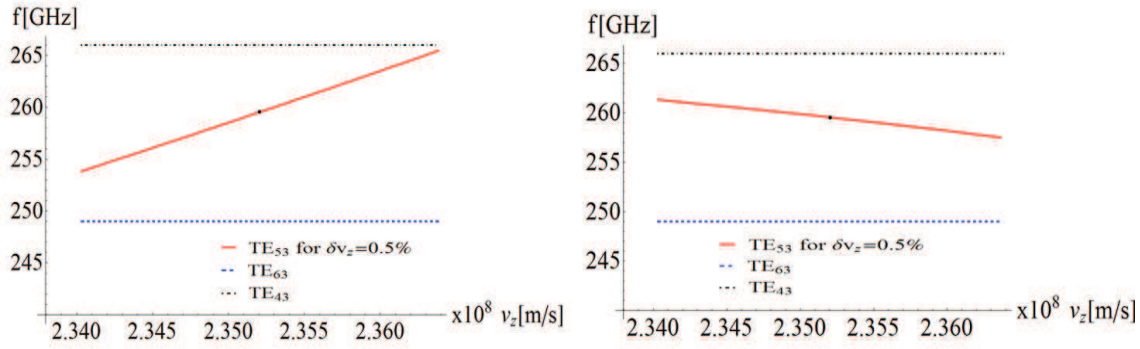

Figure 3.15: The resonance frequency range for a beam line with a velocity longitudinal spread of ($\delta v_z = 0.5\%$) interacting with the mode TE_{53} assuming a constant value for γ (Eq. 3.59) (on the left side) and with a γ variation (Eq.3.60) on the right side. The resonances are well separated from these of the competitors modes TE63 (dotted line) and TE43 (dot-dashed line).

Furthermore, considering the expression for the electron energy

$$E = |e|V + m_e c^2 = \sqrt{(m_e c^2)^2 + c^2(p_z^2 + p_\perp^2)} \tag{3.63}$$

the relativistic factor is given by

$$\gamma = \frac{|e|V}{m_e c^2} + 1 \tag{3.64}$$

By combining the equations on the frequency selection 3.15 (with $\beta_p \approx 1$) and the Hamiltonian 3.63 we end up with the following condition on the magnetic field necessary to get the resonance condition

$$B = \frac{m_e \omega_r}{|e|} \frac{1 + \bar{\alpha}^2}{2} \tag{3.65}$$

being $\bar{\alpha} = \gamma \beta_\perp$ the corresponding strength of the undulator for FEL device.

Requiring $f_r = \omega_r/(2\pi) \approx 250\ GHz$ we find a corresponding magnetic field intensity of the main coil $B \approx 5\ T$.

We can finally summarize in Tab. 3.1 the design request for the electron beam and the magnetic field.

The numbers reported in the previous table fix the conditions for a safe operation of the CARM device, but do not specify the form of operation, which can be either an amplifier or an oscillator. Within the present framework, the latter is more

Table 3.1: **Preliminary Design Parameters**

Beam current	5 A
Beam voltage	700 kV
Longitudinal and transverse Velocity Spread	< 0.5 %
Energy spread	< 0.5 %
Magnetic Field	5 T

convenient for various reasons: it removes the quest for an input source and input couplers, requires a shorter length of the interaction region, with the consequent need of a long high field intensity magnet. Furthermore the amplifier operation demands for the suppression of the backward-wave instability.

In order to ensure the CARM oscillations at the desired Doppler shifted frequency, it will be necessary to design the system in such a way that the relevant threshold current be less than that of the competing modes. This will be done by an appropriate choice of the beam and cavity parameters, as properly discussed in the next chapter.

Chapter 4

CARM Oscillator and cavity design: numerical simulation

A research and development program that has been undertaken at ENEA Frascati Center aims at the realization of a microwave tube well known as a Cyclotron Auto-Resonance Maser (CARM) operating in oscillation mode. The pivotal requirements that must be accomplished by the facility is a generation of a millimeter wave operating in the frequency range of $\sim$ 250 GHz carrying a power of $\sim$ 1 MW in continuous wave (CW) operation reaching a wall-plug efficiency of $\sim$ 30%.
The design of the CARM cavity that consists of a short smooth cylindrical waveguide section delimited by two Bragg reflectors, is a challenging task, facing several theoretical and technological problems. The most severe among them is the competition between the selected operating mode and the neighboring parasitic (spurious) modes. In order to reach the desired efficiency an accurate cavity design, guided by a robust beam-wave interaction model, is necessary. The design of a cavity, with a length around half thousand times the wavelength under investigation, imposes severe constraints, in terms of CPU times and RAM, hardly met by any of the existing commercially available Particle in Cell (PIC) codes. The following procedures has been envisaged for the cavity design: development of a model based on semi-analytical scaling formulae, suitable for the definition of the working point, which will be followed by a full 3D analysis for the cavity optimization. The developed design strategy will be described in the remaining part of the chapter.

4.1 Constraints and design

In order to fulfill the requirements mentioned above, in particular for the CW operation to prevent the discharge the electric field at the surface must be less than 10 kV/mm. Furthermore, the high efficiency value can be maintained with a power wall load less than 2 kW/cm^2 avoiding the cavity deformation and finally the confined power density inside the cavity must be less than 500 kW/cm^2[49].

The requirements merged with the previous discussed constraint leads directly to the following cavity parameters: the Doppler shift should be $3 \div 4$ times the cyclotron frequency Ω_c (varying in the range $65 \div 75$ GHz) to operate in region where the mode overlapping is contained (see Fig.4.1).

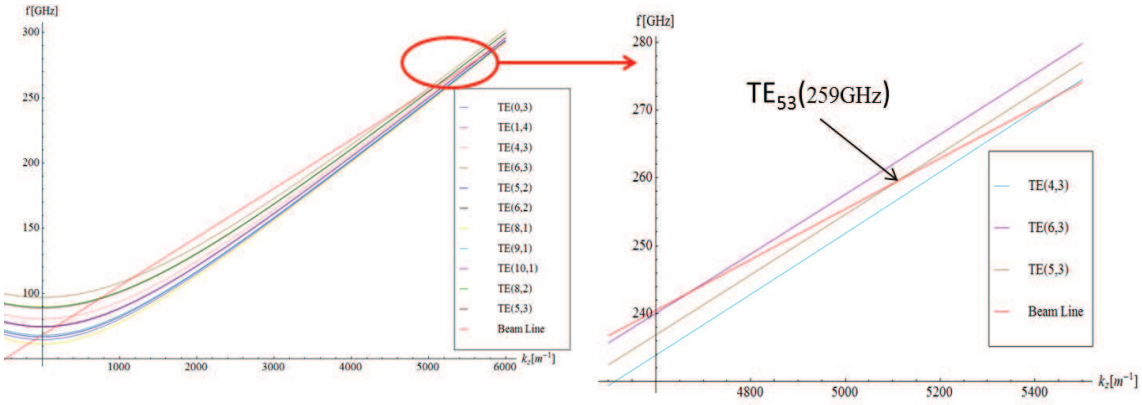

Figure 4.1: Brillouin diagram.

The dispersion relation 3.13 of a cylindrical waveguide with radius r_w reads

$$\frac{\omega^2}{c^2} = (\nu_{mn}/r_w)^2 + k_z^2 \tag{4.1}$$

being ν_{mn} the nth zero of the Bessel function J_m.

In order to limit the operating mode number and considering the confined power density limitation we get the variation range for the cavity cross section $1.5 \div 2.4$ cm^2.

Considering the constrains for the beam line, discussed in the previous chapter and reported in Tab.2.1, the system equations of Eqs. 3.12,3.13 leads to two operating mode at ~ 250 GHz (TE_{53} or TE_{82}) for parameters specified in Tab.4.1.

The choice of the operating mode will be discussed later.

Table 4.1: **Oscillator CARM prameters**

Cathode Voltage	650 kV
Magnetic field	5.3
Pitch ratio ($v_\perp/v_\parallel$)	0.53
Cavity radius	7.5 mm

The design of a CARM cavity is a very difficult problem, already addressed in [50], where different options have been analyzed and compared. In our project, we have chosen the solution consisting of a short smooth cylindrical waveguide section delimited by two Bragg reflectors, the first discussed in Fig. 5 of the refs.[50] and discarding other choices (see below).

The choice of the Bragg resonator configuration has been dictated by the intra cavity power dissipation demand. In ref. [50], two different schemes were proposed. The quasi optical solution was discarded because numerical and analytical calculations have indicated that a cavity length greater than 2 m is necessary in order to reach a reasonable power density on the mirror surface (2 kW/cm^2) . Such a long cavity, with mirror surfaces of $\sim$ 500 cm^2, is not appropriate for our purposes because the length of the superconductive coil proportionally increases, thus implying a significantly larger cost of the device. The other scheme, even though foreseeing the beam wave interaction region limited by the waveguide, demands for cavity mirror radii greater than 2 m, which is not compatible with the annular beam of our project. Accordingly the choice of a more compact cavity, with radius of 1.5 cm and a length of 80 cm, allows a more efficient dissipation of the RF power (see Fig.4.2). In this case the machining must be supported by an appropriate cold test to verify the goodness of the reflectivity properties for the operating and competitors modes. In fact, the most urging problem when dealing with the chosen cavity configurations is the competition between the selected operating mode and the neighboring parasitic (spurious) modes.

The radio frequency circuit design must be supported by a numerical modeling allowing to accurately simulate the intra-cavity beam wave interaction. The large length of this cavity (80 cm) compared to the wavelength under investigation impairs the effectiveness of the classical particle-in-cell (PIC) codes, due to the huge amount of computer memory and CPU time required by the resulting large mesh sizes. In

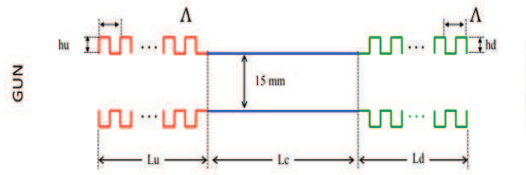

	Upstream	Downstream
Reflectivity	99.9%	61.4%
Period Λ	641 μm	641 μm
depth	140 μm	140 μm
Length	890*Λ = 57.04cm	250*Λ = 16 cm
Cylindrical smooth section		Lc < 13 cm

Figure 4.2: Cavity design with the main parameters values.

parallel to the development of the full numerical treatment, envisaged for a "start to end" simulation, we have undertaken the cavity design by the use of a twofold strategy. We have indeed developed a "home-made" 1D code GRAAL and extended to the CARM case the "universal" scaling formulae, already developed for undulator (U-) based FELs [41].

The numerical code, referred to as GRAAL (which stands for Gyrotron Radiation Auto-Resonance Amplified Laser), is based on a self-consistent procedure developed by several authors [28, 37, 39, 51, 52], while the scaling formulae have been derived after a proper comparison between U-FEL and CARM theories [41, 46] as discussed in the previous chapter.

The two procedures have been crosschecked, benchmarked with the numerical predictions available in literature, with the experimental results from the MIT(Massachusetts Institute of Technology)-CARM test facility[40], operating at low frequency (35 GHz) and the commercial PIC code (CST Microwave Studio®) simulation whose parallel version, working whit Graphics Processing Unit (GPU), has been installed on CRESCO HPC facilities. In case of a CARM amplifier, namely the simplest geometry without Bragg reflectors, experimental data from the Massachusetts Institute of Technology (MIT) [40] have been compared with semi-analytical formulae, GRAAL, the commercial PIC code by CST Microwave Studio® and the CSPOT code by MIT. Measurements are overlapped with predicted curves in Fig.4.3 showing a reasonable agreement among the simulation tools and providing some confidence on the reliability of the method.

The approach we are going to describe is based on the assumption that the beam-wave interaction, resulting in the EM wave generation, take place manly in the smooth cylindrical section of the cavity (L_c in Fig. 4.2). The assumption is also

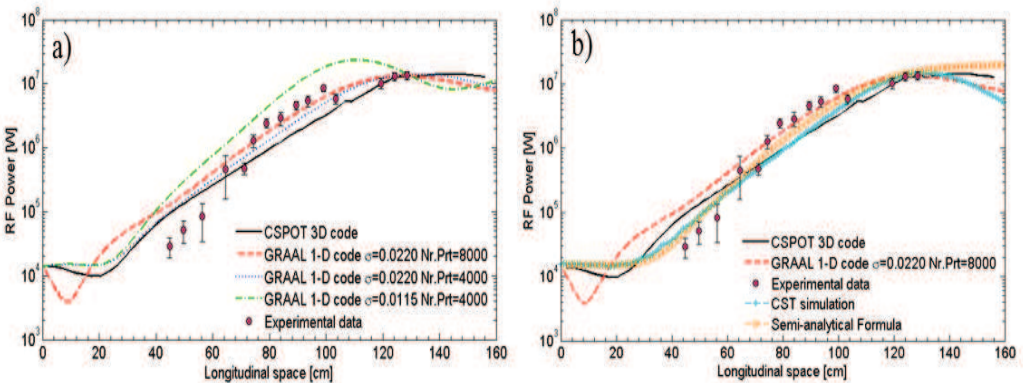

Figure 4.3: Experimental results of a 35-GHz CARM amplifier from MIT compared with: a) the CSPOT code by MIT and the homemade GRAAL code (varying σ, the velocity spread of the beam particles, and the number of particles (Nr. Prt.) used in the simulation) and b) the PIC commercial code by CST Microwave Studio and the semi-analytical formulae.

supported by the design of an adiabatic magnetic field compression at the upstream mirror region which allows to gradually shrink the beam radius, thus inducing a variation in the resonance condition, which prevents the growth of the gyrotron modes, before the constant field profile is reached in the smooth cylindrical section (see Fig.4.4).

A PIC simulation has been performed using CST Microwave Studio® considering only the upstream mirror with an appropriate analytical tapered magnetic field which allows to have a well defined beam radius $Rw = 2.9\ mm$ at the entrance of the smooth section4.4

In Fig.4.5 the results of the simulation show a substantial reduction of the output signal using a tapered magnetic field in particular the TE mode disappear the only TM mode still remain with a low signal level which can be canceled using a slotted cavity, as will be discussed later.

Before concluding the section it useful to point out the reason why it has been chosen the operating mode TE_{53} analyzing the graphs of Fig. 4.6. The resulting analysis of the beam-wave interaction in a cold cavity, using the parameters of Tab. 4.1, show that the maximum of the coupling coefficient for the co-propagating mode TE_{53} is located in a inner radial position than the mode TE_{82} (see Fig.4.6b).

Furthermore, the maximum linear growth signal of an annular beam, with $300\mu m$

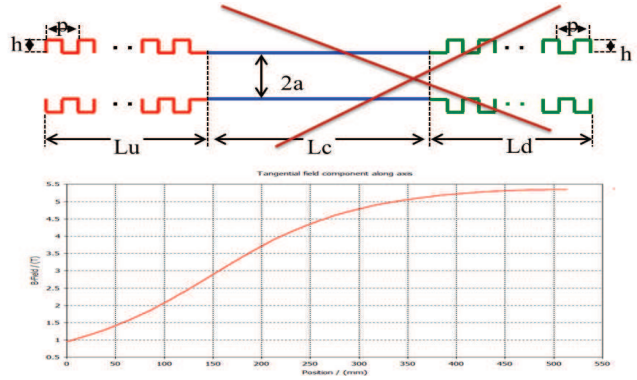

Settings parameters	values
Beam current	5 A
Gamma beam	γ=2.17
Cavity radius	Rw=7.5 mm
Tapered B Field	0.98÷5.3 T
Frequency Range	50-105 GHz
Initial Pitch	0.17
Final Pitch	0.51
Initial Beam radius	R_b^i=6.6 mm
Final Beam radius	R_b^f=2.9 mm

Figure 4.4: The simulation geometry scheme and setting parameters for a tapered magnetic field.

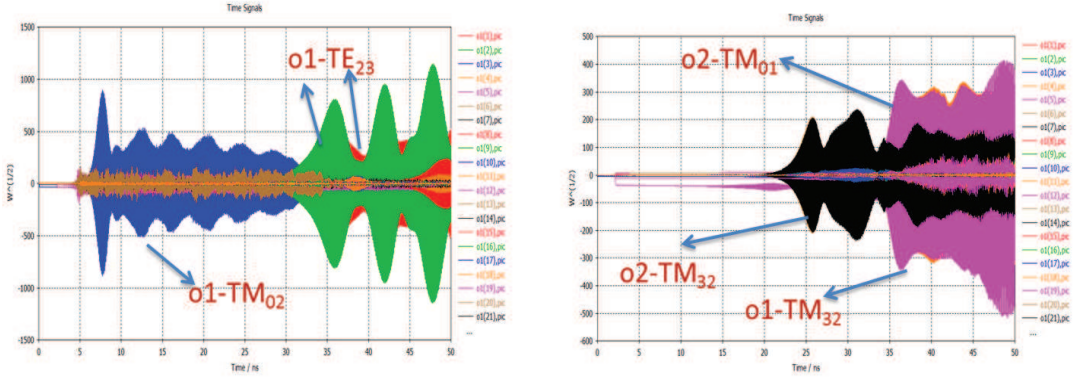

Figure 4.5: The output signal at entrance (01) and at exit (02) of the beam for the first 100 modes propagating inside the cavity using a constant magnetic field(on the right side) and a varying magnetic field (on the right side).

of thickness, is at the radial position which maximize the coupling coefficient, as reported in Fig.4.6c,d) for the mode TE_{53} at the gyrotron (95 GHz) and CARM (259 GHz) resonance, respectively.

The previous discussion leads to the choice of TE_{53} for the operating mode as it allow to have more space to play with the tapering magnetic field avoiding the growth signal of the gyrotron mode.

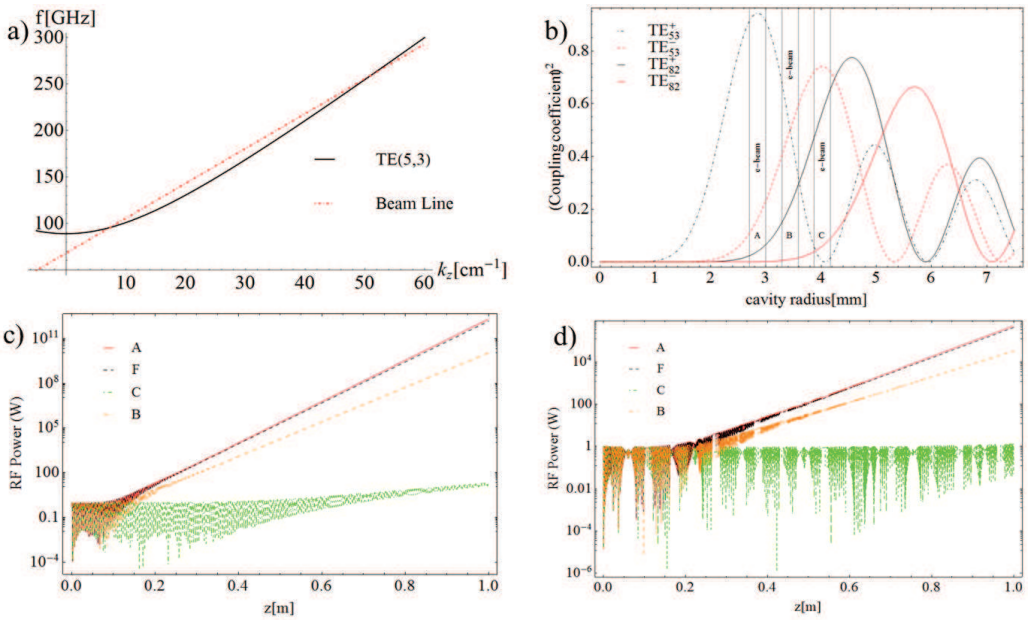

Figure 4.6: In a) the beam wave interaction for the parameters of Tab.4.1 and the coupling coefficient versus the cavity radius for co-counter propagating modes TE_{53} and TE_{82}. The linear growth signal, linearizing the Vlasov-Maxwell equation, for the mode TE_{53} at gyrotron resonance (95 GHz) in c) and at CARM resonance (259 GHz) in d). To evaluate the growth signal has been considered an annular beam with 300μm of thickness centered at different radial position A,B,C as reported in b) related to the maximum of the coupling coefficient. The F corresponds to the radial position ($r_F = 3.1\ mm$) where the transversal electric field of the mode TE_{53} is maximized.

4.2 Operating mode selection: Q-factor, starting current and cavity length

In an oversized cavity, like that one we are going to analyze, a great number of modes ($\approx$ 400) with dense spectrum can be excited as shown in Fig.4.7, which presents many possible intersections of their dispersion characteristics (Brillouin diagrams) with the beam line. This makes the mode selection and correspondingly the single-mode operation a difficult task. The beam-wave interaction in a cold cavity for a CARM oscillator opens three kinds of problems as highlighted in Fig.4.7:

a) the suppression of the beam-wave intersection for the operating mode at low frequency;

b) the suppression of the excitation of the competitor mode near cut-off;

c) the suppression of the modes competition near the Doppler up-shift interaction.

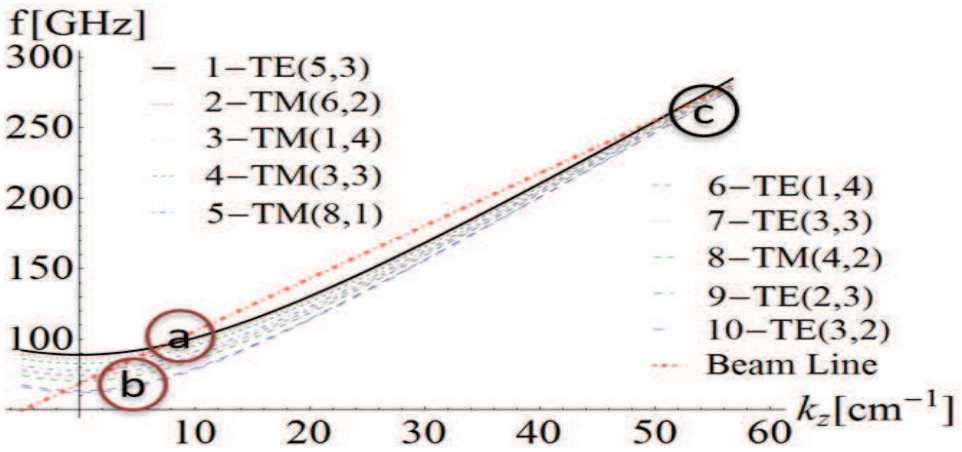

Figure 4.7: Brillouin diagram of a particle beam ($\gamma = 2.17$, $v_\perp/v_{||} = 0.53$) interaction with modes of a cylindrical cold cavity with radius $R_w = 0.75\ cm$ surrounded by an external axial magnetic field $B_0 = 5.3\ T$.

Starting from the point a) we must note that the signal at low resonance exhibit the undesirable feature to grow faster than the signal at CARM resonance (see Fig.4.6c,d)). Furthermore, the temporal growth rate decreases monotonically as the resonance frequency increases away from the waveguide cutoff frequency.

This is easily seen starting from the dispersion relation 3.23, which comes linearizing the Maxwell-Vlasov equation[37, 40]), perturbing the central resonance frequency ω_0 with $\omega = \omega_0 + \Delta\omega$ and deriving the following polynomial equation

$$\Delta^4\omega + 2\left(\Omega_s + k_z v_z\right)\Delta^3\omega + \left(\Omega_s - k_z^2 + 2\Omega_s k_z + k_z^2 v_z^2 - k_{mn}^2 + \bar{\epsilon}k_{mn}^2\right)\Delta^2\omega + \\ +2\left(\Omega_s + k_z v_z\right)\bar{\epsilon}k_{mn}^2\Delta\omega + \left(\Omega_s^2 - k_z^2 + 2k_z v_z + k_z^2 v_z^2\right)\bar{\epsilon}k_{mn}^2 = 0, \qquad (4.2)$$

where $\Omega_s = s\Omega_e/\gamma$ and $\epsilon_{mnns}^{TE} = \bar{\epsilon}/\beta_\perp$ is the coupling parameter of the beam with the cold-cavity mode TE_{mn}.

The fourth degree algebraic equation (4.2) has two real solutions and two complex conjugate roots whose imaginary part versus k_z is plotted in Fig. 4.8 (solid red line) together with the dispersion curve of the mode TE_{53} (solid black line) and the

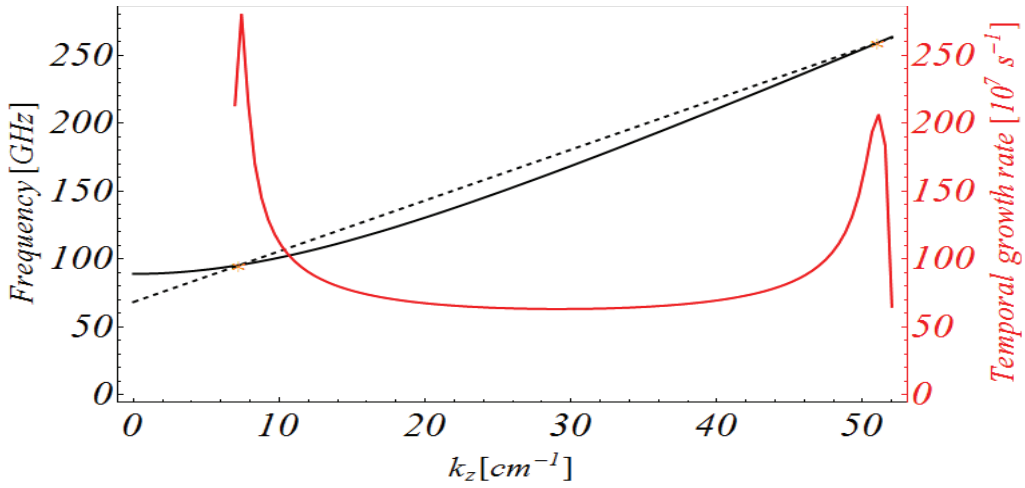

Figure 4.8: The frequencies (left axis) corresponding to the intersection of the dashed beam line with the dispersion curve of the operating mode TE_{53} (solid black line) and the temporal growth rate of the generated signal (right axis).

dashed beam line. The parameters of the electron beam are those reported in Tab. 4.1.

It is evident from Fig.4.8 that the lowest frequency solution exhibits the largest growth rate, therefore this is the mode competing with the desired CARM operation and once coupled to the beam reaches the saturation and suppresses its high frequency counterpart.

In the case of CARM oscillator, a possible solution to prevent the onset of the gyrotron mode is the design of an appropriate cavity with selective losses, inhibiting the growth of the lower-frequency mode. In particular, for a fixed mode the threshold current for the growth of the oscillations can be defined in terms of the parameters of the device including the gain and cavity losses. The energy W of the electromagnetic field stored in the cavity with a quality factor Q is related to the beam power P_b by the equation [29]

$$\eta_a P_b = \omega \frac{W}{Q}, \tag{4.3}$$

where η_a is the efficiency of the interaction at an operating frequency ω. The threshold current ensuring the onset of the oscillations and eventually the saturation is accordingly given by (see [38])

$$I_{thr} = I_A \gamma_0 \beta_z^2 \frac{\pi}{2\lambda} \frac{R^2}{L_c} \frac{1}{QG\tilde{\chi}(\Phi_k)} \tag{4.4}$$

where I_A is the Alfvén current, G is the beam-wave coupling current coefficient, $\widetilde{\chi}(\Phi_k)$ is the gain function, including the beam quality effects as will be discussed later in this section, and L_c is the interaction length, given by the length of the smooth section. The beam-wave interaction in the upstream mirror region is avoided by an adiabatic magnetic field compression in order to shrink gradually the beam radius as discussed in previous section.
The previous identity defines the minimum current, which is necessary in order to overcome the losses and to reach a saturation. It also contains geometrical (L_c) and dynamical factors as the gain function $\widetilde{\chi}(\Phi_k)$.
The strategy we will follow is that of modeling the device parameters in order to increase the threshold current of the gyrotron mode and to prevent any competition with the CARM operation.
The underlying optimization procedure is based also on a reasonable compromise between the gain and the efficiency, which exhibits an opposite behavior with increasing the L_c values: a decrease of the gain leads to an increase of the efficiency.
It is furthermore important to stress that according to ref.[38] the quality factor Q of the cavity can be written as

$$Q = \frac{\omega L_c}{v_{gr}(1 - R_1 R_2)}, \tag{4.5}$$

R_1, R_2 being the reflection coefficients at both sides of the cavity. In the case of the operation at a gyrotron mode, where $k_z \sim 1/L_c$, we can write [38]

$$Q_G \sim 4\pi \left(\frac{L_c}{\lambda_G}\right)^2, \tag{4.6}$$

which is the minimum diffractive Q_G, obtained neglecting the reflectivity. The equation (4.6) shows that Q_G is a large quantity thus, demanding for a small starting current. Our strategy is therefore that of adjusting the kinematic conditions to shift away from the gyrotron mode the interaction ω^- (see Fig.3.3) by increasing of the staring current while preserving an adequate value of the system efficiency.
The optimization procedure, for fixed beam parameters (α, γ, beam current I_0) and magnetic field intensity in the cavity B, involves the following steps[53]:

First step: Select an optimal length L_{opt} of the regular cylindrical section of the cavity which optimizes the system efficiency using the following considerations.

The CARM efficiency, given by the product of the single particle efficiency (η_{sp}) and the transverse efficiency ($\eta_{\perp}$), is close to the η_{sp} if the number of cyclotron turns $N_t = L/(v_z \Lambda_B)$ in the interaction space satisfies the following expression[38]

$$N_{opt} \sim \frac{2}{\beta_{\perp}^2} \frac{(1-\beta_z/\beta_{ph})^2}{(1-\beta_{ph}^{-2})}, \tag{4.7}$$

from which we derive L_{opt}, using $\Lambda_B = 2\pi c/\Omega$.

Second step: Adjust the beam energy and/or the external magnetic field B in order to shift the ω^- intersection (see Fig.3.3) away from the cut-off and to reduce the Q^G value for the gyrotron interaction (in this case the formula given by the (4.6) is not valid) finding a $\overline{B}$ value for which the CARM starting current $I^C_{start}(\gamma(\overline{B}), L_{opt})$ is less than the gyrotron starting current $I^G_{start}(\gamma(\overline{B}), L_{opt})$. Herein the upper indices G, C stand for Gyrotron and CARM modes, respectively. Therefore, for a fixed up-shifted beam-wave interaction (ω^+ in Fig.3.3), we change the magnetic field or γ in the range $2 \div 2.4$ (which is related to the non-relativistic cyclotron frequency Ω_e by $\Omega_e = \gamma(\omega^+ + k_z^+ v_z)$), in order to increase the oscillation threshold current for the gyrotron mode. In particular, evaluating the starting current according to (4.4) for both of the intersections $\omega^-(I^G_{start})$ and $\omega^+(I^C_{start})$ we define the following quantity

$$F(\gamma(B), L_{opt}) = \frac{I^G_{start}(\gamma(B), L_{opt})}{I^C_{start}(\gamma(B), L_{opt})} = \frac{\lambda_C Q_C(L_{opt}) \chi_C(\gamma(B), L_{opt})}{\lambda_G(\gamma(B)) Q_G(L_{opt}) \chi_G(\gamma(B), L_{opt})}. \tag{4.8}$$

Here χ_G and χ_C are the gain in the small-signal approximation for ω^-(G) and ω^+(C), respectively. Then, for a fixed CARM interaction (see the Brillouin diagram in Fig. 3.3), i.e. for a fixed relativistic cyclotron frequency Ω_c, we change the magnetic field B inside the cavity in order to satisfy the condition $F(\gamma(H), L_{opt}) > 1$. From it, we can evaluate the maximum value that can be reached for a given ratio $Q_G(\gamma(H), L_{opt})/Q_C(\gamma(H), L_{opt})$ since

$$\frac{Q_G(\gamma(B), L_{opt})}{Q_C(\gamma(B), L_{opt})} < \frac{\lambda_C(\gamma(B)) \chi_C(\gamma(B), L_{opt})}{\lambda_G \chi_G(\gamma(B), L_{opt})} = \Gamma(\gamma(B), L_{opt}). \tag{4.9}$$

Third step: We determine the Q_C, using the formula describing the dynamics of the CARM oscillator reported in [41]. Then, we select the value of $\overline{B}$, which according to (4.9) yields an acceptable Q_G and satisfies the condition $I^C_{start}(\gamma(\overline{B}), L_{opt}) <$

$I^G_{start}(\gamma(\overline{B}), L_{opt})$.
Starting from $\chi_C(\gamma(B), L_{opt})$, the saturation intensity I_s and considering the ratio $\zeta = \eta_p/\eta_a$ between the passive η_p and active η_a losses, we can determine the equilibrium intracavity power density I_e given by the relation[41]

$$I_e{=}C\left(\sqrt{\frac{1-\eta_a(1+\zeta)}{\eta_a(1+\zeta)}\chi_C(\overline{B}, L_{opt})}-1\right)I_s,$$
$$C{=}(\sqrt{2}+1), \tag{4.10}$$

from which we determine the Q_C specifying an output power of $P_{out} = 1MW$ and using the following equations

$$P_{out} = \eta_a I_e, \quad Q_C{=}2\pi\nu\frac{L_{opt}}{c\eta_a}. \tag{4.11}$$

The underlying optimization is sketched in the block diagram in Fig. 4.9. The search for an optimum interaction length is based on a compromise between gain and efficiency for a given output CARM oscillator power.

It should to be noted that (4.10) is a result of an assumption (only partially supported by the numerical analysis) that the small signal gain of CARM and U-FEL devices exhibit the same dependence on the intra-cavity power. Such assumption is reasonable but it deserves an extensive numerical check, which is under investigation.

Major attention must be paid to the point b) of Fig.4.7 for which the increase of the starting current is not sufficient for suppressing the modes growth excited by the beam near the cut-off where TM modes play a crucial role too.

In Fig.4.10 it has been put in evidence how large is the linear growth signal for the TM_{42} at 70 GHz (near cutoff) with respect to the operating mode TE_{53} at 259 GHz. The starting current for TM modes is minimized at the cut-off, since the group velocity of the wave is well separated from the particle velocity, thus increasing the beam-wave energy exchange. Opposite condition occurs at CARM resonance implying an infinity value for the starting current.

In order to study the cavity mode response at the cut-off frequency range due to the beam-wave interaction a CST simulation has been performed considering only the smooth cylindrical section. This reasonable approximation take into account the fact that the Braggs has been designed to work close to the CARM resonance and

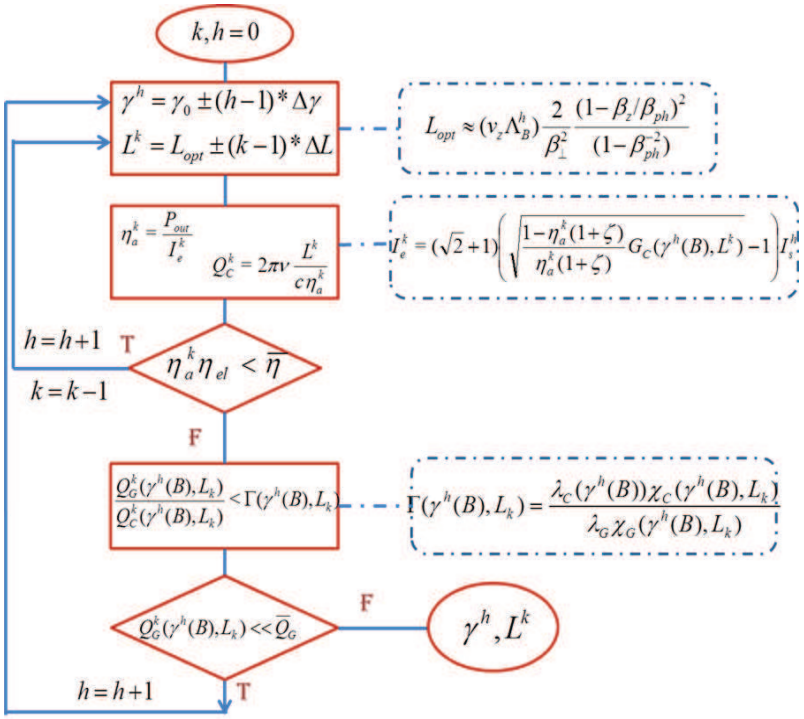

Figure 4.9: Block diagram describing the procedure allowing to fix the beam energy and the smooth cylindrical cavity section length limiting the growing of the lower beam intersection with the operating mode.

the beam-wave interaction will be drastically reduced tapering the magnetic field inside the Braggs (as previously discussed, in particular see Fig.4.5).

In Fig.4.11 has been reported: in the upper side the layout of the simulation with only the smooth cylindrical section which allow to reduce the computational requirement and to simulate the structure on CRESCO ENEAGRID and in the down side the setting parameters with the most significative output modes signals. For each of those modes the cavity quality factor Q and the starting current have been evaluated and reported in the table of Fig.4.12. The TM mode, red encircled in Fig.4.12, represent the most dangerous competitor mode due to the the low value of the starting current and the high growth factor (see Fig.4.10). The only way to suppress this TM mode is by using a slotted cavity.

A cylindrical cavity with a short longitudinal or transversal cut on the boundary surface will avoided the propagation of the competing modes TE or TM respectively

(see Fig. 4.13). The price that we must pay is a reduction of 30% of the system overall efficiency due to the linear polarization of the operating mode induced by the cut.

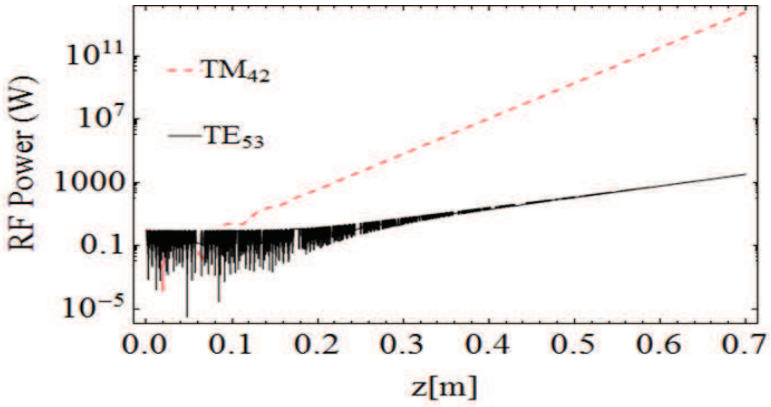

Figure 4.10: The linear growth signal for an electron beam (with $\gamma = 2.17$, $v_\perp/v|| = 0.53$, $I = 8\ A$) interacting with the modes of a cylindrical cavity of radius $R = 7.5\ cm$.

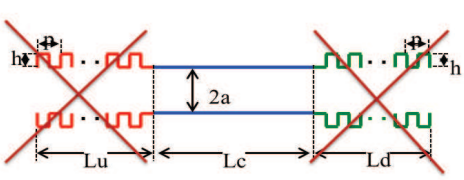

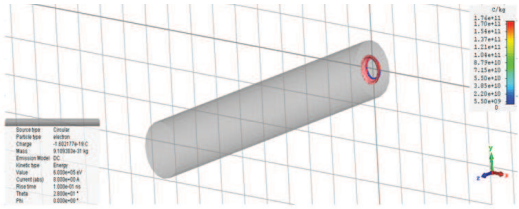

Beam Ring Radius [mm]	2.7 - 3
Beam Current	8 A
Beam Voltage	600 keV
pitch	0.53
Magnetic Field	5.3 [T]
cavity length	13 cm
Frequency range	65-105 GHz

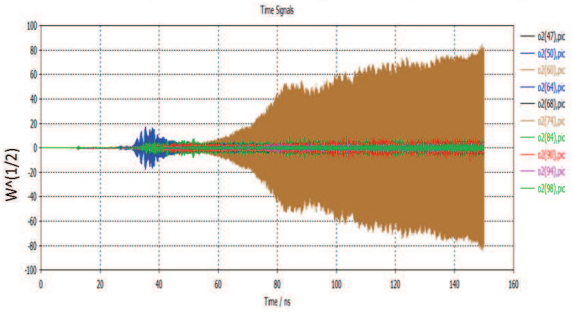

Figure 4.11: PIC simulation results on CRESCO ENEAGRID with two GPUs (a) the geometry design with the particles electron beam (b) the most significant output modes signal excited by the beam at low frequency, the worst in brown is related to the mode TM_{42}.

A further step towards a more definite design of the ENEA CARM has been accomplished by running full-wave simulations of circular waveguides with either

Mode-CST	Cutoff Frequency [GHz]	Beam-Wave Intersection [m^{-1} - GHz] Ωc=68.25	$Q = \frac{\omega W}{P_{out}}$	I_{start} [A]
TM(3,2)- 47	62.09	-153 – 62.52	2095	2.04
TE(2,3) - 50	63.42	-121.97 – 63.69	2600	850.2
TE(5,2) - 56	66.92	-34.94 – 66.94	3209	2.09
TM(4,2)- 60	70.39	58.5 – 70.44	3850	1.29
TE(3,3) - 64	72.18	109.91 – 72.37	2820	1.39
TE(1,4) - 68	74.47	179.08 – 74.95	833	3.3
TM(8,1)- 74	77.77	285.9 – 78.96	369	2190.48
TM(3,3)- 84	82.8	467.3 – 85.74	--	--
TM(1,4)- 90	84.76	545.17 – 88.66	--	--
TM(6,2)- 94	86.45	615.83 – 91.3	--	--
TE(5,3) - 98	88.98	728.73 – 95.5	130	21.94

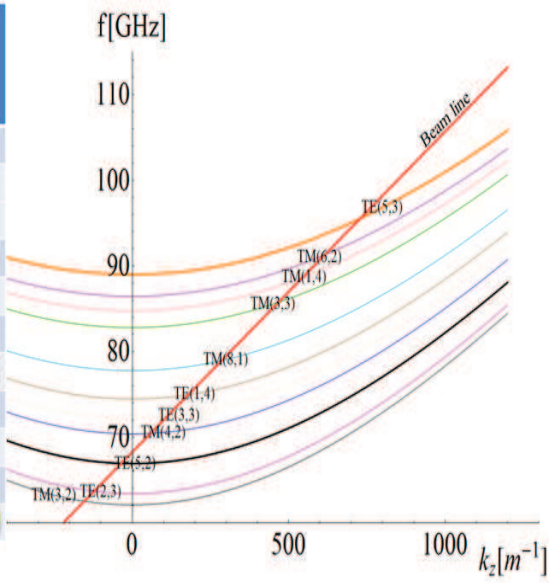

Figure 4.12: On left side table has been reported the with a significant output signal derived by the PIC simulation results are reported in Fig. 4.11; for these mode has been calculated the Q-factor, using the transient module of the CST Microwave Studio, and the related starting current from the Eq. 4.4. The chosen system parameters allow to increase the starting current for the low resonance of the operating mode TE_{53} but major attention must be payed to some gyrotron modes, the most dangerous is the TM_{42} which has a very low starting current in this configuration.

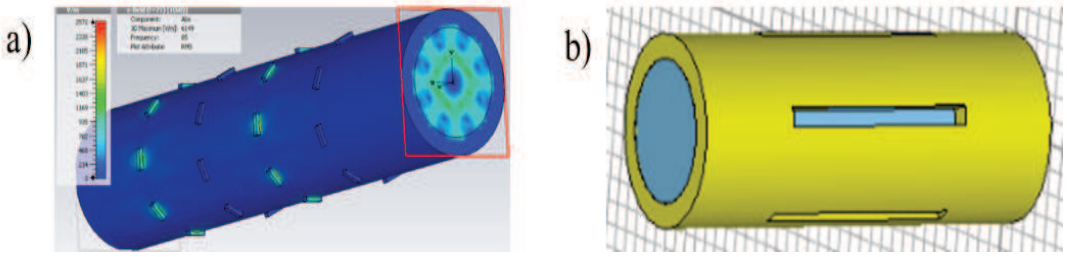

Figure 4.13: Circular waveguide with transversal (a) and longitudinal (b) slots. Light blue identifies vacuum parts, while other colors are used to indicate metals

transversal or longitudinal slots as depicted in Fig. 4.13. Some CARM experiments in the past have been impaired by the excitation of gyrotron modes, namely, waveguide modes intersecting the beam line very close to their cutoff frequency. The most dangerous gyrotron mode of the ENEA CARM is the TM_{42} (see Fig.4.12), whose

propagation can be suppressed by providing waveguide walls with transversal slots. On the other hand, longitudinal slots mostly affect transverse electric modes and can be designed to select a single polarization of the working mode as well as to damp modes with azimuthal index different from the one of the operational mode. Some outcomes of preliminary optimizations carried out for slotted waveguides are reported in Fig. 4.14. For the case of transversal slots, the behavior of a waveguide

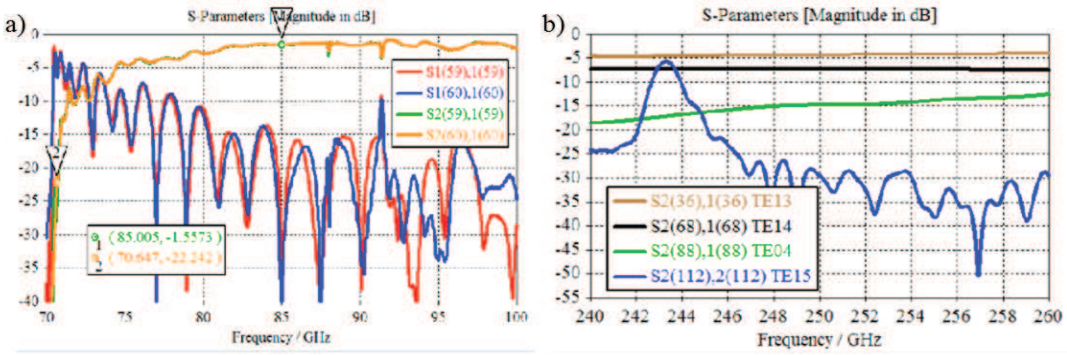

Figure 4.14: (a) Main scattering parameters across the ENEA CARM cavity with 5 rings of 8 transversal slots: both polarization of the TM42, i.e., mode numbers nn = 59 and 60, are impaired when transmitted (S2(nn),1(nn)); adjacent rings are rotated of 22.5 degrees. (b) Main transmission parameters of some unwanted modes in a circular waveguide with internal radius of 2.92 mm and 5 longitudinal slots.

section is studied around the frequency where the dispersion curve of the TM_{42} mode intersects the beam line. This frequency is lower than the operational frequency of the ENEA CARM, leading to a reasonable computation time if the smooth cylindrical section is simulated by means of two GPUs TESLA K40m 2x10 in CRESCO. When moving to 250 GHz, the computational load increases significantly; therefore a waveguide with smaller diameter has been simulated. Despite this geometry differs from the actual cavity, it equally provides a meaningful, though preliminary, assessment of the effects of longitudinal slots on unwanted modes.

The modes competition of the beam wave interaction at CARM resonance, third point c) in Fig.4.7, can be cured generating a high quality beam with a limited longitudinal velocity spread whose estimation is given in Eq. 3.62 (see Fig. 3.15).

Before concluding this section we must put in evidence that for the configuration under study the spurious dangerous mode could be also the TE_{52} with a low starting current (as reported in Fig.4.12) and with the same azimuthal index of the operating mode (TE_{53}) which not allow to be suppressed this mode with a slotted cavity. Anyway, the results achieved with a multi-mode PIC simulation performed with CST at frequency near the cut-off show that the output signal for the gyro-backward TE_{52} is much less than output signal for the TM_{42} as reported in Fig.4.15. However, if with the simulation including the Braggs and enlarging the frequency range till the CARM resonance we achieve a significant growth of the TE_{52} mode we can control the effect by a bunchmarking of the magnetic field inside of the optical cavity. In this way near the cut-off we can drive the interaction of the beam line with a mode having a different azimuthal index of the operating mode and which can be suppressed with an appropriate slotted cavity.

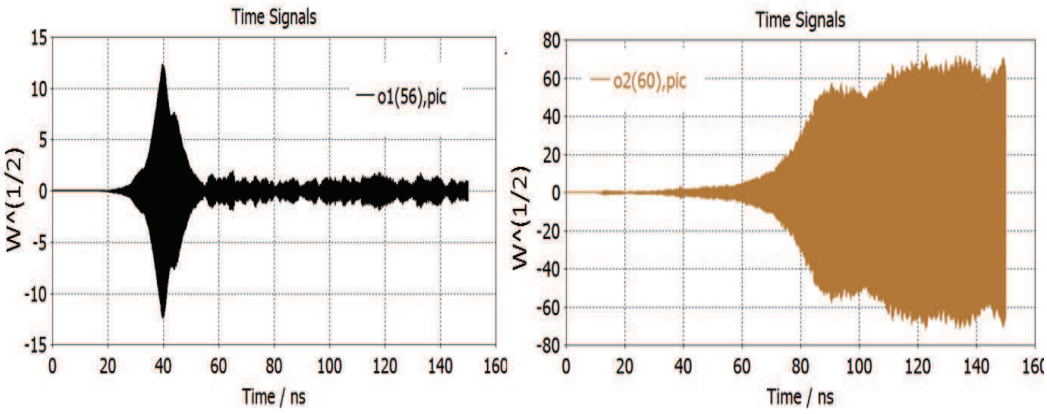

Figure 4.15: The output signal for the gyro-backward mode TE_{52} (on the left) and the TM_{42} mode (on the right): the results has been achieved with a multi-mode PIC simulation for a 13 *cm* of a smooth cylindrical cavity using the parameters set reported in table of Fig.4.11 and considering all the modes having the cut-off between $11 \div 90$ GHz.

In the following section we will discuss the effect of the energy spread on the starting current.

4.3 Starting current and energy spread

The gain function in the Eq.4.4 for a CARM interaction in low gain regime is given by the following expression [38]

$$\begin{aligned}\chi(\Phi_k) &= -\left(1-\frac{\beta_z}{\beta_{ph}}\right)\phi(\Phi_k)+ \\ &+ 3\frac{\beta_\perp^2}{2\beta_z\beta_{ph}}\left[\phi(\Phi_k)+\Phi_k\phi(\Phi_k)'\right]-\frac{\beta_{\perp^2}(1-\beta_{ph}^{-2})Z_{out}}{2}\phi(\Phi_k)' \end{aligned} \quad (4.12)$$

being

$$\phi(\Phi_k) = Re\left[\int_0^1\left(\int_0^\xi \mathbf{e}^{\imath\Phi_k(\xi-x)}dx\right)d\xi\right] = \frac{1-\cos(\Phi_k)}{\Phi_k^2}, \quad (4.13)$$

characterizing the spectrum of the wave acting on the electrons with constant amplitude in the spatial range $0 < x < Z_{out}$ being $Z_{out} = \omega L/v_z$, $\Phi_k = \delta_0 Z_{out}$, ω the resonance frequency and δ_0 the detuning parameter

$$\delta_0 = 1-\frac{\beta_z}{\beta_{ph}}-\frac{\Omega_c}{\omega} \quad (4.14)$$

The inclusion of the gain distortion effects due to the velocity spread can be easily done by convolving the function $\chi(\Phi_k)$ on the velocity distribution reported below.

The relevant procedure is sketched below. The beam velocity spread effect on the detuning parameter δ_0 is taken into account through the ϕ function

$$\phi(\Phi_k+\delta\Phi_k) = Re\left[\int_0^1\left(\int_0^\xi \mathbf{e}^{\imath(\Phi_k-NK\epsilon)(\xi-x)}dx\right)d\xi\right]; \quad (4.15)$$

where

$$N=\frac{L}{\Lambda\beta_z},\ \Lambda=\frac{2\pi c}{\Omega},\ K=\frac{\omega_R\Lambda}{c\gamma^2\beta_{ph}\beta_z} \text{ and } \epsilon=\frac{\Delta\gamma}{\gamma}.$$

The assumption of a gaussian energy distribution for the beam velocity spread modifies the ϕ function in the following way

$$\phi(\Phi_k^{\sigma_\varepsilon}) = Re\left[\frac{1}{\sqrt{2\pi}\sigma_\varepsilon}\int_{-\infty}^{\infty}\phi(\Phi_k+\delta\Phi_k)\mathbf{e}^{-\frac{\varepsilon^2}{2\sigma_\varepsilon^2}}d\varepsilon\right] =$$
$$= Re\left[\int_0^1(1-t)\mathbf{e}^{\imath\Phi_k t-\frac{(\pi\widetilde{\mu}_\epsilon)^2t^2}{2}}dt\right], \tag{4.16}$$

where μ_ϵ is the inhomogeneous broadening parameter

$$\widetilde{\mu}_\epsilon = 4N\sigma_\epsilon\frac{\omega_R}{2\Omega\gamma^2\beta_z\beta_{ph}}. \tag{4.17}$$

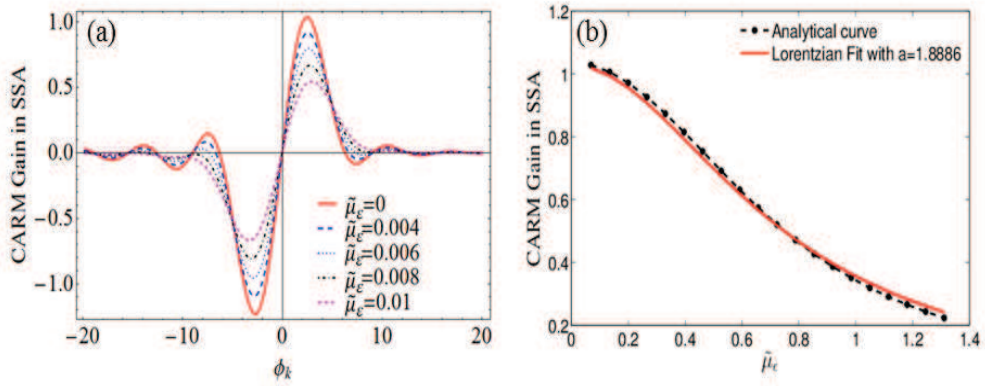

Figure 4.16: (a): The CARM Gain in SSA without beam spread (continuous line) and with different values of the beam spread $\widetilde{\mu}_\epsilon$ (dashed lines);(b): the maximum value od the CARM gain (dot-line) vs $\widetilde{\mu}_\epsilon$.

In Fig.4.16, the gain which takes into account the beam velocity spread has been fitted with a Lorentzian function

$$G(\widetilde{\mu}_\epsilon) = \frac{G_0}{1+a\widetilde{\mu}_\epsilon^2}, \tag{4.18}$$

G_0 being the gain without spread.

Fig.4.17 shows the plot of $\Gamma(\gamma(B), L_{opt})$ and the starting current values versus the magnetic field B inside the cavity for a beam, with the parameters used in Fig. 4.12, interacting with the operating mode TE_{53} of a cavity with a radius $R_w = 7.5mm$ and a smooth section $L_{opt} = 13cm$. The admissible values of the cavity Q-factor

ratio (Fig.4.17a) are constrained within the continuous curve, in the case of a beam with negligible energy spread, or within the dashed counterpart for a more realistic beam.

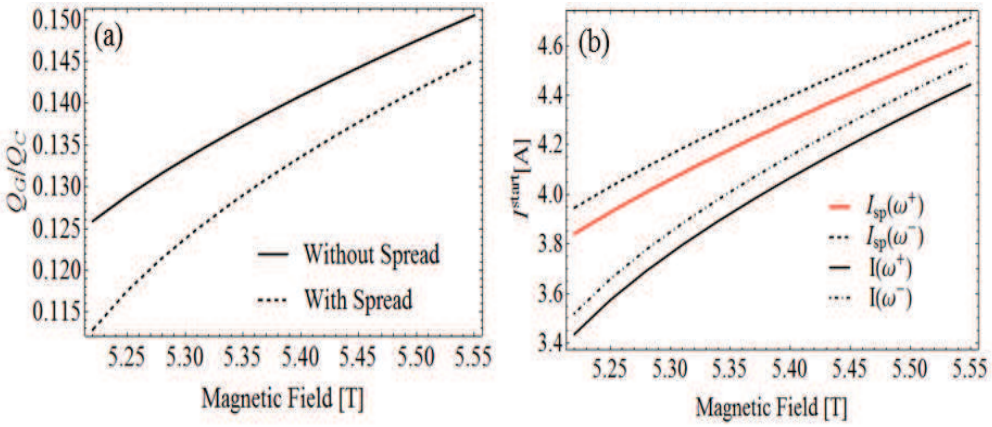

Figure 4.17: (a): the maximum admissible value for the quality factors ratio evaluated at ω^+ and ω_- vs the magnetic field; (b): the starting current values vs the magnetic field in the cavity for a fixed quality cavity factors $Q_C = 3300$ and $Q_G = (\Gamma(\gamma(H), L_{opt}) - k)Q_C$ with $k = 0.003$. In both cases we show the effect of the velocity spread of the beam electrons considering a Gaussian distribution with a dispersion $\sigma_\epsilon = 0.003$.

4.4 Conclusions

This thesis has covered almost all the aspects of the CARM design activity at the ENEA Frascati center.

The project has undergone different stages of development, reported in the Conceptual Design Report(CDR)[27] which has been submitted to a panel of experts (workshop held at Enea Frascati Center on 2-3 November 2016) who have approved the whole conception, the design solutions, the technological choices...

The panel made however a series of recommendation which have been only partially taken into account, it is important to review the points raised by the Referees because they will provide the future developments of the research undertaken in the thesis.

It is also important to underline that the CARM project is moving towards the stage of delivering of the tender of its main components, among which the modulator

is one of the most delicate elements, because of the novelty of the relevant design and of the request of the specific performances. These if not fulfilled may induce a deterioration of the beam qualities, which, in turn may be the source of dilution of the CARM gain and of its efficiency. Within this respect the commission has recommended a thorough analysis of the interplay between modulator performances and beam qualities and the study of strategies to prevent the relevant negative feedback.

A further element of concern has been the elimination of the spurious modes and the mode selections, which are points treated within the main body of the thesis The settling out of these points have been accurately investigated using either home -made and commercial (CST Microave Studio ®) codes. Within such a respect a real comparison has been hampered by the quoted computational difficulties associated with the mesh-size and the available memory. Even though most of these points have been solved by a wise application of numerical and analytical tools and the results we have obtained provides a good deal of confidence on the solutions we have proposed, we are developing a more appropriate effort foreseeing a full numerical strategy (by using CST Microave Studio ® and, as suggested by the panel, with the MICHELLE code developed at Massachusetts Institute of Technology) which envisages the use of the CRESCO/ENEAGRID High Performance Computing infrastructure enhancing the power simulation with two GPUs TESLA K40. However, this is not still enough to simulate the beam-wave interaction for the whole CARM cavity.

These points are under current investigations, but require further efforts including the necessity of a start to end simulation of the CARM oscillator including the characteristics of the Bragg resonator.

The thesis has covered about three years of research work and has benefitted of the discussion and the collaboration with Italian and foreign scientists, with long standing experience in the theory and realization of Gyrotron and CARM and FEL devices.

The work presented here has been therefore the result of a fruitful collaboration which has also lead to the publications on peer review journals and on conference proceedings hereafter listed

- E. Di Palma, G. Dattoli, E. Sabia, S. Sabchevski and I. Spassovsky, “Beam-wave interaction from FEL to CARM and associated scaling laws”, IEEE Transection on Electron Device, Vol. 99, 21August 2017, pp.1-8.

DOI: https://doi.org/10.1109/TED.2017.2738673

- G. Dattoli, E. Di Palma, S. Pagnutti, E. Sabia, "Free Electron Coherent Sources: from Microwave to X-rays", to be published on Physics Reports (A Review Section of Physics Letters).

- E. Di Palma, E. Sabia, G. Dattoli, S. Liciardi and I. Spassovsky, "Cyclotron auto resonance maser and free electron laser devices: a unified point of view", J. Plasma Phys., Vol. 83(1), February 2017.

  DOI: https://doi.org/10.1017/S0022377816001239

- ENEA CARM Design Team, "A 250 GHz Radio Frequency CARM Source for Plasma Fusion", website: www.enea.it/it/pubblicazioni/pdf-volumi/v2016-cdr-carm.pdf, volumi Enea, ISBN:978-88-8286-339-5, pp. 1-154, 2016.

- S. Ceccuzzi, G. Dattoli, E. Di Palma, A. Doria, E. Sabia, I. Spassovsky, "The High Gain Integral Equation for CARM-FEL devices", IEEE Journal of Quantum electronics vol. 51, no. 7, July 2015.

  DOI: https://doi.org/10.1109/JQE.2015.2432719

- F. Mirizzi, I. Spassovsky, S. Ceccuzzi, G. Dattoli, E. Di Palma, A. Doria, G.P. Gallerano, A. Lampasi, G. Maffia, G.L. Ravera, E. Sabia, A.A. Tuccillo, P. Zito, "A high frequency, high power CARM proposal for the DEMO ECRH system", Fusion Engineering and Design, Volumes 96–97, October 2015, pp. 538-541. DOI: https://doi.org/10.1016/j.fusengdes.2015.02.026

- E. Di Palma, G. Dattoli, S. Ceccuzzi, E. Sabia, G. L. Ravera, I. Spassovsky, F. Mirizzi, A. Doria, A.A. Tuccillo, G.P. Gallerano and the ENEA CARM Task Force, "The CARM beam-wave interaction and cavity design", 10th International Workshop on Strong Microwave and therahertz waves: sources and applications, 17-22 July 2017, Nizhny Novgorod –Moscow (Russia). DOI: https://doi.org/10.1051/epjconf/201714904008

- S. Ceccuzzi, G. Dattoli, E. Di Palma, A. Doria, G.P. Gallerano, G.L. Ravera, I. Spassovsky, A.A. Tuccillo and the ENEA CARM Team, "Comparison of reflector concepts for a 250 GHz CARM cavity", 10th International Conference

on Strong Microwave and therahertz waves: sources and applications, 17-22 July 2017, Nizhny Novgorod –Moscow, Russia.

DOI: https://doi.org/10.1051/epjconf/201714904009

- G. L. Ravera, S. Ceccuzzi, G. Dattoli, E. Di Palma, A. Doria, G. P. Gallerano, E. Giovenale 1, F. Mirizzi, G. Schettini, I. Spassovsky, and A. A. Tuccillo, "Mode Converters in Overmoded Circular Waveguide for a 250 GHz CARM Source", 38th Progress In Electromagnetics Research Symposium (PIERS), 22-25 May 2017, St. Petersburg Russia.

- E. Di Palma, S. Licciardi, E. Sabia, G. Dattoli, "Numerical modelling of a CARM oscillator at High Frequency", Internatonal CARM meeting, November 03-04, 2016, Enea Frascati.

- E. Di Palma, S. Ceccuzzi on behalf of the CARM Team, "Update of Cyclotron Auto- Resonance Maser (CARM) project at ENEA-FRASCATI", US-EU-JPN Workshop on RF Heating Technology, Karlsruhe(Germany) 21-23 September 2016.

- N.S.Ginzburg, M.Yu. Glyavin, N.Yu. Peskov, A.V. Savilov, V. Yu. Zaslavsky, I.P. Spassovsky, E. Di Palma, S. Ceccuzzi, F. Mirizzi, G. L. Ravera and G. Dattoli, "Prospects of Realization of Powerful Sub-Millimeter Relativistic Cyclotron Masers",41st International Conference on Infrared, Millimeter, and Terahertz waves (IRMMW-THz), 25-30 September 2016, Copenhagen, Denmark.

Bibliography

[1] G. Dattoli, M. Artioili, A. A. Tuccillo *Understanding the limits of the development*, ENEA Technical Report, vol. 17, nr. RT/2017/17/ENEA, ISSN/0393-3016.

[2] P. Glen, G. Marland, C. Le Quéré, T. Boden, J.G. Canadell, M.R. Raupach *Rapid growth in CO2 emissions after the 2008–2009 global financial crisis*, Nature Climate Change, vol. 2, January 2012.

[3] E. M. Efstathios *Alternative Energy resources*, Ed. Springer 2011.

[4] Cabal H., Lechón Y. , Bustreo C. , Eder T., Biberacher M., Grohnheit P.E., and Gadomska M., *Analysis of the potential contribution of fusion power in a future low carbon global electricity system*, to be published.

[5] D. Maisonnier et al., *The European Power Plant Conceptual Study*, Fusion Eng. Des., 2001, **75-79** 1173-9.

[6] K. Lackner *Socio-economic aspects of fusion power* , European Development Agreement Report, CCE-FU 10/6.2.2.

[7] Cook I., Miller R.L. and Ward D.J. *Prospects for economic fusion electricity* , Fusion Eng. Des., 2002, **63-64** 25-34.

[8] D.J. Ward et al., *The economic viability of fusion power*, Fusion Eng. Des.,2005, vol. **75-79** 1221-7.

[9] P. King et al, *European Council of Ministers Conclusions of the fusion fast track experts meeting hels on 27 November 2001 on the initiative of Mr. Donnea(President of the Research Council)*, EUR(02) CCE-FU/FTC 10/4.1.1,Brussels 5 December.

[10] V. Pericoli, *DEMO R&D challenges*, ISFNT conference Dalian China 11-16 Octoer 2009.

[11] J. Garcia et al., *Analysis of DEMO scenarios with the CRONOS suite of codes*, Nucl. Fusion,2008, vol. **48** 075007 (9pp).

[12] G. Federici et al., *Overview of the design approach and prioritization of R&D activitiestowards an EU DEMO*, Fusion Eng. Des., 2016, **109–111** 1464–1474.

[13] J. Pamela et al., *Efficiency and availability driven R&D issues for DEMO*, Fusion Eng. Des., 2009, **84(2)** 194-204.

[14] H. Zhom, *On the minimum size of DEMO*, Fusion Sc. Tech., 2010, **58** 613–624.

[15] D. Landau, *On the vibration of the electronic plasma*, J. Phys (USSR), 1946, **10** 25–34.

[16] D. G. Swanson, *Plasma Waves* , Academic Press, San Diego 1989.

[17] G. Bekefi, *Radiation Processes in Plasma* , (New York:Wiley), 1966.

[18] M. Botanici et al., *Electron Cyclotron Emission and Absorption in Fusion Plasmas*, Nucl. Fusion, 1983, **23** 1153-1257.

[19] R. Wenninger et al., *The physics and technology basis entering European system code studies for DEMO*, Nucl. Fusion, 2017, **57** 016011 pp. 1-11.

[20] T.C. Luce et al., *Generation of Localized Non inductive Current by Electron Cyclotron Waves on the DIII-D Tokamak*, Phys. Rev. Lett., 1999, vol. **83**(22) 4551-4553.

[21] E. Poli et al., *Electron-cyclotron-current-drive efficiency in Demo plasmas*, Nucl. Fusion, 2013, **53** 1-10.

[22] R. Wenninger et al., *Advances in the physics basis for the European DEMO design*, Nucl. Fusion, 2015, **55** 1-7.

[23] H. Zhom et al., *Control of NTMs by ECCD on ASDEX Upgrade in view of ITER application*, Plasma Phys. Control. Fusion, 2007, **49** B341-B347.

[24] G. Granucci et al., *Conceptual design of the EU DEMO EC-system: main developments and R&D achievements*, Nucl. Fusion, 2017, vol. **57(11)** 6009-60017.

[25] R. J. Barker et al., *Modern Microwave and Millimeter-Wave Power Electronics* , A JOHN WILEY & SONS, INC., PUBLICATION (2005).

[26] K. Sakamoto, T. Kariya, Y. Oda, R. Minami, R. Ikeda, K. Kajiwara, T. Kobayashi, K. Takahashi, S. Moriyama and T. Imai ,*"Study of sub-terahertz high power gyrotron for ECH&CD system of DEMO"*, *IEEE International Conference on Plasma Sciences (ICOPS)*, pp. 1-1, Anatalya 2015.

[27] ENEA CARM Design Team,*"A 250 GHz Radio Frequency CARM Source for Plasma Fusion"*, *website:www.enea.it/it/pubblicazioni/pdf-volumi/v2016-cdr-carm.pdf*, volumi Enea, ISBN:978-88-8286-339-5, pp. 1-154, 2016.

[28] V. L. Ginzburg, *"On emission of microwaves and their absorption in air"*, *Izv. Akad. Nauk. SSSR, Ser- Fiz.*, vol. 11, pp.165-182, 1947.

[29] M.I. Petelin, *"On the theory of ultrarelativistic cyclotron self-resonance masers"*, *Radiophys. Quantum Electron.*, vol. 17(6), pp. 902-908, Jun. 1974.

[30] K.R. Chen, J.M. Dawson, A.T.Lin, and T. Katsouleas *"Unified theory and comparative study of cyclotron masers, ion channel lasers and free electron lasers"*, *Physics of Plasmas*, vol. 3, 1270 (1991).

[31] A. V. Gaponov, *"Interaction between electron fluxes and electromagnetic waves in waveguides"*, *Izv. Vyssh. Uchebn. Zaved. Radiofiz.*, vol. 2, pp.450-462, 1959.

[32] E.S. Weibel, *"Sponatanously growing transverse waves in a plasma due to an anisotropic velocity distribution"*, *Phys. Rev. Lett.*, vol. 2, pp.83-84, Feb. 1959.

[33] K.R. Chu, *"The elctron cyclotron Maser"*, *Reviews of modern physics*, vol. 76, pp.489-538, April. 2004.

[34] K.K. Chow and R.H. Pantell, *"The cyclotron resonance backward-wave oscillator"*, *Proc. IRE*, vol. 48, pp. 1865-1870, 1960.

[35] K.R. Chu and J.L. Hirshfield, *"Comparative study of the axial and azimuthal bunching mechanism in electromagnetic cyclotron instabilities"*, *Phys. Fluids*, vol. 21(3), pp.461-466, March 1978.

[36] G. Dattoli, A. Torre and A. Renieri, Lectures on the Free Electron Laser Theory and related Topics, World Scintific, 1993.

[37] G. Nusinovich, Introduction to the physics of Gyrotrons, The Johns Hopkins University Press, June 2004.

[38] V.L. Bratman, N.S. Ginzburg, G.S. Nusinovich, M.I. Petelin and P.S. Strelkov, *"Relativistic gyrotrons and cyclotron autoresonance maser"*, *Int. J. Electron.*, vol. 51(4), pp. 541-567, Sep. 1981.

[39] A. W. Fliflet, *"Linear and non-linear theory of the Doppler-shifted cyclotron resonance maser based on TE and TM waveguide modes"*, *Int. J. Electron.*, vol. 61(6), pp. 1049-1080, Aug. 1986.

[40] C. Chen, S. Wurtele, *"Linear and non linear theory of cyclotron autoresonance masers with multiple waveguide modes"*, *Phys. Fluids B*, vol.3, pp.2133, Apr. 1991.

[41] S. Ceccuzzi, G. Dattoli, E. Di Palma, A. Doria, E. Sabia and I. Spassovsky, *"The High Gain Integral Equation for CARM-FEL Devices"*, *IEEE J. Quantum Elect.*, vol. 51(7), pp. 1-9, Jul. 2015.

[42] G. Dattoli, P.L. Ottaviani and S. Pagnutti, *"Booklet for FEL Design: A Collection of Practical Formulae"*, Frascati, Italy: Edizioni Scientifiche Frascati, 2007.

[43] Marcello Artioli, Giuseppe Dattoli, Pier Luigi Ottaviani, Simonetta Pagnutti, *"Virtual Laboratory and Computer Aided Design for Free Electron Lasers outline and simulation"*, Energia Ambiente e Innovazione / Anno 2012 / n. 3 Maggio-Giugno 2012.

[44] , E. Saldin, E.V. Schneidmiller and M.V. Yurkov, *"The Physics of Free Electron Lasers"*, Springer-Verlag Berlin Heidelberg 2000.

[45] N. Kroll, P. Morton and M.N. Rosenbluth, IEEE J. Quantum Electron. 17, 1436 (1981).

[46] V.L. Bratman, N.S. Ginzburg and M.I. Petelin, *"Common properties of free electron lasers"*, Opt. Commun., vol. 30, no. 3, pp. 409–412, 1979.

[47] G.S. Nusinovich , P.E. Latham and H. Li, Efficiency of frequency Up-Shifted Gyrodevices: Cyclotron Harmonics Versus CARM's, *IEEE Trans. Plasma science*, vol. 22(5), pp. 796-803, October 1994

[48] E. Di Palma,E. Sabia, G. Dattoli, S. Licciardi, I. Spassovsky, Cyclotron auto resonance maser and free electron laser devices: a unified point of view, *Journal of Plasma Physics*, 83(1), pp. 905830102, 2017.

[49] M. Gilden and L. Gould, *Handbook on High Power Capabilities of Waveguide Systems* , Microwave Associates Inc., 1964.

[50] V.L. Bratman and G.G. Denisov,*"Cyclotron autoresonance masers- recent experiments and prospects"*, *Int. J. Electronics*, vol. 72(5-6), pp. 969-981, 1992.

[51] A.V. Gaponov, M.I. Petelin, and V.K Yulpatov,*"The induced radiation of excited classical oscillators and its use in high-frequency electronics"*, *Radiophys. Quantum Electron.*, vol. 10(9), pp. 794-813, Jul. 1967.

[52] V.K. Yulpatov,*"Nonlinear theory of the interaction between a periodic electron beam and an electromagnetic wave"*, *Radiophys. Quantum Electron.*, vol. 10(6), pp. 846-856, Jun. 1967.

[53] E. Di Palma, G. Dattoli, E. Sabia, S. Sabchevski and I. Spassovsky, Beam-wave interaction from FEL to CARM and associated scaling laws", IEEE Transection on Electron Device, *IEEE Transection on Electron Device*, 99, pp.1-8, Aug. 2017.